MASS SPECTROMETRY AS A PLATFORM FOR CHARACTERIZATION AND QUANTITATION OF PROTEINS ACROSS BIOLOGICAL AND CLINICAL SYSTEMS.

AYESHA MAQSOOD

A DISSERTATION SUBMITTED TO THE FACULTY OF GRADUATE STUDIES IN PARTIAL FULFILLMENT OF THE REQUIREMENTS FOR THE DEGREE OF DOCTOR OF PHILOSOPHY.

Department of Chemistry, York University, Toronto, Ontario

August 2026

© Ayesha Maqsood, 2026

Abstract

Proteins regulate virtually all cellular processes, and changes to their abundance, structure, or conformational dynamics are frequently associated with human disease. While advances in structural biology have provided important insight into protein architecture, many biologically relevant proteins remain difficult to characterize due to their dynamic nature and structural heterogeneity. The overall objective of this dissertation was to develop and apply mass spectrometry-based approaches to investigate proteins of clinical and biological importance, with a particular focus on understanding how structural perturbations influence protein function in disease.

Targeted proteomic workflows were developed to support the sensitive and reproducible measurement of protein biomarkers in complex biological matrices. In parallel, hydrogen–deuterium exchange mass spectrometry (HDX-MS) was applied to examine the conformational consequences of disease-associated mutations and post-translational modifications. Methodological advances, including the optimization and implementation of an automated continuous-flow time-resolved electrospray ionization (CFI-TRESI) HDX-MS platform, improved the robustness and reproducibility of measurements for highly dynamic protein systems.

Application of these approaches revealed that both genetic mutations and phosphorylation events can induce distinct changes in protein conformational behaviour that are not apparent from static structural models. Studies of the signalling protein STAT5B identified mutation-specific alterations in conformational dynamics associated with disease-related gain- and loss-of-function phenotypes. Investigation of the intrinsically disordered tau protein demonstrated that phosphorylation by different kinases generates distinct conformational states, providing new insight into the structural heterogeneity associated with tau pathology and neurodegenerative disease.

Together, these findings demonstrate the importance of protein dynamics in regulating biological function and disease-associated dysfunction. More broadly, this work highlights the versatility of mass spectrometry for addressing questions that span clinical proteomics, structural biology, and disease mechanism research. The methodologies and insights developed throughout this dissertation contribute to a growing understanding of how protein structure and dynamics influence human disease and provide a foundation for future biomarker and therapeutic discovery efforts.

Acknowledgements

All praise is due to God, the Almighty, whose countless blessings have carried me through every stage of this journey.

This work would not have been possible without the support, encouragement, and generosity of many people. First and foremost, I extend my sincere gratitude to my supervisor, Dr. Derek Wilson, for his invaluable mentorship, guidance, and unwavering support throughout my graduate journey. His encouragement and scientific insight have greatly shaped both this research and my growth as a scientist. I am equally grateful to my current and former supervisory committee members, Dr. Demian Ifa, Dr. Gerald Audette, Dr. Ryan Hili, Dr. Yi Sheng, and Dr. Lusia Sepiashvili, as well as my internship supervisor, Dr. Kerene Brown, whose expertise and thoughtful feedback helped strengthen this work.

I would also like to thank Cristina Lento for her kindness and support in navigating both the academic and personal challenges during my graduate school. Your words of advice and encouragement have truly meant a lot to me. My sincere appreciation also goes to the past and present members of the Wilson Lab: Banafsheh, Esther, Vimanda, Joe, Alex, Venita, Erica, Chris, Karl, and Rhona. Thank you for fostering such a collaborative and welcoming environment.

On a personal note, I owe my deepest gratitude to my parents, Arjumand Maqsood and Mona Maqsood, whose courageous decision to immigrate to Canada created opportunities that made this achievement possible. Their sacrifices, unwavering belief in me, endless prayers, and unconditional love have been the foundation of every success in my life. I am deeply honoured to be the first person in my family to earn a PhD, a milestone that is as much theirs as it is mine.

To my sister, Fatima, thank you for being so much more than a sister. You have been an incredible role model and a loving caretaker to my daughter from the time she was only three months old. Your selfless support and countless hours of babysitting allowed me to continue pursuing my research, and I could not have completed this journey without you.

To my brothers, thank you for standing by me through some of the most difficult moments of my personal life. Your encouragement and support gave me strength when I needed it most.

Most importantly, I thank my daughter, Aliya. You were only three months old when I returned to my PhD after maternity leave, and in many ways, we completed this journey together. You unknowingly attended virtual classes, group meetings, and countless hours of writing and research by my side. While you may never remember those moments, they are memories I will always cherish. You have been my greatest source of motivation, reminding me every day why perseverance matters. I hope that one day, when you are old enough to read these words, you will know that every sacrifice was made with love and with the hope of making you proud.

Finally, I am grateful to everyone who has been part of my journey. Whether through encouragement, friendship, challenge, or adversity, each person and experience has shaped my resilience and contributed to the person I am today. This achievement reflects not only my own efforts but also the support and influence of everyone who helped me along the way.

Table of Contents

Abstract ..... **iii**
Acknowledgements ..... **iii**
Table of Contents ..... **iiiv**
List of Figures ..... **vi**
List of Abbreviations ..... **vii**
List of Publications ..... **vii**

CHAPTER 1 ..... **1**
INTRODUCTION **1**
1.1. Proteins as Therapeutic Targets 1
1.2. Mass Spectrometry 1
1.2.1. Ion Source: Electrospray Ionization *2*
1.2.2. Mass Analyzer: A Hybrid Quadrupole and Time-Of-Flight (Q-TOF) *4*
1.2.3. Gas-phase Ion Mobility Separation *8*
1.2.4. Collision-Induced Dissociation of Peptides *11*
1.3. Hydrogen-Deuterium Exchange Mass Spectrometry 13
1.3.1. Fundamentals of Amide Hydrogen Exchange *14*
1.3.2. HDX in ordered and disordered proteins *17*
1.3.3. Bottom-Up Workflow for HDX-MS *19*
1.3.4. Data Interpretation for HDX-MS *22*
1.4. Quantitative Mass Spectrometry 24
1.5. Research Objectives 25

CHAPTER 2 ..... **26**
Hydrogen–deuterium exchange mass spectrometry reveals mutation-specific conformational remodelling in STAT5B SH2 domain **26**
2.1. Summary 27
2.2. Introduction 27
2.3. Experimental procedures 29
2.3.1. Expression and purification of STAT5B variants *29*
2.3.2. Detection using Native Mass Spectrometry *30*
2.3.3. Continuous flow injection TRESI-HDX (CFI-TRESI-HDX) *30*
2.3.4. Bottom-up Hydrogen-Deuterium Exchange Mass Spectrometry *30*
2.4. Results and Discussion 31
2.4.1 SH2 domain mutations produce distinct stabilization effects within the pY+3 pocket. *31*
2.4.2. Non-SH2 domain mutations reveal allosteric effects on the SH2 domain and divergent dynamic outcomes *35*
2.5. Conclusion 36

CHAPTER 3 ..... **39**
Millisecond Hydrogen–Deuterium Exchange Mass Spectrometry Reveals Kinase-Specific Conformational Biases within the Tau Ensemble **39**
3.1. Summary 40
3.2. Introduction 40
3.3. Experimental Methods 42
3.3.1. Expression and purification of Tau *42*

3.3.2. Expression and purification of GSK3β *42*
3.3.2. Phosphorylation of tau using GSK3β, MARK4, and Fyn kinases. *43*
3.3.3. Identification of tau using Native Mass Spectrometry *43*
3.3.4. Continuous flow injection TRESI-HDX (CFI-TRESI-HDX) *43*
3.3.5. CFI-TRESI-HDX with trap column (CFIT-TRESI-HDX) *43*
3.3.6. CFI-TRESI-HDX with complete LC separation (CFID-TRESI-HDX) *44*
3.3.7. Circular Dichroism (CD) spectroscopy of tau *44*
3.4. Results and Discussion 44
3.4.1 Optimization and implementation of an automated CFIT-TRESI-HDX for tau analysis *44*
3.4.2. Automated CFIT-TRESI-HDX reproduces previously observed conformational effects of GSK3β-mediated tau phosphorylation *45*
3.4.3. Identification of MARK4 and Fyn-Mediated Tau Phosphorylation *47*
3.4.4. Kinase-specific phosphorylation produces distinct phospho-tau conformational ensembles *47*
3.5. Conclusion 51

CHAPTER 4 52
Development of a Targeted LC-MS Proteomics Workflow for Quantitative Analysis of Clinical Protein Biomarkers in Human Serum 52
4.1. Summary 53
4.2. Introduction 53
4.3. Experimental procedures 54
4.3.1. Proteolysis of human albumin and thyroglobulin *54*
4.3.2. Solid-phase extraction of the digested protein biomarkers *55*
4.3.3. Quantitation of human albumin and thyroglobulin using MRM-HR mass spectrometry *55*
4.4. Results and Discussion 55
4.4.1. Development of a Simplified Bottom-Up Proteomics Workflow *55*
4.4.2. LC-MS Method Optimization *57*
4.4.3. Quantitation of Human Albumin *59*
4.4.4. Quantitation of Thyroglobulin (TG) *60*
4.5. Conclusion 61
CHAPTER 5 63
Conclusion and Future Work 63
5.1. Conclusions 63
5.2 Limitations and Future Directions 64
Reference 66
Appendices 76
Appendix A: Supplementary information for Chapter 2. 76
Appendix B: Supplementary information for Chapter 3. 86
Appendix C: Supplementary information for Chapter 4. 91

List of Figures

Figure 1.1 | Schematic representing the basic components of a Mass Spectrometer.....2
Figure 1.2 | Schematic depiction of an electrospray ionization source operated under positive ion mode 3
Figure 1.3 | Summary of the ESI mechanism 4
Figure 1.4 | Schematic representation of a quadrupole time-of-flight (QToF) mass spectrometer 5
Figure 1.5| Schematic of the Waters Synapt G2-S mass spectrometer 6
Figure 1.6 | Summary of the various modes of tandem MS experiments using CID 7
Figure 1.7 Schematic comparison of the four major ion mobility spectrometry (IMS) technologies 9
Figure 1.8 | Cyclic IMS (cIMS) instrument design in Waters Select Series mass spectrometer 11
Figure 1.9 | Nomenclature for peptide fragmentation. 12
Figure 1.10 | A schematic representation of the mobile proton model 13
Figure 1.11 | Schematic representation of exchangeable hydrogen atoms within a peptide backbone 14
Figure 1.12 | Mechanisms of acid- and base-catalyzed HDX reaction 15
Figure 1.13 | Dependence of the intrinsic amide hydrogen exchange rate constant (k_{ex}) on solution pH for an unstructured peptide 16
Figure 1.14 | Schematic representing the EX1 and EX2 HDX kinetics 18
Figure 1.15 | Schematic representation of the bottom-up HDX-MS workflow 20
Figure 1.16 | Schematic representations of HDX-MS setups 22
Figure 1.17 | Interpretation of HDX-MS data 23
Figure 2.1 | Three-dimensional structural organization of STAT5B wildtype and its SH2 domain 28
Figure 2.2 | Differential HDX uptakes (%) were calculated between apo and phosphotyrosine peptide-bound STAT5B 31
Figure 2.3 | Differential HDX uptakes (%) were calculated between STAT5B wildtype and $STAT5B^{N642H}$ 32
Figure 2.4 | Differential HDX uptakes (%) were calculated between STAT5B wildtype and disease-associated mutations within the SH2 domain 34
Figure 2.5 | Differential HDX uptakes (%) were calculated between STAT5B wildtype and disease-associated mutations outside the SH2 domain 36
Figure 2.5 | Proposed model illustrating the effects of disease-associated STAT5B mutations on SH2 domain... 37
Figure 3.1 | Discrete time point mode of operation with LC separation 44
Figure 3.2 | Differential CFI-TRESI-HDX on GSK3β-mediated tau hyperphosphorylation 45
Figure 3.3 | Differential CFI-TRESI-HDX on phosphorylated tau 47
Figure 3.4 | Monitoring the spectrum from CD spectroscopy of native and phosphorylated tau 49
Figure 4.1 |Base Peak Chromatogram demonstrating the increase in peptide intensity upon SPE cleanup 56
Figure 4.2 | A total ion chromatogram of digested proteins of (a) Albumin and (b) human Thyroglobulin over a 5-minute LC gradient. 57
Figure 4.3 | Calibration curve for a characteristic peptide for the quantitation of human Albumin using five calibrants, two quality controls and an internal standard. 58
Figure 4.4 | Calibration curve for a characteristic peptide for the quantitation of human Thyroglobulin using six calibrants, two quality controls and an internal standard 60

List of Abbreviations

Å	Angstrom
ATP	Adenosine Triphosphate
TCEP	isopropyl β-D-thiogalactopyranoside
SDS-PAGE	Sodium Dodecyl Sulfate-Polyacrylamide Gel Electrophoresis
EAD	Electron-Activated Dissociation
CID	Collision-Induced Dissociation
Cryo-EM	Cryogenic Electron Microscopy
Da	Dalton
DMSO	Dimethyl Sulfoxide
D_2O	Deuterium Oxide
ECD	Electron Capture Dissociation
ESI	Electrospray Ionization
ETD	Electron Transfer Dissociation
k_{ex}	Intrinsic Exchange Rate Constant
k_{op}	Opening Rate Constant
MS/MS	Tandem Mass Spectrometry
LC-MS/MS	Liquid Chromatography-Tandem Mass Spectrometry
AD	Alzheimer's Disease
MALDI	Matrix-Assisted Laser Desorption/Ionization
MRM	Multiple Reaction Monitoring
MS	Mass Spectrometry
m/z	Mass-to-Charge Ratio
NMR	Nuclear Magnetic Resonance
PF	Protection Factor
pY	Phosphotyrosine
PTM	Post-Translational Modification
Q0	Quadrupole 0
Q1	Quadrupole 1
Q2	Collision Cell Quadrupole
QTOF	Quadrupole Time-of-Flight
QQQ	Triple Quadrupole
EX1	Unimolecular Exchange
EX2	Bimolecular Exchange
HDX	Hydrogen-Deuterium eXchange
HDX-MS	Hydrogen-Deuterium eXchange Mass Spectrometry
HPLC	High-Performance Liquid Chromatography
IDP	Intrinsically Disordered Protein
IDR	Intrinsically Disordered Region
IM-MS	Ion Mobility-Mass Spectrometry
IMS	Ion Mobility Separation
k_{ch}	Intrinsic Chemical Exchange Rate Constant
k_{obs}	Observed Exchange Rate Constant
RF	Radio Frequency
RMSD	Root Mean Square Deviation
SH2	Src Homology 2
STAT5B	Signal Transducer and Activator of Transcription 5B
TOF	Time-of-Flight
GST	Glutathione S-Transferase
LB	Luria Broth
GSK3β	glycogen synthase kinase 3β
MARK4	microtubule affinity-regulating kinase 4
NFTs	Neurofibrillary Tangles
PHFs	Paired Helical Filaments
OD	Optical Density
XL-MS	Cross-Linking Mass Spectrometry
CD	Circular Dichroism
ΔG	Change in Gibbs Free Energy
TG	Thyroglobulin
SPE	Solid-Phase Extraction
QC	Quality Control

List of Publications

1. **Maqsood A**, Ashraf QF, Lento C, de Araujo ED, Gunning P, Wilson DJ (2026) “Hydrogen–deuterium exchange mass spectrometry reveals mutation-specific conformational remodelling in STAT5B SH2 domain”, *JBC. (under review)*
2. **Maqsood A**, Lento C, Wilson DJ (2026) “Millisecond Hydrogen Deuterium Exchange for Characterization of Disordered Conformational Dynamics and Weak Binding Interactions”, *Protein Sci. (under review)*
3. Che X, MacLellan A, **Maqsood A**, AlSafadi E, Wang TY, Krylov SN (2026) “Signal Nonadditivity Limits Backscattering Interferometry for Quantitative Determination of Equilibrium Dissociation Constants”, *ACS. (under review)*
4. Haas-Neill L, Meneksedag-Erol D, **Chaudhry A**, Novoselova M, Ashraf QF, de Araujo ED, Wilson DJ and Rauscher S (2025) "The structural influence of the oncogenic driver mutation N642H in the STAT5B SH2 domain", *Protein Sci*.
5. Anacleto J**,** Lento C**,** Sarpe V, **Maqsood A**, Mehrazma B, Schriemer D and Wilson DJ (2023) "Apparatus for Automated Continuous Hydrogen Deuterium Exchange Mass Spectrometry Measurements from Milliseconds to Hours", *Anal Chem*.

CHAPTER 1

INTRODUCTION

1.1. Proteins as Therapeutic Targets

Proteins are among the most abundant and versatile biomolecules in living organisms, responsible for regulating virtually every cellular process. Their ability to perform such diverse functions arises from their unique three-dimensional structures and conformational flexibility. Even subtle structural alterations, including point mutations or changes in post-translational modifications, can significantly affect protein behaviour and contribute to disease pathogenesis.

As a result, considerable efforts across multiple disciplines have been directed toward understanding protein structure, dynamics, and the formation of pathological species to facilitate the development of effective therapeutic strategies. Traditional structural biology techniques, including X-ray crystallography, Nuclear Magnetic Resonance (NMR) spectroscopy, and Cryogenic Electron Microscopy (Cryo-EM), have been instrumental in advancing our understanding of protein structure and function.[1–3] However, these approaches often face challenges when applied to heterogeneous, weakly populated and/or conformationally flexible proteins and protein complexes

In addition to requiring highly pure and concentrated samples, such techniques frequently struggle to characterize intrinsically disordered regions (IDRs) and intrinsically disordered proteins (IDPs). These highly flexible regions are often artificially constrained by crystal packing in X-ray crystallography, obscured by severe spectral overlap in NMR experiments, or averaged out during Cryo-EM image reconstruction.[4–6] As a result, important structural and dynamic information can remain inaccessible using conventional structural biology methods.

To address these limitations, advanced mass spectrometry (MS)-based approaches, including Hydrogen-Deuterium Exchange Mass Spectrometry (HDX-MS), Cross-Linking Mass Spectrometry (XL-MS), and native (or intact) MS, have emerged as powerful tools for structural characterization.[7,8] These techniques provide valuable insights into subtle conformational biases, rapidly exchanging intermediate states, and weak molecular interactions while requiring substantially lower sample concentrations than traditional structural methods. Furthermore, the high sensitivity, specificity, and throughput of MS-based techniques have enabled the detection and quantification of a broad range of biomolecules. Beyond structural characterization, these capabilities have driven the widespread adoption of MS-based workflows in proteomics, biomarker discovery, and clinical diagnostics, thereby supporting the development of novel therapeutics and precision medicine approaches.

1.2. Mass Spectrometry

Mass spectrometry (MS) is an analytical technique that measures the mass-to-charge (*m/z*) ratio of gas-phase ions and has become an indispensable tool for the characterization of proteins and other biomolecules. The foundations of modern mass spectrometry were established through the pioneering work of J.J. Thomson, who demonstrated the existence of charged particles and developed the first mass spectrograph in the early twentieth century.[9] Subsequent advances by Francis Aston, Arthur Dempster, and others enabled increasingly

accurate mass measurements and isotope determination.[10,11] Although early mass spectrometers were largely limited to the analysis of small molecules, the development of soft ionization techniques, most notably electrospray ionization (ESI) by Fenn and co-workers and matrix-assisted laser desorption/ionization (MALDI) by Karas and Hillenkamp in the late 1980s, revolutionized the field by enabling the transfer of intact biomolecules into the gas phase.[9,12] These advances established mass spectrometry as a central technique in structural biology and proteomics, allowing the analysis of proteins, protein complexes, post-translational modifications, and conformational dynamics.[13]

Despite the wide range of mass spectrometer designs currently available, all instruments share the same fundamental components (Figure 1.1).[14] Sample introduction begins at the inlet, where analytes are converted into gas-phase ions in the ion source. These ions are subsequently directed into the mass analyzer, which separates them according to their m/z ratio using electric and/or magnetic fields under high-vacuum conditions. The separated ions are then measured by a detector, which converts ion arrival events into electrical signals proportional to ion abundance.[13,15] Finally, the acquired signals are processed to generate a mass spectrum, in which ion intensity is plotted as a function of m/z. The performance of a mass spectrometer is largely determined by the characteristics of its ion source, mass analyzer, and detector, with each component influencing parameters such as sensitivity, mass accuracy, resolution, and dynamic range (i.e. the ratio between the strongest and weakest ion signals detected by the mass spectrometer).[13,16] Consequently, over the years, numerous instrument configurations have been developed to address specific analytical challenges, including the characterization of large biomolecules, complex mixtures, and low-abundance species.[13]

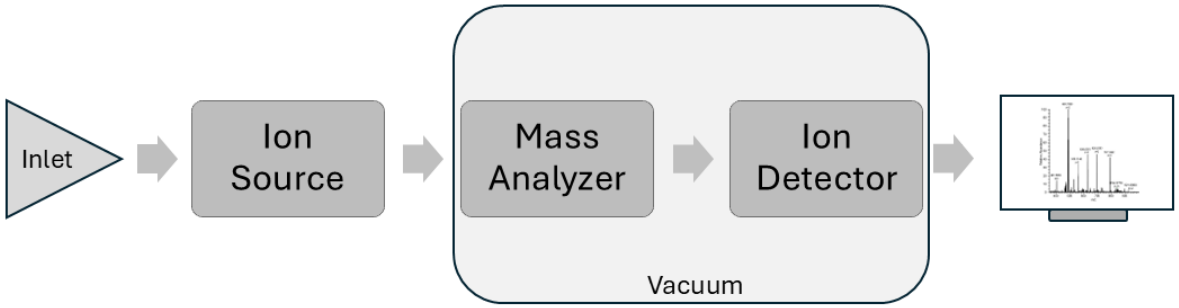


Figure 1.1 | Schematic representing the basic components of a Mass Spectrometer. Analytes are introduced into the instrument through an inlet and converted into gas-phase ions at the ion source. The generated ions are subsequently separated according to their mass-to-charge (m/z) ratio by the mass analyzer under high-vacuum conditions before being measured by the ion detector. The resulting ion signals are processed to generate a mass spectrum, which provides information on the molecular masses and relative abundances of the detected species.

1.2.1. Ion Source: Electrospray Ionization

Electrospray ionization (ESI) is one of the most widely used ionization techniques in biological mass spectrometry due to its ability to transfer large biomolecules from solution into the gas phase with minimal fragmentation. The technique is particularly well-suited for the analysis of peptides, proteins, and non-covalent protein complexes and is readily interfaced with liquid chromatography systems.

In ESI, a solution containing the analyte is passed through a metal capillary held at a high electric potential relative to the inlet of the mass spectrometer (Figure 1.2).[17] The applied electric field causes the liquid at the capillary tip to emit into a cone-shaped structure, commonly referred to as a Taylor cone, from which a fine spray of charged droplets is emitted. As the droplets travel toward the mass spectrometer inlet, solvent evaporation leads to a progressive increase in surface charge density. When electrostatic repulsion exceeds the stabilizing force provided by surface tension, the droplets undergo Coulomb fission, producing a series of smaller charged droplets.[17]

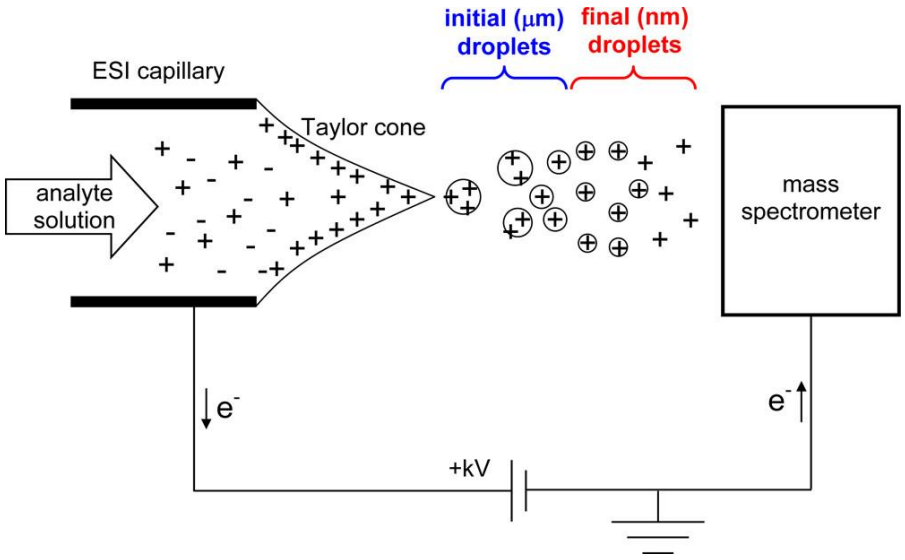


Figure 1.2 | Schematic depiction of an electrospray ionization source operated under positive ion mode. Adapted with permission from Konermann et al. (2013), © 2013 American Chemical Society.[17]

The Rayleigh limit describes the maximum charge that a droplet can sustain before Coulomb fission occurs:

$$z_R = (8\pi/e)\sqrt{(\varepsilon_0 \gamma r^3)} \qquad (1.1)$$

where z_R is the maximum droplet charge, e is the elementary charge, ε_0 is the permittivity of free space, γ is the surface tension of the solvent, and r is the droplet radius.

Although the exact mechanism by which gas-phase ions are formed remains a topic of discussion, the Charged Residue Model (CRM) is generally accepted for folded proteins (Figure 1.3 b). In this model, repeated cycles of solvent evaporation and Coulomb fission generate progressively smaller droplets until a single analyte molecule remains. Complete solvent evaporation then produces a gas-phase ion carrying the residual charge of the droplet. For smaller molecules, ion formation is more commonly described by the Ion Evaporation Model (IEM), in which ions are emitted directly from the droplet surface under a sufficiently strong electric field (Figure 1.3 a). A third mechanism, known as the Chain Ejection Model (CEM), has been proposed for unfolded proteins and other flexible polymers that can partially protrude from the droplet surface before being ejected into the gas phase (Figure 1.3 c).

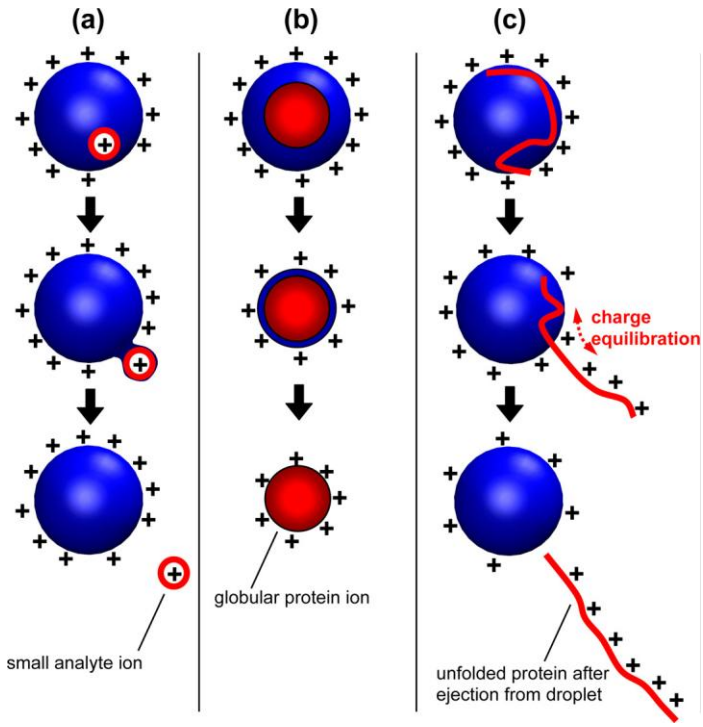


Figure 1.3 | Summary of the ESI mechanism. (a) Ion Ejection Model (IEM), (b) Charge Reduced Model (CRM), and (c) Chain Ejection Model (CEM). Adapted with permission from Konermann et al. (2013), © 2013 American Chemical Society.[17]

A key advantage of ESI is its ability to generate multiply charged ions. The observed mass-to-charge ratio of an ion is described by:

$$\frac{m}{z} = \frac{M + zH}{z} \qquad (1.2)$$

where *m/z* is the mass-to-charge ratio, *M* is the molecular mass of the analyte, *z* is the charge state, and H is the mass of a proton. The production of multiple charge states reduces the measured m/z values of large biomolecules, allowing proteins and protein complexes to be analyzed within the operating range of most mass analyzers. The soft ionization characteristics of ESI, together with its compatibility with aqueous solutions and liquid chromatography, have made it the ionization method of choice for many structural biology applications, including HDX-MS, native MS, and bottom-up proteomics.

1.2.2. Mass Analyzer: A Hybrid Quadrupole and Time-Of-Flight (Q-TOF)

By enabling the transfer of intact proteins from solution to the gas phase, ESI overcame many of the mass limitations associated with earlier ionization methods, such as MALDI, and opened the door to routine protein characterization by mass spectrometry.[18] In the 1990s, advances in mass analyzer design led to the development of a hybrid instrument by combining quadrupole and time-of-flight analyzers (Q-TOF), capable of providing high-resolution mass measurement down to the femtomolar range.[16] The Q-TOF mass spectrometer became particularly important for biological applications due to its sensitivity, mass accuracy, and compatibility with tandem mass spectrometry experiments.

The Q-TOF mass spectrometers combine the ion filtering capabilities of a quadrupole mass analyzer with the resolving power of a time-of-flight (TOF) analyzer.[19] In these instruments, the quadrupole acts as either (i) an ion guide, transmitting all ions to the TOF analyzer (MS mode), or (ii) an ion filter, allowing only ions in a predefined mass range to pass through the quadrupole analyzer (MS/MS mode), whereas the TOF analyzer is responsible for measuring the actual masses of the sample ions.[19] The filtered ions are fragmented by inert gas in the collision cell, referred to as collision-induced dissociation (CID) (more details on ion fragmentation and activation are provided later).[20] This configuration provides a significant improvement over conventional triple quadrupole instruments by enabling accurate mass measurements of both precursor and fragment ions while maintaining the ability to perform collision-induced dissociation (CID) experiments. As a result, QTOF platforms have rapidly become established tools for peptide sequencing, protein identification, structural biology, and proteomics applications.

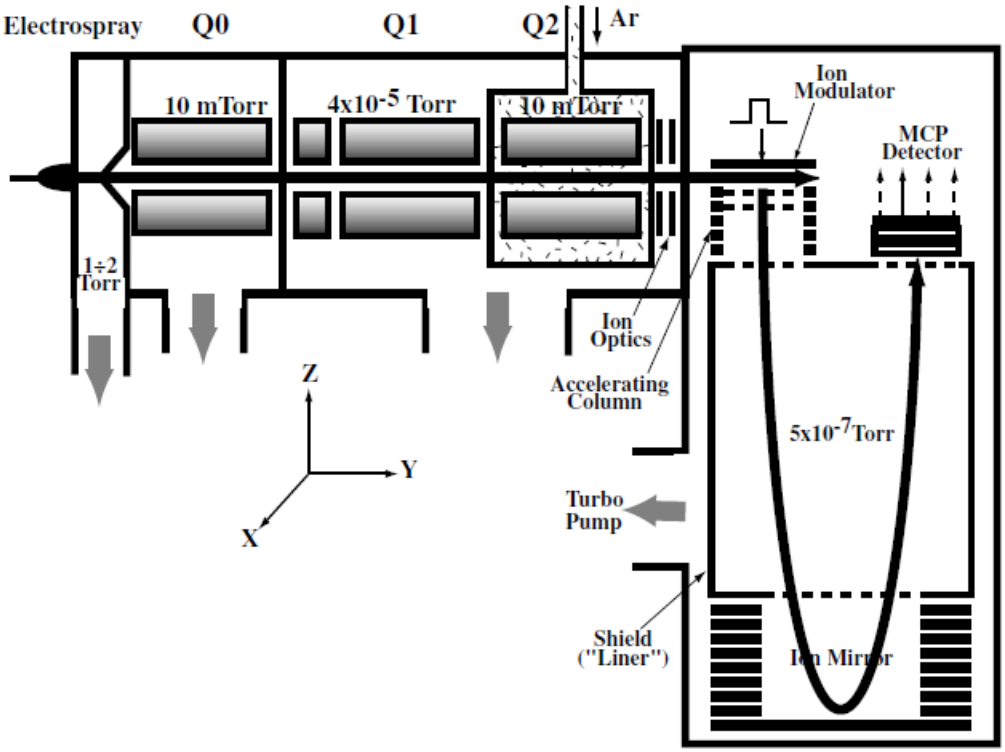


Figure 1.4 | Schematic representation of a quadrupole time-of-flight (QToF) mass spectrometer. Gas-phase ions generated by electrospray ionization are transmitted through the instrument and initially focused by the Q0 quadrupole. The Q1 quadrupole acts as a mass filter, selecting ions based on their mass-to-charge ratio (m/z). Q2 serves as a collision cell containing an inert gas (typically nitrogen) and may be used for collision-induced dissociation (CID) experiments. Following Q2, ions are refocused by ion optics and transferred into the time-of-flight (TOF) analyzer. An ion modulator pulses ions orthogonally into the flight tube, where separation occurs according to m/z. An ion mirror (reflectron) improves mass resolution by compensating for kinetic energy differences between ions prior to detection by a multichannel plate detector. Adapted from Chernushevich et al.[21]

A conventional Q-TOF model consists of an ion-focusing region (Q0), a quadrupole mass filter (Q1), a collision cell (Q2), and a TOF analyzer (Figure 1.4).[21] Following electrospray ionization, ions are transmitted through Q0, where they are cooled and focused using stacks of ring-shaped electrodes known as the ion guides, before

entering Q1. The quadrupole can be operated either as a broadband ion guide or as a mass filter that selectively transmits ions within a preselected mass-to-charge ratio (m/z) range. Currently, many variations of the conventional Q-TOF model exist, including those used in Waters Synapt G2-S and Select Series Cyclic IMS mass spectrometers. These instruments use a step wave ion guide that filters out neutral gas-phase species in the first step, followed by focusing them through a narrow path of electric field (Figure 1.5).[22]

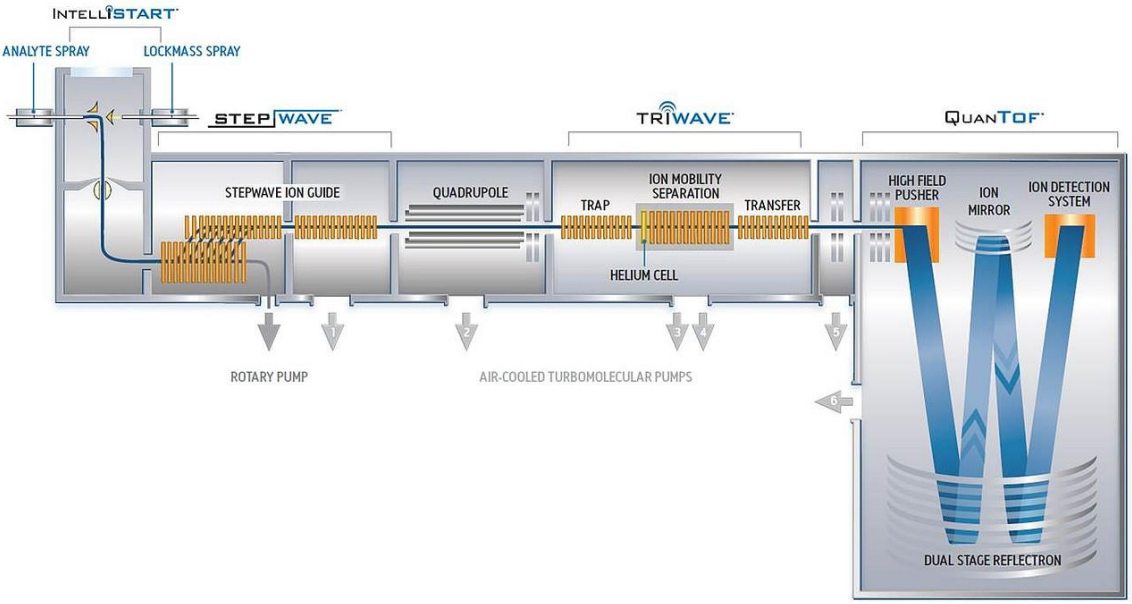


Figure 1.5 | Schematic of the Waters Synapt G2-S mass spectrometer. The addition of the Stepwave ion guide allows the filtering of neutral species while focusing charged analytes into the quadrupole.[9]

Additionally, these instruments allow gas-phase fragmentation and orthogonal separation using three pressurized collision cells with tunable parameters: Trap, Ion Mobility and Transfer cells.[23,24] (Ion Mobility separation is discussed in section 1.1.3) In tandem mass spectrometry (MS^n) experiments, selected precursor ions are fragmented by collisions with an inert gas, typically nitrogen or argon, via collision-induced dissociation (CID). The resulting product ions are then accelerated into the TOF analyzer for mass measurement

The TOF analyzer separates ions according to the time required to traverse a fixed flight path under vacuum. Following acceleration through an electric potential, ions with the same kinetic energy separate as a function of their mass-to-charge ratio, with lower m/z ions reaching the detector before the heavier ones. The relationship between the kinetic energy of the ions and the accelerating voltage is given by:

$$KE = zeV = \tfrac{1}{2}mv^2 \qquad (1.3)$$

where z is the ion charge state, e is the elementary charge, V is the accelerating voltage, m is the mass of the ion, and v is the ion velocity. Since ions are accelerated to approximately equal kinetic energies, their flight time is proportional to the square root of their mass-to-charge ratio:

$$t = L\sqrt{(m/2zeV)} \qquad (1.4)$$

where t is the flight time, and L is the path length.

Modern Q-TOF instruments employ orthogonal acceleration in which ions are continuously introduced from the quadrupole region and periodically pulsed into the TOF analyzer at right angles to their original trajectory. This design significantly improves mass resolution by ensuring that all ions start their TOF journey at the same time with identical kinetic energy. Even with the orthogonal acceleration, ions of the same m/z may contain slight differences in their kinetic energies. Without correction, these speed variations cause the ion peak to broaden, decreasing resolution. Therefore, modern TOF analyzers use a "reflectron" positioned at the end of the flight tube. This reflectron compensates for small differences in kinetic energy among ions with identical m/z by increasing the flight path of faster ions, thereby improving peak focusing and enhancing mass resolution.[21]

Beyond accurate mass measurements, Q-TOF instruments are capable of performing a variety of tandem mass spectrometry scanning mode. In a product ion scan, a precursor ion is selected by Q1, fragmented within Q2, and the TOF analyzer analyzes the resulting product ions. This approach forms the basis of peptide sequencing and structural characterization experiments. Alternative scan modes include precursor ion scans, which identify precursor ions that generate a specific fragment ion, and neutral loss scans, which detect ions undergoing a characteristic neutral loss during fragmentation (Figure 1.6).

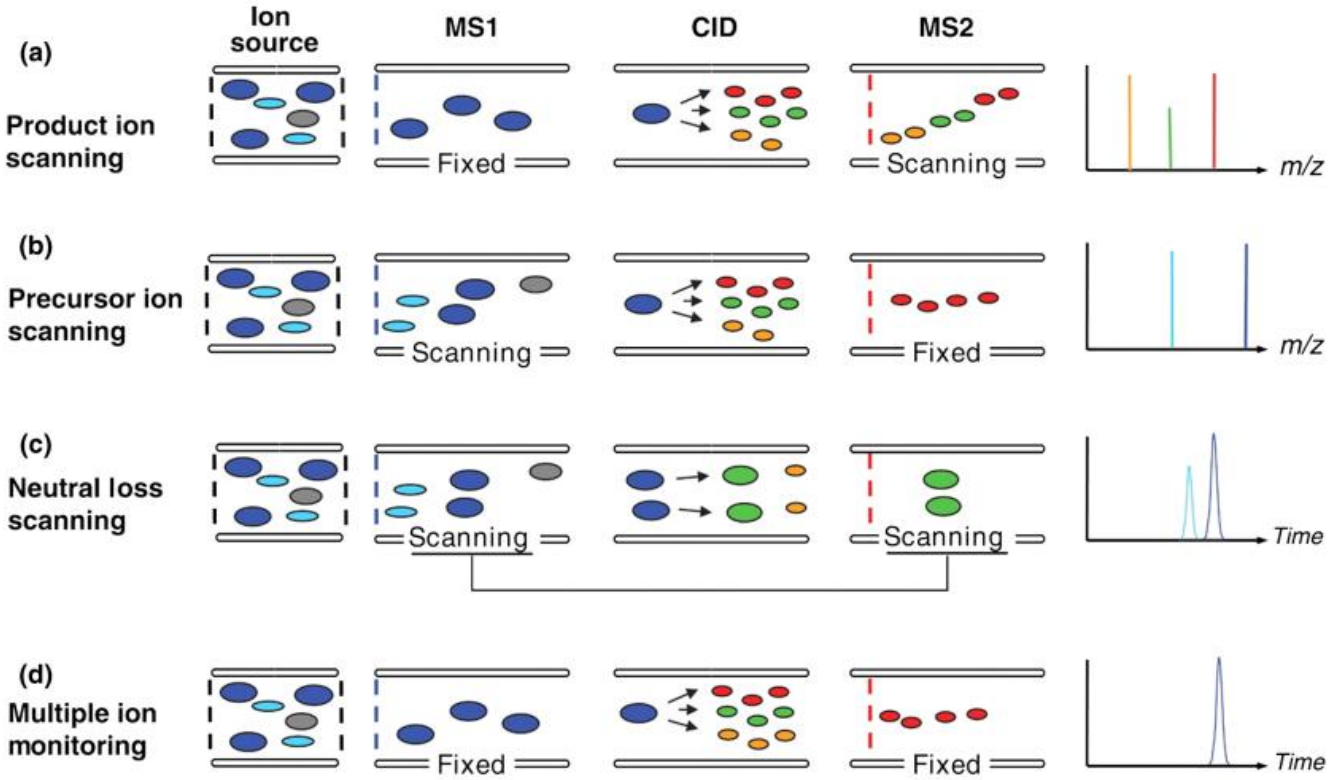


Figure 1.6 | Summary of the various modes of tandem MS experiments using CID. (a) Product ion scan, where a selected precursor ion is fragmented, and the resulting product ions are analyzed. (b) Precursor ion scan, in which precursor ions producing a specific fragment ion are detected. (c) Neutral loss scan, where precursor ions undergoing a defined neutral loss are identified through synchronized scanning of both mass analyzers. (d) Multiple reaction monitoring (MRM), in which specific precursor-to-product ion transitions are monitored for targeted and sensitive analyte detection. Adapted from Maher *et al.*[25]

These scan modes form the basis of many mass spectrometry workflows used throughout this thesis. Product ion analysis is routinely employed for peptide identification and characterization following CID and plays an important role in HDX-MS workflows, where peptide-level information is required to localize deuterium incorporation within a protein sequence. In contrast, multiple reaction monitoring (MRM) is a targeted MS/MS approach in which predefined precursor-to-product ion transitions are selectively monitored. By restricting data acquisition to specific transitions, MRM provides enhanced sensitivity, selectivity, and quantitative reproducibility, making it particularly useful for targeted proteomics and biomarker quantification.

1.2.3. Gas-phase Ion Mobility Separation

Ion mobility spectrometry (IMS) separates ions according to their mobility through an inert buffer gas in the presence of an applied electric field (*E*). Under these conditions, ions drift through the gas at a velocity (v_d), referred to as the drift velocity, which is directly proportional to their mobility (*K*).[26,27] The following equation describes this relationship:

$$K = \frac{v_d}{E} \qquad (1.5)$$

In a constant electric field, ions with larger collision cross sections (CCS) experience more frequent collisions with the buffer gas as they pass through the drift tube. As a result, these ions travel more slowly and exhibit lower mobilities (*K*) than smaller or more compact species. The mobility of the ions is generally reported as a reduced mobility, K_0, to account for differences in experimental parameters (i.e., pressure and temperature):

$$K_0 = K\,(\frac{P}{760})(\frac{273.15}{T}) \qquad (1.6)$$

Unlike MS alone, IMS-MS can also provide information on the collision cross-section (CCS or Ω) of the analytes to reflect their size and shape. This measurement can be exceptionally useful to obtain structural insights into conformationally distinct species with similar m/z values. It can be calculated using the Mason-Schamp equation below:

$$\Omega = \frac{\frac{3}{16}ze(\frac{2\pi}{\mu k_b T})^{\frac{1}{2}}}{N_0 K_0} \qquad (1.7)$$

where *z* is the charge, N_0 is gas density, μ is the reduced mass of the collision partners, k_b is the Boltzmann constant, and Ω is the collision cross section.[28,29]

Currently, four major ion mobility spectrometry (IMS) technologies are widely used: drift tube ion mobility spectrometry (DTIMS), travelling wave ion mobility spectrometry (TWIMS), trapped ion mobility spectrometry (TIMS), and field asymmetric ion mobility spectrometry (FAIMS) (Figure 1.7).[30] The following paragraphs provide a brief overview of each technique, with particular emphasis on TWIMS, as it is the ion mobility platform used throughout the experimental work presented in this thesis. Each approach offers distinct advantages and limitations, making them suitable for different analytical applications.

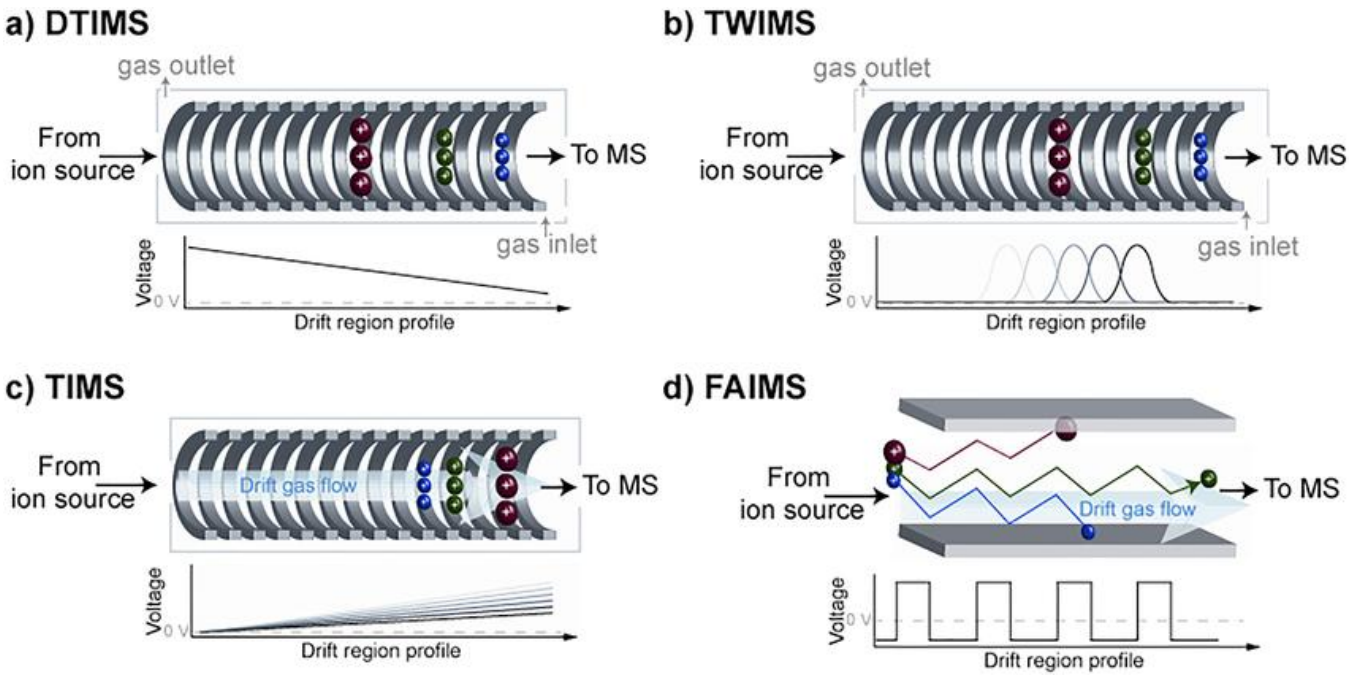


Figure 1.7 Schematic comparison of the four major ion mobility spectrometry (IMS) technologies. (a) Drift tube ion mobility spectrometry (DTIMS) separates ions based on their drift times through a buffer gas under a uniform electric field. (b) Travelling wave ion mobility spectrometry (TWIMS) separates ions using a series of moving voltage waves that propel ions through a gas-filled mobility cell according to their mobility. (c) Trapped ion mobility spectrometry (TIMS) traps ions by balancing an opposing electric field against a flowing gas stream and subsequently elutes them according to mobility. (d) Field asymmetric ion mobility spectrometry (FAIMS) separates ions based on differences in mobility under alternating high- and low-field conditions between two electrodes. Adapted from Laurence *et al*.[30]

DTIMS is considered the most fundamental form of ion mobility. Ions are pulsed into a drift tube containing an inert gas (without a directional flow) and migrate through a uniform electric field (Figure 1.7a). Separation occurs because compact ions experience fewer collisions and travel faster than extended conformations.

The ion drift time (t_d) is given by:

$$t_d = \frac{L}{KE} \qquad (1.8)$$

where $L$is the drift tube length. Because the electric field is constant and well-defined, CCS values can be calculated directly from first principles using the Mason–Schamp equation without external calibration. This direct relationship makes DTIMS the reference platform for generating highly accurate CCS measurements. However, achieving high resolving power typically requires long drift tubes and relatively large instrument footprints.

Unlike DTIMS, which uses a uniform electric field, TWIMS separates ions using a sequence of oscillating electric fields to generate voltage waves that propagate through a gas-filled mobility cell towards the mass analyzer (Figure 1.7b). Ions are transported by repeatedly climbing these moving potential waves while colliding with the buffer gas.

In the Waters Synapt G2 instrument utilized in this dissertation, alternating phases of radiofrequency (RF) voltages focus the ions into radially confined packets while direct current (DC) voltage pulses generate the travelling wave. More mobile ions remain closer to the crest of the wave and move or "roll over" the wave rapidly, whereas less mobile ions undergo more collisions, fall behind the wave, and exhibit longer time to reach the mass analyzer.[31]

Unlike DTIMS, there is no simple analytical equation relating drift time directly to CCS because ion motion is governed by repeated interactions with moving electric field gradients. Therefore, CCS values must be determined using calibration standards with known CCS values.[27]

Even though it has lower resolving power than DTIMS, TWIMS became widely adopted because it could be incorporated into existing Q-TOF instruments without requiring the long drift tubes used in DTIMS systems. Additionally, it offers high sensitivity, compact instrument design, and compatibility with LC-MS workflows, making it highly popular in the fields of structural biology, proteomics, metabolomics, and lipidomics.[32–35]

More recently, the principles of TWIMS have been enhanced through the development of cyclic ion mobility spectrometry (cIMS) (Figure 1.8).[36] In this configuration, ions travel through a closed-loop travelling wave mobility device, allowing them to complete multiple passes around the mobility cell before mass analysis. The cyclic IMS platform, implemented on the Waters Select Series Cyclic IMS system, can therefore enable advanced experiments such as mobility selection, ion activation, and multistage ion mobility (IMS^n) analyses.[37] Mobility resolving powers approaching 750 have been reported following multiple passes through the cyclic device, enabling the separation of structurally similar ions that would otherwise be unresolved using conventional single-pass TWIMS measurements.[37] In the bottom-up HDX workflow (Section 1.3), coupling cIMS with liquid chromatography (LC) can significantly boost the protein sequence coverage compared to Waters Synapt G2. However, longer residence times in the cIMS cell can cause heat-induced ion activation and fragmentation, resulting in a sensitivity loss, necessitating additional optimizations when using multi-pass experiments.[38]

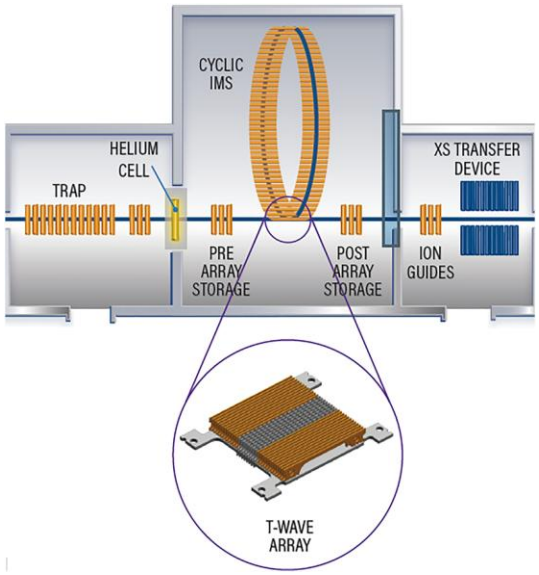


Figure 1.8 | Cyclic IMS (cIMS) instrument design in Waters Select Series mass spectrometer. The closed loop cIMS device, with a path length of 98 cm, is positioned orthogonally to the main ion optical axis. Adapted from Riches *et al*.[36]

Although DTIMS and TWIMS are the most relevant IMS technologies for the studies presented in this thesis, TIMS and FAIMS are also among the most widely used IMS variants. TIMS separates ions by trapping them within an electric field that opposes a flowing buffer gas and subsequently releasing them according to their mobilities, resulting in high resolving power and sensitivity (Figure 1.7c).[39] FAIMS employs a fundamentally different approach, separating ions based on differences in mobility under alternating high- and low-electric field conditions (Figure 1.7d). By selectively transmitting ions at specific compensation voltages, FAIMS improves selectivity and reduces chemical background in complex mixtures.[40] Due to their distinct separation mechanisms, both techniques have become valuable tools for a wide range of mass spectrometry applications, particularly in proteomics and structural biology.[27]

1.2.4. Collision Induced Dissociation of Peptides

In bottom-up proteomics, proteins are enzymatically digested into peptides that are subsequently analyzed by tandem mass spectrometry (MS/MS). During MS/MS, selected peptide precursor ions are activated to induce fragmentation, generating product ions that can be used to determine peptide sequence and identify post-translational modifications. The resulting fragmentation patterns form the basis of peptide and protein identification in modern proteomics workflows.

Fragmentation begins with ion activation, a process in which energy is deposited into a gas-phase ion, increasing its internal energy. Several activation methods have been developed, including collisions with neutral gas molecules, interactions with electrons, and photon-based activation. Among these, collision-induced dissociation (CID) remains the most widely used fragmentation technique in Q-TOF instruments due to its robustness and compatibility with high-throughput proteomic analyses. In CID, ions are accelerated into a collision cell containing an inert gas, typically argon or nitrogen. Repeated low-energy collisions convert a portion of the ion's kinetic energy into internal vibrational energy. As internal energy accumulates, the ion eventually reaches a critical energy threshold and undergoes unimolecular dissociation.

The overall process can be represented as:

$$AB^{+} + M \rightarrow (AB^{+})^{*} + M \rightarrow A^{+} + B + M \qquad (1.9)$$

where AB^{+} represents the precursor ion, M is the neutral collision gas, $(AB^{+})^{*}$ is the activated ion, and A^{+} and B are the resulting charged and neutral fragments, respectively. Because the deposited energy is rapidly redistributed throughout the molecule prior to bond cleavage, CID is generally considered an ergodic fragmentation process. Consequently, larger molecules such as peptides and proteins often require greater activation energies than smaller molecules due to their larger number of vibrational degrees of freedom.

For peptides, fragmentation occurs primarily along the amide backbone, generating a series of structurally informative product ions. The nomenclature introduced by Roepstorff and Fohlman and later modified by Biemann classifies peptide fragments according to the site of backbone cleavage (Figure 1.9).[41] Cleavage toward the N-terminus generates a-, b-, and c-type ions, while cleavage toward the C-terminus results in x-, y-, and z-type ions. Under CID conditions, fragmentation occurs predominantly through the formation of b- and y-type ions, which are the primary fragments used for peptide sequence determination. Secondary fragmentation pathways may also occur, resulting in neutral losses such as ammonia (-17 Da) and water (-18 Da), as well as the formation of a-ions through carbon monoxide loss from b-ions. Smaller diagnostic ions, including immonium ions, can provide additional evidence for the presence of specific amino acid residues within a peptide sequence.[15,41]

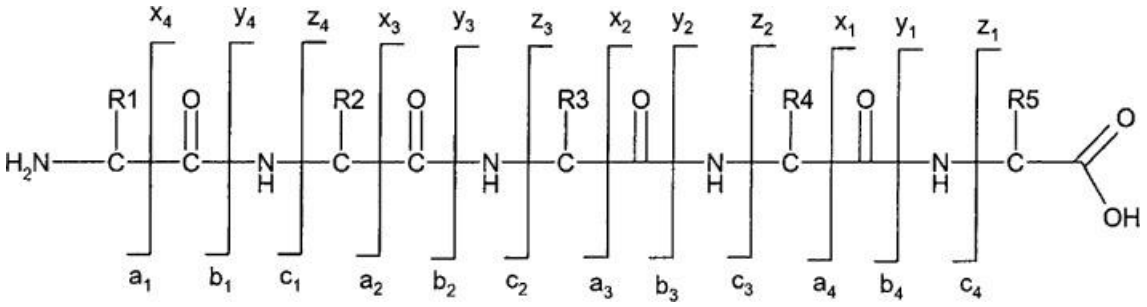


Figure 1.9 | Nomenclature for peptide fragmentation.

The fragmentation behaviour observed during CID is commonly described by the mobile proton model (Figure 1.10).[42] In the gas phase, protons are not necessarily localized to a single site but can migrate along the peptide backbone when sufficient internal energy is available. Protonation of backbone amide groups weakens the adjacent peptide bond, facilitating cleavage and formation of b- and y-type fragments. Peptides containing highly basic residues, particularly arginine, often require higher collision energies because these residues strongly retain protons, limiting proton mobility and reducing fragmentation efficiency. This model successfully explains many of the sequence-dependent fragmentation patterns observed in peptide CID spectra.

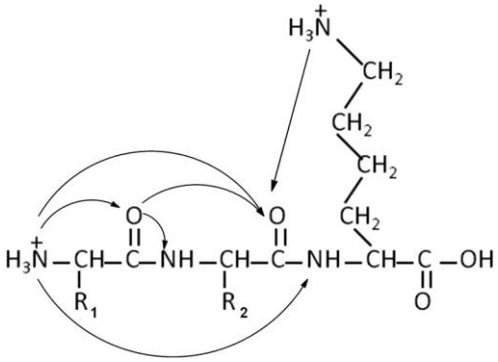


Figure 1.10 | A schematic representation of the mobile proton model. Adapted from Boyd *et al*.[42]

Although CID remains the standard approach for peptide identification, alternative fragmentation methods generate different product ion series. Electron capture dissociation (ECD) and more recent electron-based activation methods, such as electron-activated dissociation (EAD), predominantly cleave the N–C_α bond, producing c- and z-type ions. Because electron-based dissociation occurs on a much shorter timescale than CID, labile post-translational modifications and deuterium labels are often preserved, making these techniques attractive for structural biology and HDX-MS applications.

The Waters Synapt platform used throughout this thesis incorporates collision cells both before and after the ion mobility region, allowing fragmentation to be performed in either the Trap or Transfer cell following quadrupole precursor selection. When coupled with ion mobility separation, precursor ions can first be separated according to their shape and charge before fragmentation, reducing spectral overlap and improving peptide identification in complex mixtures. This additional dimension of separation is particularly beneficial in HDX-MS experiments to improve sequence coverage as well as the sensitivity of low-abundant species.

While fragmentation is essential for peptide identification, excessive ion activation can be detrimental in HDX-MS workflows. Increased collision energies may promote gas-phase structural rearrangements, hydrogen scrambling, or unintended fragmentation, resulting in reduced confidence in peptide identification and structural elucidation. Consequently, collision energies must be carefully optimized to generate sufficient fragment ion information while preserving the isotopically labelled peptide backbone. For this reason, peptide identification is often performed by acquiring spectra at low and high collisional energies on the undeuterated samples.

1.3. Hydrogen-Deuterium Exchange Mass Spectrometry

Hydrogen-deuterium exchange mass spectrometry (HDX-MS) is a structural biology technique that probes protein conformation and dynamics by measuring the exchange of backbone amide hydrogens with deuterium atoms from the surrounding solvent. Performed under near-native solution conditions, HDX-MS is particularly well suited for characterizing conformational heterogeneity, transient intermediate states, intrinsically disordered regions, and protein-ligand interactions. Consequently, it serves as a valuable technique that complements the widely used structural biology techniques such as X-ray crystallography, NMR spectroscopy, and cryo-EM.

The theoretical basis of HDX-MS originates from pioneering studies by Linderstrøm-Lang and colleagues in the 1950s, who recognized that amide hydrogens within proteins continuously exchange with solvent hydrogens.

The rate of exchange depends not only on the chemical properties of the amide group itself but also on the local environment surrounding the residue. Consequently, measurements of hydrogen exchange provide a direct link between protein structure, stability, and dynamics.

1.3.1. Fundamentals of Amide Hydrogen Exchange

HDX-MS fundamentally measures the rate at which amide hydrogens exchange, k_{ex}, with the deuterons in the solution. In a typical HDX-MS experiment, a protein is diluted into a deuterated buffer (such as D_2O), initiating exchange between solvent deuterium atoms and labile hydrogens within the protein. Although hydrogens associated with side chains, N- or C-termini, hydroxyl groups, and thiols may also exchange, these sites undergo rapid back-exchange during quenching and chromatography stages of the experiment (Figure 1.11). Consequently, HDX-MS primarily monitors deuterium incorporation at backbone amide positions, which serve as sensitive reporters of protein structure and dynamics due to their involvement in the hydrogen-bonding networks that stabilize secondary structural elements. Since each incorporated deuteron increases the molecular mass by approximately 1 Da (the masses of deuterium and hydrogen are 2.01 and 1.01 Da, respectively), the resulting mass shift is directly proportional to the extent of deuterium uptake and can be readily measured by mass spectrometry.

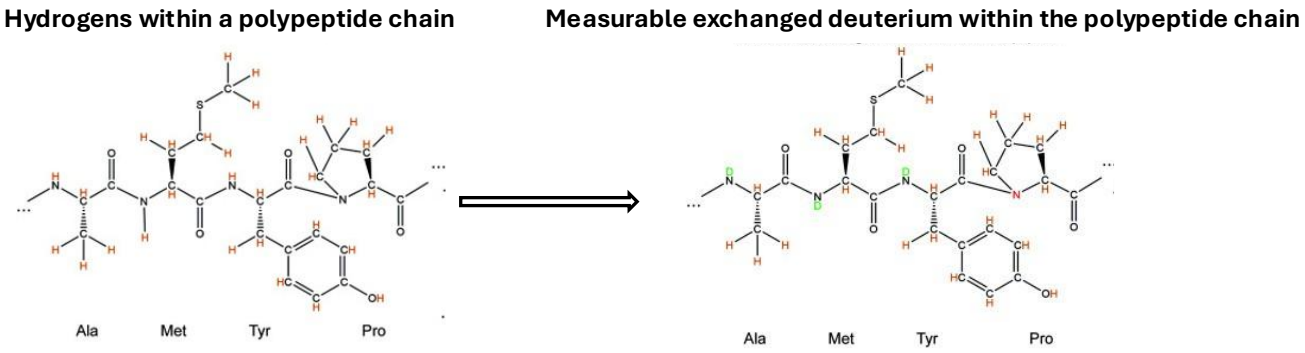


Figure 1.11 | Schematic representation of exchangeable hydrogen atoms within a peptide backbone. Upon exposure to D_2O, labile hydrogens exchange with deuterium from the surrounding solvent. During HDX-MS analysis, most deuterium incorporated into amino acid side chains is lost through back-exchange during quenching and chromatographic separation. In contrast, deuterium incorporated into backbone amide positions is largely retained. Consequently, the observed mass increase primarily reflects deuterium uptake at backbone amide sites. Proline residues do not participate in backbone amide exchange because they lack an amide hydrogen. Adapted from Vinciauskaite *et al.*[15]

The isotopic exchange of a backbone amide hydrogen occurs through acid (H_3O^+)-, base (OH^-)- water (H_2O)-catalyzed reactions. Therefore, the resulting intrinsic exchange rate constant (k_{ex}) can be expressed as a sum of the three terms:

$$k_{ex} = k_H[H^+] + k_{OH}[OH^-] + k_{H2O}[H_2O] \quad (1.10)$$

where k_H, k_{OH} and k_{H2O} are the exchange rate constants associated with acid-, base- and water-catalyzed reactions, respectively.[43] In the base-catalyzed mechanism, a deuterated hydroxide ion removes the amide proton, forming a transient negatively charged amide nitrogen that is subsequently reprotonated with a D^+ ion present in the solvent (Figure 1.12a). Under acidic conditions, exchange may occur through protonation of either the amide nitrogen (Figure 1.12b) or carbonyl oxygen (1.8c), increasing the susceptibility of the amide hydrogen to exchange with the deuterium in the solvent. In both cases, the net result is the replacement of the backbone amide hydrogen with deuterium from the surrounding solvent.

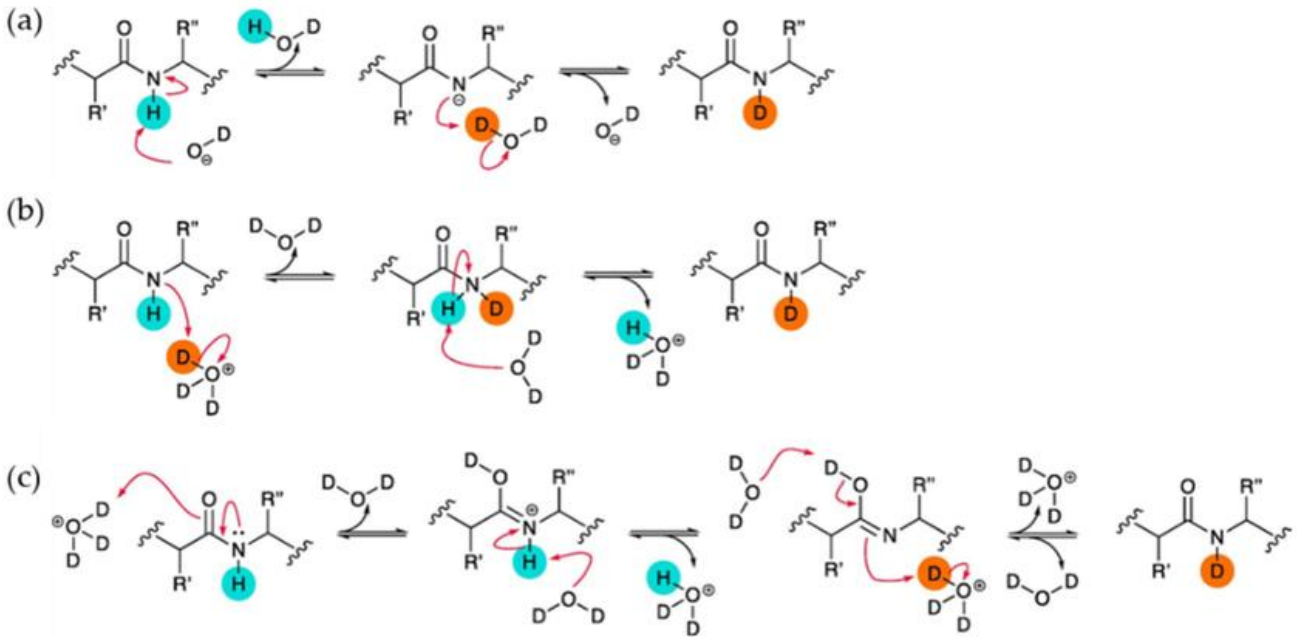


Figure 1.12 | Mechanisms of acid- and base-catalyzed HDX reaction. (a) Under basic conditions, exchange proceeds through the removal of the amide proton followed by incorporation of deuterium from the solvent. (b) Acid-catalyzed exchange can occur through (b) protonation of the amide nitrogen, facilitating replacement of the amide hydrogen with deuterium, or by (c) protonation of the amide carbonyl oxygen, which similarly promotes exchange at the backbone amide position. Adapted from Narang *et al*.[8]

Pioneering work by Englander *et. al.* provided detailed studies on the amide exchange rates in the unstructured poly-DL-alanine model, associating values to rate constants k_H, k_{OH} and k_{H2O} to 41.7, 1.12×10^{10} and 3.16×10^{-2} M^{-1} min^{-1}, respectively, at 20 °C.[44–46] Combining these values and the equation provided above (equation 1.10), the relationship between the exchange rate constant, k_{ex}, as a function of pH generates a V-shaped curve with a pH minimum at ~2.5-3.0 (Figure 1.13). At this pH, the acid and base-catalyzed reactions are equal, whereas exchange at higher pH values is predominantly base-catalyzed. This strong pH dependence reduces exchange rates by approximately four orders of magnitude when the pH is lowered from physiological conditions (~pH 7), where labelling is performed, to pH 2.5, where the exchange reaction is quenched.

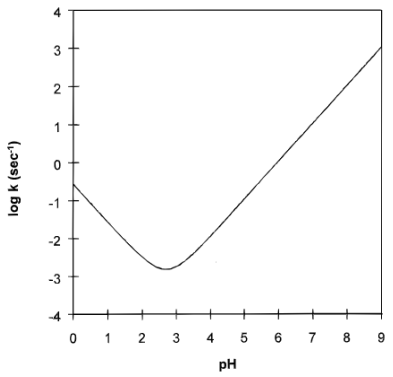


Figure 1.13 | Dependence of the intrinsic amide hydrogen exchange rate constant (k_{ex}) on solution pH for an unstructured peptide. The characteristic V-shaped profile arises from the combined contributions of acid- and base-catalyzed reactions, with a minimum exchange rate occurring near pH 2.5–3.0. The pronounced reduction in exchange rate at low pH forms the basis of HDX-MS quench conditions, which preserve deuterium labelling prior to analysis. Adapted from Englander *et al*.[47]

Similar to pH, temperature directly influences the rate of exchange, k_{ex}, in HDX reactions, with higher temperatures increasing k_{ex} and lower temperatures slowing it. The Arrhenius equation can describe the temperature dependence of amide hydrogen exchange:

$$k_{ex}\,(T) = \; k_{ref(293)} * \exp\left(-\frac{Ea}{R}\left[\frac{1}{T} - \frac{1}{293}\right]\right) \qquad (1.11)$$

where $k_{ref(293)}$ is the reference constant, E_a is the energy of activation for acid-, base- or water-catalyzed reactions, R is the gas constant, and T is the absolute temperature.[45,48] The exponential nature of this relationship means that relatively small temperature changes can have a substantial effect on exchange rates. For example, decreasing the temperature from 25°C to 0°C reduces the intrinsic exchange rate by approximately 14-fold.[45,48] When combined with quenching to pH 2.5, this reduction effectively suppresses both forward and reverse exchange (or back-exchange) reactions, preserving the isotopic labelling acquired during the experiment. Therefore, HDX-MS experiments are routinely performed under low-temperature conditions following quenching, including proteolytic digestion, chromatographic separation, and mass spectrometric analysis.

In addition to pH and temperature, the k_{ex} is also influenced by the local amino acid sequence surrounding a given amide hydrogen. Neighbouring side chains can alter exchange rates through both inductive and steric effects, although these contributions are generally less pronounced than those arising from changes in pH or temperature.[45,48] Polar and charged residues can modify the electron density around adjacent peptide bonds, thereby affecting the acidity of the amide hydrogen and its susceptibility to exchange. For example, amides located adjacent to acidic residues such as aspartate or glutamate typically exchange more rapidly than those surrounded by non-polar residues. Conversely, bulky side chains can hinder solvent access to the amide group and reduce exchange rates through steric effects. Bai and co-workers demonstrated that neighbouring residue effects can alter intrinsic exchange rates by more than an order of magnitude, with certain residue combinations exhibiting exchange rates up to 10–20 times slower than predicted for an average peptide.[45] Therefore, sequence-dependent effects must be considered when calculating intrinsic exchange rates and interpreting HDX-MS data, particularly when comparing regions of proteins that differ substantially in amino acid composition.

1.3.2. HDX in ordered and disordered proteins

Proteins exist along a structural continuum ranging from well-folded globular proteins with defined three-dimensional structures to intrinsically disordered proteins (IDPs) that lack stable tertiary structure. Many proteins also contain both ordered and disordered domains, with intrinsically disordered regions (IDRs) embedded within otherwise structured proteins. Regardless of their degree of structural organization, proteins are inherently dynamic molecules that continuously sample different conformational states through local and global fluctuations. These transient motions, or “breathing motions,” can disrupt intramolecular hydrogen-bonding networks, exposing backbone amide groups to the surrounding solvent and allowing hydrogen-deuterium exchange to occur. Therefore, the rate at which an amide hydrogen exchanges reflects not only its solvent accessibility, but also the conformational dynamics that govern its exposure. In unstructured peptides, this exchange can occur at a millisecond to second timescale.

The relationship between protein dynamics and hydrogen exchange is described by the Linderstrøm-Lang model, in which each backbone amide exists in equilibrium between a protected, "closed" state and a solvent-accessible, "open" state. The observed exchange mechanism can therefore be described as:

$$N - H_{cl} \underset{k_{cl}}{\overset{k_{op}}{\rightleftarrows}} N - H_{op} \xrightarrow{k_{ex}} N - D_{op} \underset{k_{cl}}{\overset{k_{op}}{\rightleftarrows}} k_{op}\, N - DH_{cl} \qquad (1.12)$$

where opening and closing occur with rate constants k_{op} (s^{-1}) and k_{cl} ($M^{-1}s^{-1}$), respectively, and exchange within the open state occurs with rate constant (k_{ex}). This relationship suggests that the proteins in solution remain in equilibrium between the open and closed conformations; hence, the rate of exchange is mainly determined by the protein dynamics or its intrinsic exchange rate (k_{ex}). The observed exchange rate (k_{obs}) of protected amides can therefore be given by:

$$k_{obs} = \frac{k_{op} * k_{ex}}{kcl + k_{op} + k_{ex}} \qquad (1.13)$$

Even though the HDX reaction may occur reversibly in an open state, the experimental design allows for the deuterium concentration to be much greater than that of hydrogen, forcing the forward exchange reaction. Structured or ordered regions of the protein mainly sample the closed or folded conformation, suggesting that $k_{cl} >> k_{op}$. This further reduces equation 1.13 to:

$$k_{obs} = \frac{k_{op} * k_{ex}}{kcl + k_{ex}} \qquad (1.14)$$

Two limiting kinetic regimes arise from the Linderstrøm-Lang model, EX1 and EX2. These regimes are determined by the relative magnitudes of the rate of closing event k_{cl} and the intrinsic chemical exchange rate k_{ex}. In EX1 kinetics, the $k_{ex} >> k_{cl}$, resulting in the rate of exchange becoming almost equal to the rate of the opening event. Under such conditions, for example, those observed in intrinsically disordered proteins (IDPs), the protein spends most of its time sampling the open state, resulting in complete exchange of the backbone amides with the solvent. The observed exchange rate, therefore, can be reduced to:

$$k_{obs} = k_{ex} \qquad [s^{-1}] \qquad (1.15)$$

Rather than a gradual isotopic shift upon HDX reaction, the EX1 regime produces a bimodal isotopic distribution corresponding to populations of exchanged and unexchanged species (Figure 1.14a). Such behaviour is typically associated with large conformational rearrangements or transiently populated intermediate states. However, under native conditions, most stable proteins undergo an EX2 behaviour where they sample the closed state for a far longer period, resulting in $k_{cl} >> k_{ex}$. This presents as a binomial isotopic distribution upon deuteration (Figure 1.14b). Under EX2 kinetics, equation 1.15 can be reduced to:

$$k_{obs} = \frac{k_{op} * k_{ex}}{k\text{cl}} = K_{op} * k_{ex} \qquad [M^{-1}s^{-1}] \qquad (1.16)$$

where the K_{op} is defined by the equilibrium constant of the opening and closing reaction ($\frac{k_{op}}{k\text{cl}}$). An amide hydrogen located within the core of a folded kinase may undergo numerous opening and closing events before a single exchange event occurs. As a result, exchange rates reflect the equilibrium population of open conformations rather than the opening rate itself.

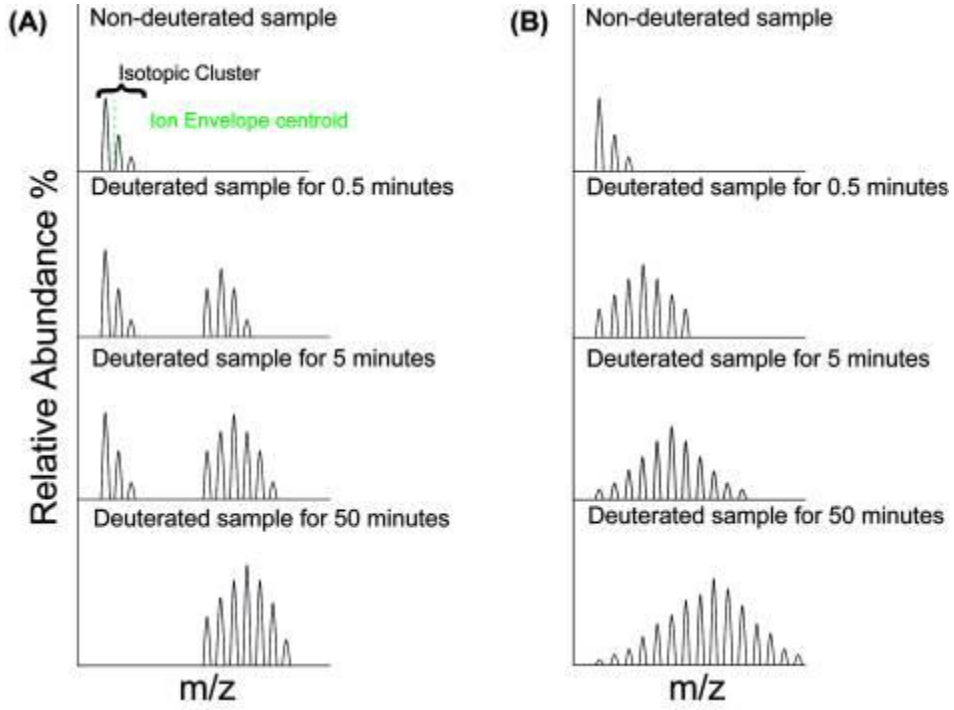


Figure 1.14 | Schematic representing the EX1 and EX2 HDX kinetics. (a) EX1 exchange occurs when exchange is faster than structural refolding, resulting in a bimodal isotopic shift. (b) EX2 exchange occurs when conformational fluctuations are rapid relative to chemical exchange, producing a continuous shift in the isotopic envelope. Adapted from Vinciauskaite *et al*.[15]

Under EX2 conditions, protection factors can also be related to free energy through:

$$\Delta G_{obs} = RT\ ln(PF) \qquad (1.17)$$

where R is the gas constant, and T is the absolute temperature. This relationship provides a direct thermodynamic connection between hydrogen exchange measurements and conformational stability.[45]

One of the most important quantitative parameters obtained from HDX experiments is the protection factor (PF), which describes the extent to which protein structure suppresses hydrogen exchange relative to an unstructured peptide. The PF is defined by the ratio of the intrinsic exchange rate to the observed exchange rate:

$$PF = \frac{k_{ex}}{k_{obs}} \quad (1.18)$$

While k_{ob} reflects the exchange rate observed for an amide within the context of the folded region, k_{ex} is calculated from the primary amino acid sequence and accounts for the influence of neighbouring residues, pH, temperature, and other local chemical effects on exchange.[32,36,37]

The protection factor quantifies the extent to which protein structure suppresses exchange relative to an unstructured peptide. A protection factor of greater than 1 corresponds to a presence of some degree of protection from solvent exchange. The larger the protection factor is, the higher the protection or presence of secondary structure a protein has.[47,51] Therefore, using PFs as a quantitative framework is especially helpful when studying IDPs, as it can provide information on the presence of residual structures.[52]

1.3.3. Bottom-Up Workflow for HDX-MS

HDX-MS experiments can be performed using bottom-up, middle-down, or top-down analytical strategies, all of which rely on the same fundamental principles of hydrogen-deuterium exchange. The primary distinction between these approaches lies in the stage at which structural information is obtained. In bottom-up HDX-MS, proteins are digested into peptides following deuterium labelling and analyzed at the peptide level. In contrast, middle-down and top-down workflows preserve larger protein fragments or intact proteins, respectively, providing higher spatial resolution but often requiring specialized instrumentation and data analysis strategies.[15,53–55] While each approach offers distinct advantages, bottom-up HDX-MS remains the most widely adopted methodology due to its robustness, sensitivity, broad applicability, and compatibility with automated workflows. Consequently, the work presented in this thesis focuses exclusively on the bottom-up HDX-MS workflow described below.

A conventional bottom-up HDX-MS experiment consists of five major stages: (i) deuterium labelling, (ii) quenching of the exchange reaction, (iii) proteolysis, (iv) chromatographic separation coupled to mass spectrometry, and (v) data processing and interpretation (Figure 1.15). Collectively, these steps are designed to preserve the deuterium labelling pattern acquired during the exchange reaction while minimizing unwanted back-exchange prior to data analysis.

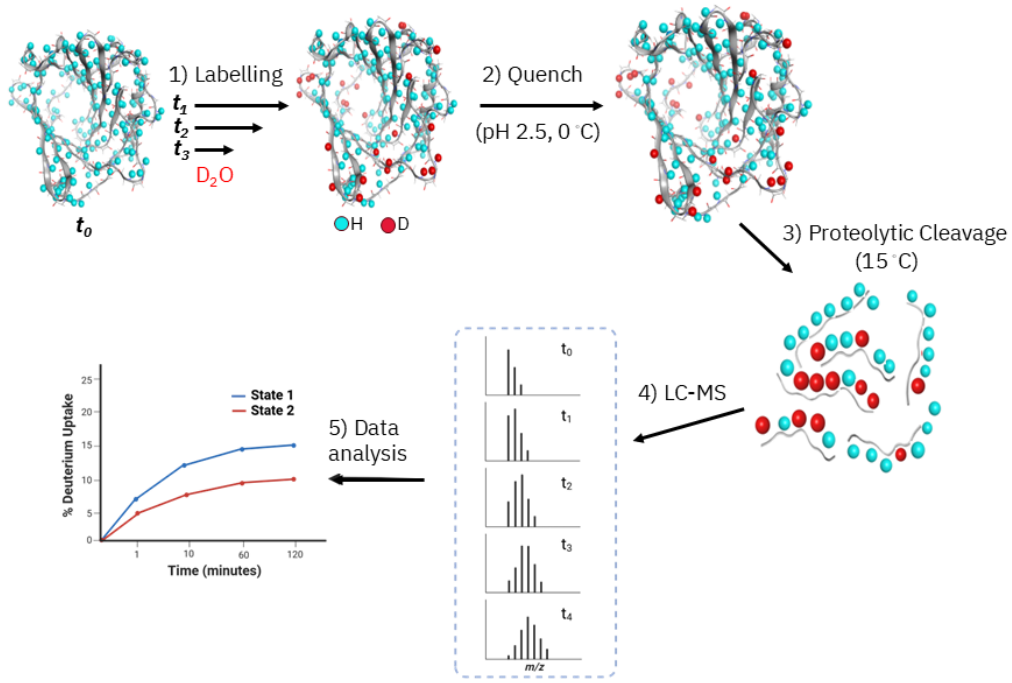


Figure 1.15 | Schematic representation of the bottom-up HDX-MS workflow. Proteins are exposed to deuterated buffer for defined labelling periods before the exchange reaction is quenched by lowering the pH and temperature. The labelled proteins are subsequently digested under quench conditions, and the resulting peptides are separated by reversed-phase LC and analyzed by ESI-MS. Deuterium uptake is quantified from peptide mass shifts and compared across labelling times or protein states to reveal changes in protein conformation, dynamics, and molecular interactions.

The experiment begins by (i) initiating hydrogen-deuterium exchange through dilution of a protein solution prepared in H_2O-containing buffer into an equivalent D_2O-containing buffer. Typical labelling buffers contain 80–95% D_2O and are adjusted to the desired pD and temperature before mixing. Exchange is then allowed to proceed for a series of labelling time points, commonly ranging from seconds to several hours. Multiple labelling timepoints are required because a single measurement provides only a snapshot of deuterium incorporation, whereas a time course allows exchange kinetics to be determined. When comparing more than one state, for instance, when observing the effects of a mutation or post-translational modification on a wild-type protein system, all states are labelled under identical conditions. Differences in deuterium incorporation between the two states can then be attributed to changes in structural stability, solvent accessibility, or conformational dynamics. This comparative approach forms the basis of many HDX-MS applications in structural biology and drug discovery.

Following labelling, the exchange reaction is (ii) quenched to preserve the isotopic labelling pattern. This is achieved by rapidly lowering both the pH and temperature of the sample. Typically, an acidic quench buffer reduces the pH to approximately 2.5 while the sample is simultaneously cooled to 0°C. As discussed previously, the combined effects of low pH and temperature decrease intrinsic exchange rates by several orders of magnitude, effectively "freezing" the deuterium distribution acquired during labelling. Although back-exchange with H^+ in solution is not entirely eliminated under quench conditions, it is sufficiently reduced. The quench buffer can be prepared with denaturants such as guanidine hydrochloride or reducing agents such as Tris (2-

carboxyethyl) phosphine (TCEP), to disrupt higher-order structure, facilitating protein unfolding for efficient proteolytic cleavage.

Next, the acid-quenched protein is (iii) digested under conditions compatible with the low pH and temperature requirements of the HDX reaction. Conventional proteases such as trypsin are inactive under these acidic conditions and therefore unsuitable for HDX workflows. Instead, acid-stable proteases, most commonly pepsin or protease XIII, are employed. These proteases remain highly active near pH 2–3 and efficiently cleave proteins into peptides suitable for LC-MS analysis while maintaining conditions that suppress further back-exchange. The digestion is usually performed online with the temperature for the proteolytic chamber set to 15°C. This ensures the most efficient proteolysis step while also minimizing back-exchange.

Proteases, such as pepsin, usually cleave proteins non-specifically, resulting in multiple overlapping peptides that can significantly benefit from the addition of ion-mobility or chromatographic separation (or both) prior to their detection by MS. In a conventional set-up, the peptides are (iv) trapped and desalted on a reversed-phase trapping column before separation on an analytical reversed-phase column. These columns are packed with a hydrophobic stationary phase (usually C18) that separates the peptides based on hydrophobicity, using a rapid organic gradient to elute them off the column and into the MS. The LC stage utilizes high flow rates of the mobile phases, at 0 °C, to ensure efficient peptide separation while minimizing back-exchange. A schematic depicting the Waters conventional HDX-MS setup used in the Wilson lab is illustrated in Figure 1.16a.

This conventional HDX-MS workflow is highly effective for measuring protein dynamics on timescales ranging from seconds to hours, with typical minimum labelling times of approximately 10 s. However, characterization of weak binding interactions, rapidly interconverting conformations, and transient intermediate states—particularly those associated with highly dynamic IDPs—requires substantially shorter labelling periods. To address this limitation, several millisecond HDX-MS platforms have been developed, including the Time-Resolved Electrospray Ionization HDX-MS (TRESI-HDX-MS) system implemented in the Wilson Lab.[56,57]

TRESI-HDX-MS employs a concentric capillary mixer in which protein and D_2O solutions continuously flow through the inner and outer capillaries, respectively. An automated Continuous Flow Injection (CFI)-TRESI-HDX configuration is shown in Figure 1.16b. In this setup, deuterium labelling times are controlled by adjusting the position of the inner capillary within the outer capillary, enabling labelling periods from approximately 140 ms to 18 s. Labelling times can be varied either continuously using a syringe pump-driven translation mechanism or in discrete increments by manually adjusting the position of the inner capillary relative to the quench tee.[58] CFI-TRESI can further be coupled to online LC separation using either a desalting trap column alone (CFIT mode) or a combination of trap and analytical C18 columns (CFID mode). The applications of both configurations are utilized in Chapters 2 and 3.

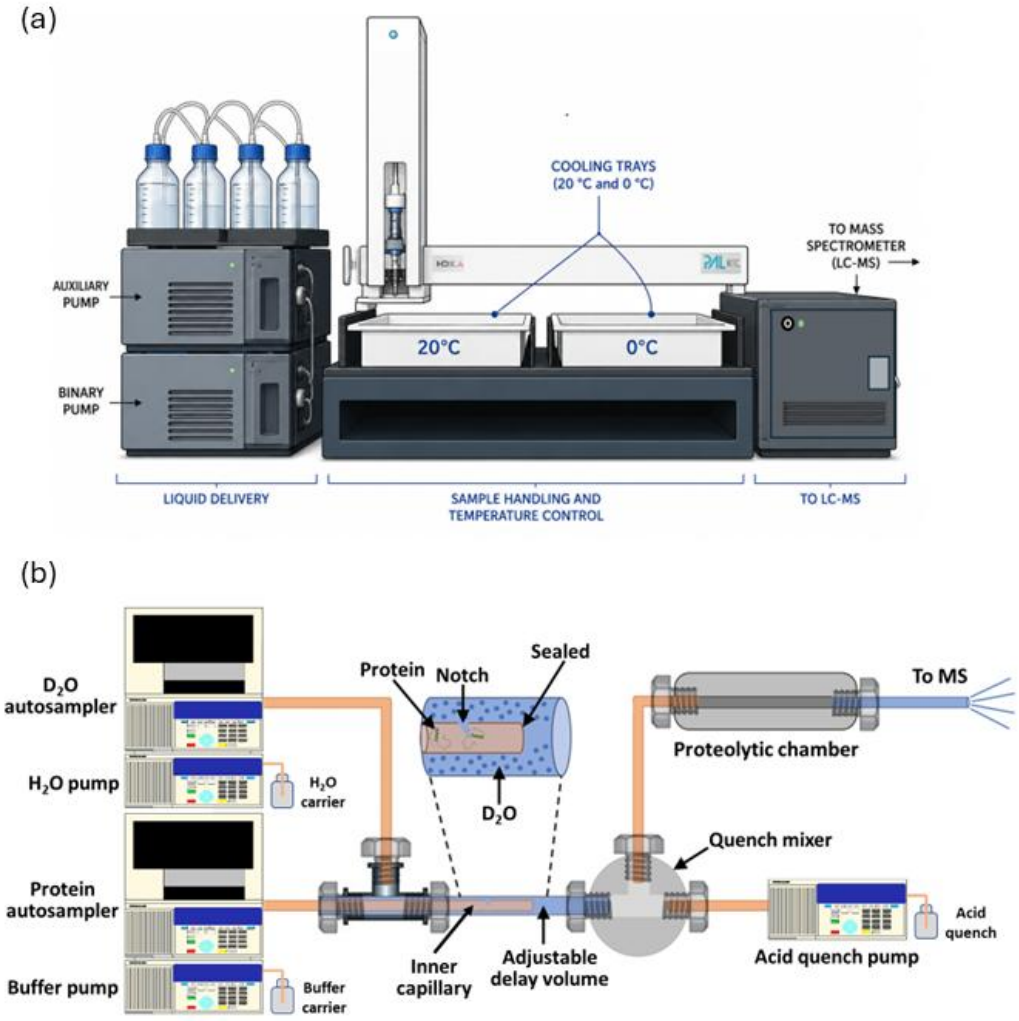


Figure 1.16 | Schematic representations of HDX-MS setups. (a) Conventional HDX-MS liquid delivery and sample handling system coupled to RP-LC, maintained under cool conditions. Samples are stored at 0°C, diluted in D2O at 20°C, and acid-quenched again at 0°C. The quenched sample is digested, and peptides are separated through RP-LC separation before entering the ion source. Liquid delivery of acid and mobile phases is performed using the auxiliary and binary pumps, respectively. (b) Automated Continuous Flow Injection (CFI)- TRESI-HDX-MS platform used for the delivery and rapid mixing of protein and D_2O within a concentric capillary device. The labelling reaction is initiated through mixing at the notched region of the sealed inner capillary and terminated by acid quenching downstream. Following quenching, the sample is subjected to online proteolysis and transferred directly to the mass spectrometer for analysis. Labelling times are controlled by the position of the inner capillary, capillary dimensions, and flow rates. Adapted from Anacleto *et al*.[58]

1.3.4. Data Interpretation for HDX-MS

Peptides eluting from the LC column are introduced into the mass spectrometer by electrospray ionization, where the isotopic envelope of each peptide at various reaction times is measured. Because each incorporated deuterium increases the peptide mass by approximately 1 Da, deuterium uptake can be determined from the

shift in the centroid mass (i.e. the weighted average m/z of the representative peaks in the cluster) of the isotopic distribution relative to the undeuterated control (Figure 1.17a).

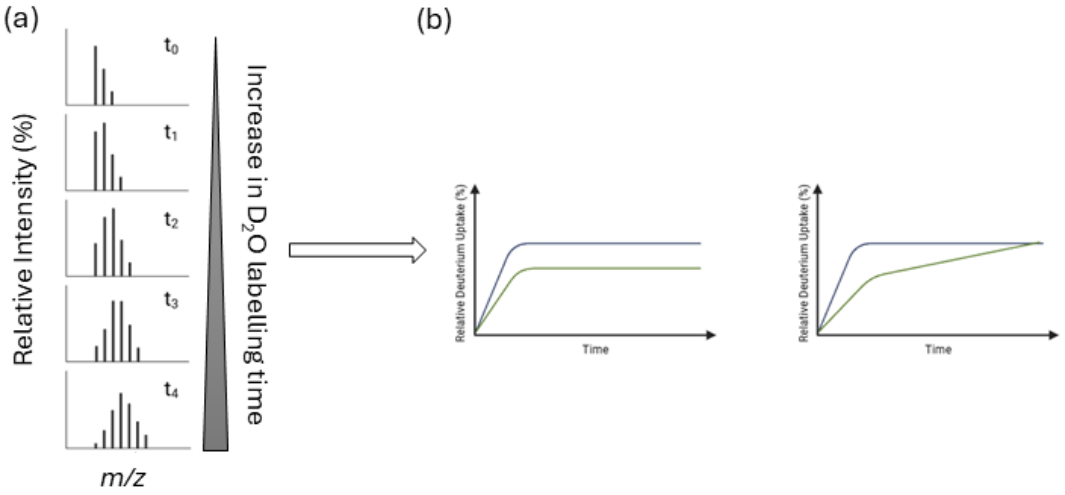


Figure 1.17 | Interpretation of HDX-MS data. (a) An increase in deuterium uptake over time results in a shift of the isotopic envelope toward higher m/z values. The centroid mass, representing the average m/z of the isotopic distribution, is used to quantify the extent of deuterium uptake. (b) Representative HDX uptake plots illustrating changes in deuterium uptake following protein-ligand complexation. Blue and green traces correspond to the apo and ligand-bound states, respectively. Persistent separation between the uptake curves (left) indicates a strong or long-lived interaction that alters protein dynamics, whereas rapid convergence of the curves (right) is characteristic of weaker interactions that produce only transient changes in exchange behaviour.

The deuterium uptake for a given peptide is typically calculated as:

$$\Delta m = m_D - m_H \qquad (1.19)$$

where m_D and m_H represent the centroid masses of the deuterated and undeuterated peptide, respectively. To account for differences in peptide length, uptake is often expressed as a relative fractional deuterium uptake:

$$\%D = \frac{N_D}{N_{max}} \times 100 \qquad (1.20)$$

where N_D is the number of incorporated deuterons and N_{max} is the theoretical maximum number of exchangeable backbone amides. The number of proline residues is deducted from N_{max}, due to its lack of exchangeable backbone amide hydrogen.

Protein-ligand interactions can manifest from ligands exhibiting either low or high binding affinity. A low off-rate, which often, but not always, corresponds to a high-affinity ligand (i.e., one that remains predominantly in the bound state), causes the protein to display a persistently divergent deuterium uptake profile. In contrast, when the ligand has a high off-rate (i.e., rapidly transitions between bound and unbound states), the uptake rates gradually converge over time (Figure 1.17b). If ligand binding does not require substantial conformational rearrangement of the protein, the protein will spend most of its time in the apo or unbound state. As a result, the uptake rates of the bound and unbound forms converge more rapidly, with the maximum difference in the HDX

signal observed at the earliest labelling time points. Therefore, HDX-MS performed at shorter time scales can provide critical insight into weakly bound or rapidly exchanging ligands, information that may otherwise be obscured when only longer, conventional labelling time points are examined.

Regardless of the labelling time selected, a critical consideration for accurate and reproducible HDX data is the characterization of the level of back-exchange (i.e. the level of incorporated deuterium lost during the experiment).[53] This can be performed by using a model peptide (e.g. bradykinin) or a model protein system (e.g. cytochrome c) that has been subjected to deuterium for extended periods of time before analysis, to ensure complete labelling of exchangeable amide hydrogens.[53] The level of back-exchange can then be calculated using the following equation:

$$\text{Back-exchange} = \left[1 - \frac{m_{100\%} - m_{0\%}}{N \times D_{\text{fract}}}\right] \times 100 \qquad (1.21)$$

where $m_{0\%}$ is the centroid mass of the non-deuterated peptide, $m_{100\%}$ is the centroid mass of the maximally deuterated peptide, N is the theoretical number of backbone amides in the peptide and D_{fract} is the fraction of D/H in the labelling buffer used.[48,59,60]

1.4. Quantitative Mass Spectrometry

Mass spectrometry has also become an increasingly important tool in clinical diagnostics owing to its ability to identify and quantify a wide range of biomolecules with high sensitivity and molecular specificity. When coupled with liquid chromatography, LC-MS enables the analysis of complex biological samples such as serum, plasma, urine, and tissue extracts, making it particularly well-suited for biomarker discovery applications. Unlike traditional immunoassays, which are generally limited to a predefined set of targets, LC-MS can simultaneously detect hundreds to thousands of proteins, peptides, lipids, and metabolites within a single analysis (also referred to as multiplexing), providing a more comprehensive view of disease-associated molecular changes.

A biomarker is a measurable biological characteristic that reflects a physiological state, disease process, or response to therapy. Clinically, biomarkers may be used for diagnosis, prognosis, treatment selection, or disease monitoring. The identification of novel biomarkers has become a major focus of clinical proteomics and metabolomics, as disease-associated molecular changes often occur before the onset of clinical symptoms. In some cases, these biomarkers may be present at concentrations below the detection limits of conventional immunoassays, leading to false-negative results. Due to its high sensitivity, specificity, and multiplexing capabilities, LC-MS has emerged as a powerful platform for biomarker discovery and validation.

The development of a clinically useful biomarker typically involves three stages: discovery, verification, and validation. During the discovery phase, untargeted LC-MS workflows are used to identify proteins, peptides, metabolites, or lipids that differ significantly between healthy and diseased populations. Candidate biomarkers identified in these studies are subsequently evaluated in larger sample sets during the verification stage, where targeted analytical methods are employed to confirm the observed changes. The final validation stage focuses on establishing the analytical performance, reproducibility, and clinical utility of the biomarker before implementation into routine diagnostic testing.

Targeted mass spectrometry plays an important role in the latter stages of biomarker development. Among the various targeted approaches, multiple reaction monitoring (MRM) has become one of the most widely adopted strategies for quantitative biomarker analysis. In MRM, a precursor ion is first isolated and fragmented, after which one or more characteristic precursor-to-product ion transitions are monitored. This approach provides a high degree of selectivity and sensitivity by reducing interference from background ions present in complex biological matrices. Consequently, MRM-based assays have become a benchmark for the quantitative measurement of low-abundance biomarkers in clinical samples.

Advances in high-resolution mass spectrometry, improved sample preparation workflows, and increasingly sophisticated data analysis tools have accelerated the translation of biomarker candidates into clinically relevant assays. Nevertheless, many biomarkers identified during discovery studies fail to progress to clinical implementation due to challenges associated with biological variability, limited cohort sizes, and insufficient analytical robustness. As a result, considerable effort has been directed toward developing targeted LC-MS methods capable of providing accurate, precise, and reproducible quantitation across large patient populations.

The work presented in Chapter 4 follows this translational framework through the development of a targeted LC-MS assay for the quantitation of thyroglobulin (Tg), a clinically important biomarker used in the monitoring of differentiated thyroid cancer. By combining the molecular specificity of mass spectrometry with robust quantitative analysis, targeted LC-MS methods offer a promising alternative to conventional immunoassays and continue to expand the role of mass spectrometry in clinical diagnostics.

1.5. Research Objectives

This thesis explores mass spectrometry-based approaches to investigate protein structure, dynamics, and function across multiple biological systems. A major focus of this work was the use of HDX-MS to investigate conformational changes associated with disease-relevant proteins, while also exploring the broader application of liquid chromatography-mass spectrometry (LC-MS) workflows for quantitative proteomics and clinical analysis.

Chapter 2 investigates the structural consequences of disease-associated mutations within the SH2 domain of STAT5B using conventional HDX-MS. This work, performed in collaboration with the Gunning and Raucher Labs at the University of Toronto, refines current mechanistic models of STAT5B regulation.

Chapter 3 applies millisecond HDX-MS to examine the effects of phosphorylation on the intrinsically disordered protein Tau. These studies were designed to capture rapid conformational changes and transient structural features that are inaccessible using conventional HDX-MS timescales.

Building on the quantitative capabilities of mass spectrometry, Chapter 4 focuses on the development and evaluation of an LC-MS/MS workflow to quantify clinically relevant protein biomarkers. Conducted during an internship at the Product and Development Lab at Dynacare, this work aimed to lay the groundwork for quantitative proteomics for clinical diagnostics, highlighting the broader application of mass spectrometry in clinical proteomics.

CHAPTER 2

Hydrogen–deuterium exchange mass spectrometry reveals mutation-specific conformational remodelling in STAT5B SH2 domain

Ayesha Maqsood[1], Qirat F. Ashraf[2,3], Cristina Lento[1], Elvin D. de Araujo[3], Patrick T. Gunning[3] and Derek J. Wilson[1]

[1]*Department of Chemistry, York University, Toronto, M3J 1P3, Canada*

[2]*Centre for Medicinal Chemistry, University of Toronto Mississauga, ON, L5L 1C6, Canada*

[3]*Department of Chemistry, University of Toronto, Toronto, Ontario, M5G 1L7, Canada*

A version of this work has been submitted for publication in the Journal of Biological Chemistry (2026).

A.M. and D.J.W. contributed equally to writing the manuscript. **A.M.** conducted HDX-MS experiments and data analysis. Q.F.A performed protein expression and purification. D.J.W., C.L., E.D.A, and P.T.G. provided supervision.

2.1. Summary

Signal transducer and activator of transcription 5B (STAT5B) is a multidomain transcription factor that regulates cytokine signalling through phosphorylation-dependent dimerization mediated by its Src homology 2 (SH2) domain. Recurrent STAT5B mutations are implicated in hematologic malignancies and immune disorders; however, the structural and dynamic mechanisms by which these mutations alter protein function are poorly understood, as static structural models often reveal minimal differences. Here, we apply hydrogen–deuterium exchange mass spectrometry (HDX-MS) to characterize mutation-dependent structural effects across STAT5B variants. Disease-associated variants (N642H, Y665F, T648S, T628S, S434L, and L327M) were analyzed to map changes in backbone flexibility and regional stability. Collectively, our results establish that STAT5B mutations exert their effects through subtle, region-specific modulation of structural dynamics rather than large-scale conformational rearrangements, with the most impactful effects centred on (but not confined to) the SH2 domain. More broadly, this work reinforces HDX-MS as a means to resolve mutation-specific dynamic signatures in multidomain proteins and provides new mechanistic insights into STAT5B regulation in cancer.

2.2. Introduction

Signal transducer and activator of transcription 5B (STAT5B) is a central mediator of cytokine signalling pathways that regulate immune cell proliferation, differentiation, and survival.[61,62] As a member of the STAT family of transcription factors, STAT5B functions as a latent cytoplasmic protein that becomes activated through phosphorylation-dependent dimerization and subsequent nuclear translocation, enabling transcriptional regulation of target genes.[62–66] Conventional STAT activation is initiated upon cytokine receptor engagement, which triggers Janus kinase (JAK)-mediated phosphorylation of a conserved tyrosine residue, promoting the formation of transcriptionally active parallel dimers capable of DNA binding and gene regulation (Figure 2.1d).[61,67]

In the unphosphorylated state, STAT5B exists in a dynamic equilibrium between monomeric and antiparallel dimer conformations, reflecting the protein's intrinsic flexibility (Figure 2.1a, b).[61,67] This conformational change is essential for its regulatory function, as transitions between inactive and active states depend on coordinated intramolecular and intermolecular interactions.[67] Despite extensive structural characterization of STAT proteins, the molecular determinants governing these transitions remain unclear.[68–70]

Structurally, STAT5B is composed of multiple functional domains, including an N-terminal oligomerization domain, a coiled-coil domain (CCD) involved in protein–protein interactions, a DNA-binding domain (DBD), a linker domain, and an Src homology 2 (SH2) domain, followed by a C-terminal transactivation domain (Figure 2.1a).[67,71] The SH2 domain plays a central role in STAT5B activation by mediating phosphotyrosine-dependent dimerization.[72] This domain contains a conserved binding interface defined by a central antiparallel β-sheet flanked by α-helices, forming two distinct subpockets: the phosphotyrosine (pY) pocket and the pY+3 specificity pocket (Figure 2.1c).[73] Together, these structural elements coordinate phosphotyrosine recognition and stabilize the dimerization interface.

Somatic mutations in STAT5B have emerged as key drivers of hematologic malignancies and immune dysregulation.[74–76] Recurrent gain-of-function mutations—including N642H, Y665F, T648S, and T628S—are frequently localized within the SH2 domain and are associated with enhanced transcriptional activity, prolonged phosphorylation, and constitutive signaling (Figure 2.1e).[69,77] In contrast, mutations outside the SH2 domain,

such as L327M in the coiled-coil domain, have been linked to loss-of-function phenotypes and immune disorders.[78] These observations highlight that mutations across distinct regions of the protein can perturb STAT5B activity through diverse mechanisms. However, despite their clinical relevance, the structural basis by which these mutations alter STAT5B function remains poorly understood.[70]

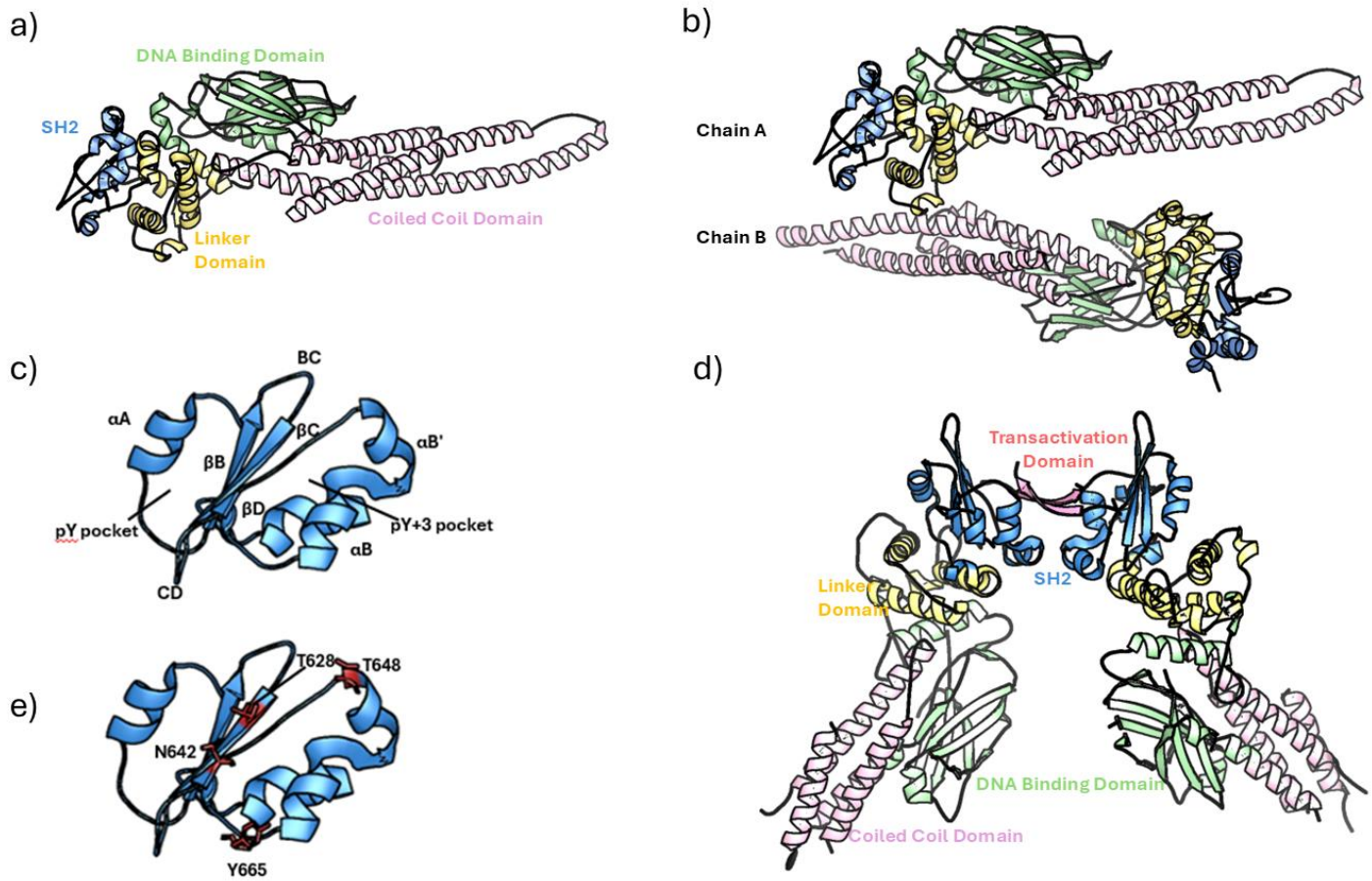


Figure 2.1 | Three-dimensional structural organization of STAT5B wildtype and its SH2 domain. (a) Crystal structure of the STAT5B monomer (Chain B; PDB: 6MBZ) shown in cartoon representation with domains labelled: coiled-coil domain (138–331), DNA-binding domain (332–471), linker domain (498–591), and SH2 domain (592–685).[67] (b) Structure of STAT5B anti-parallel dimer with labelled core fragment domains.[67] (c) Structure of the SH2 domain highlighting the phosphotyrosine (pY) and pY+3 specificity pockets and labelled secondary structural elements. (d) Structure of the STAT6 parallel dimer (PDB: 4Y5U), shown for comparison due to its high sequence homology with STAT5B. [79,80] (e) Structure of the STAT5B SH2 domain, highlighting key mutations in licorice representation.[69,73]

High-resolution structural studies, including crystallography and molecular dynamics simulations, have provided important insights into the organization of the STAT5B domain and its dimerization interfaces.[69,81] However, these approaches predominantly capture static conformations and often reveal minimal structural differences between wild-type and point mutant proteins.[69,73,81] Increasing evidence suggests that STAT5B function is governed by dynamic conformational equilibria and transient intramolecular interactions that are not readily captured by static structural methods. As such, experimental approaches capable of probing protein dynamics in solution are essential for understanding mutation-induced functional changes.

Hydrogen–deuterium exchange mass spectrometry (HDX-MS) has emerged as a powerful technique for characterizing protein conformational dynamics, local stability, and solvent accessibility under near-native conditions. By monitoring backbone amide hydrogen exchange rates, HDX-MS provides molecular-level insight into structural flexibility and transient intramolecular interactions that are often inaccessible by crystallography alone. Previous work from our laboratory combined HDX-MS with molecular dynamics simulations to characterize the oncogenic STAT5BN642H mutation and demonstrated that this variant induces pronounced stabilization of the phosphotyrosine-binding (pY) pocket within the SH2 domain.13 These findings provided the first experimental evidence linking mutation-induced changes in STAT5B conformational dynamics to oncogenic activation and established HDX-MS as a valuable approach for investigating disease-associated STAT5B variants.[67,73]

In this study, we integrate previously characterized findings for the oncogenic N642H variant with new differential HDX-MS analyses of additional disease-associated mutations located within and outside the SH2 domain. By comparing deuterium uptake profiles across wild-type STAT5B and the variants N642H, Y665F, T648S, T628S, S434L, and L327M, we identify mutation-specific changes in regional stability and backbone dynamics that collectively define the structural landscape of STAT5B dysfunction. Our results demonstrate significant stabilization within the SH2 domain, predominantly the pY+3 binding pocket and the adjacent linker region, for STAT5B^{Y665F}. The STAT5B^{T648S} variant revealed stabilization localized to the αB and αB' helices of the pY+3 pocket, while STAT5B^{T628S} showed no significant changes under the observed experimental conditions. Notably, the loss-of-function mutation in STAT5B^{L327M} induced destabilization within the pY+3 pocket despite being located in the coiled-coil domain, indicating allosteric coupling.

Together, these findings provide new mechanistic insight into how disease-associated mutations modulate STAT5B function and identify the SH2 domain as the principal dynamic regulator of STAT5B signalling. While the oncogenic N642H mutation stabilizes the phosphotyrosine-binding (pY) pocket, additional gain-of-function variants primarily perturb the neighbouring pY+3 specificity pocket and associated linker domain, revealing multiple structural pathways through which STAT5B activity can be enhanced. These results establish the pY and pY+3 pockets as dynamically sensitive regulatory hotspots and suggest that therapeutic strategies targeting SH2-domain conformational dynamics may selectively disrupt aberrant STAT5B signalling in disease.

2.3. Experimental procedures

2.3.1. Expression and purification of STAT5B variants

STAT5B (A136-S787) from the gene NCBI: NM_012448.3 was cloned into the pET vector containing an N-terminal His6-SUMO tag and the Ulp1 cleavage site sequence using restriction enzymes NheI and XhoI. To generate STAT5B mutants: N642H, Y665F, T628S, T648S, site-directed mutagenesis was performed (GenScript). Non-SH2 domain mutants: L327M and S434L were generated using the core fragment of STAT5B (A103:Q703). The plasmid vector pFGET19_Ulp1 for His6-Ulp1 was purchased from Addgene (#64697). Protein expression and purification for STAT5B and mutants, and Ulp1, were performed as described.[67,82] STAT5B and mutants were dialyzed and stored in 20 mM HEPES, pH 7.4, 150 mM NaCl and 2% (v/v) glycerol. Protein quantification was determined using

the bicinchoninic acid protein assay (Thermo Fisher Scientific). This work was done by our collaborators from the Gunning Group at the University of Toronto.

2.3.2. Detection using Native Mass Spectrometry

Samples of 10 μM of STAT5B wildtype and mutant proteins were buffer exchanged into 100 mM ammonium acetate, pH 7, using Zeba™ Spin Desalting Columns, 7K MWCO (ThermoFisher Scientific). The protein was ionized using nanoflow electrospray ionization into the Waters Synapt G2-Si (Q-TOF-MS) in positive mode. The spectrum was deconvoluted using ESIPROT.[83]

2.3.3. Continuous flow injection TRESI-HDX (CFI-TRESI-HDX)

CFI-TRESI was performed using the setup previously described, with some modifications.[58] The sample was exchanged into 100 mM ammonium acetate by performing overnight dialysis using a 10 MWCO dialysis cassette. To mimic an activated phosphorylated state, 10 μM of the phosphorylated peptide (QDpTYRLVLDKWL), dissolved in 100% DMSO, was incubated with 5 μM of STAT5B for 1 hour on ice. The protein at 4 μL/min and deuterium oxide (D2O) at 12 μL/min were injected into the reaction chamber using inner and outer capillaries, respectively. The labelling was performed by manually adjusting the reaction chamber to reach three time points (0.98, 1.57 and 1.92 seconds), before being quenched by 3% Formic Acid in 40 mM ammonium acetate (pH 2.5). The acid was set at a flow rate of 64 μL/min. The labelled protein then entered an in-house protease XIII/pepsin column before being sprayed into the Waters Synapt G2 using electrospray ionization. The data was acquired using ion-mobility separation and calibrated using internal standards. Relative deuterium uptake was calculated using Mass Spec Studio (2.0).[84]

2.3.4. Bottom-up Hydrogen-Deuterium Exchange Mass Spectrometry

Native and mutant STAT5B variants (5 μM) were maintained at 4 °C prior to deuterium exchange. For each reaction, 8 μL of protein sample was mixed with 52 μL of D_2O to achieve a final deuterium concentration of 87%. The exchange reaction was conducted over three time points (30 s, 60 s, and 600 s) before quenching with 50 μL of quench buffer (100 mM phosphate buffer, pH 2.5, 0 °C). Quenched samples (50 μL) were immediately injected onto a pepsin column for online digestion, followed by desalting on a VanGuard C18 trap column using 0.1% formic acid in water (mobile phase A) at a flow rate of 200 μL/min for 3 minutes. Peptide separation was performed on a BEH C18 analytical column at 40 μL/min using 0.1% formic acid in acetonitrile (mobile phase B). The eluted peptides were introduced into the Select Series Cyclic Ion Mobility Spectrometry (IMS) system via electrospray ionization. Peptide identification was conducted using ProteinLynx Global Server (PLGS), and relative deuterium incorporation was analyzed with DynamX 3.0. The summed difference in deuterium uptake (%) was calculated for three replicates of STAT5B wildtype and each of the mutant states. Peptides were considered statistically significant when the summed differential HDX uptake exceeded three times the propagated error (3σ). The differences in intrinsic rates of uptake for mutation-containing peptides were accounted for when calculating the difference between peptides containing the F665 residue.

2.4. Results and Discussion

To mimic an active phosphorylated state, the STAT5B wildtype was bound to a synthetic phosphotyrosine (pY) donor peptide. The complexation was confirmed by native mass spectrometry of the intact protein (S1), while its effect on the backbone amide hydrogen network was observed using time-resolved HDX-MS (also referred to as CFI-TRESI-HDX). A significant decrease in deuterium uptake was observed upon complexation, primarily in the B-sheet network and αB helix spanning the dimerization interface, suggesting stabilization of this region (Figure 2.2). Additionally, slight stabilization was also observed in the peptides 465-480 and 332-351 of the linker and the DNA-binding domains, respectively.

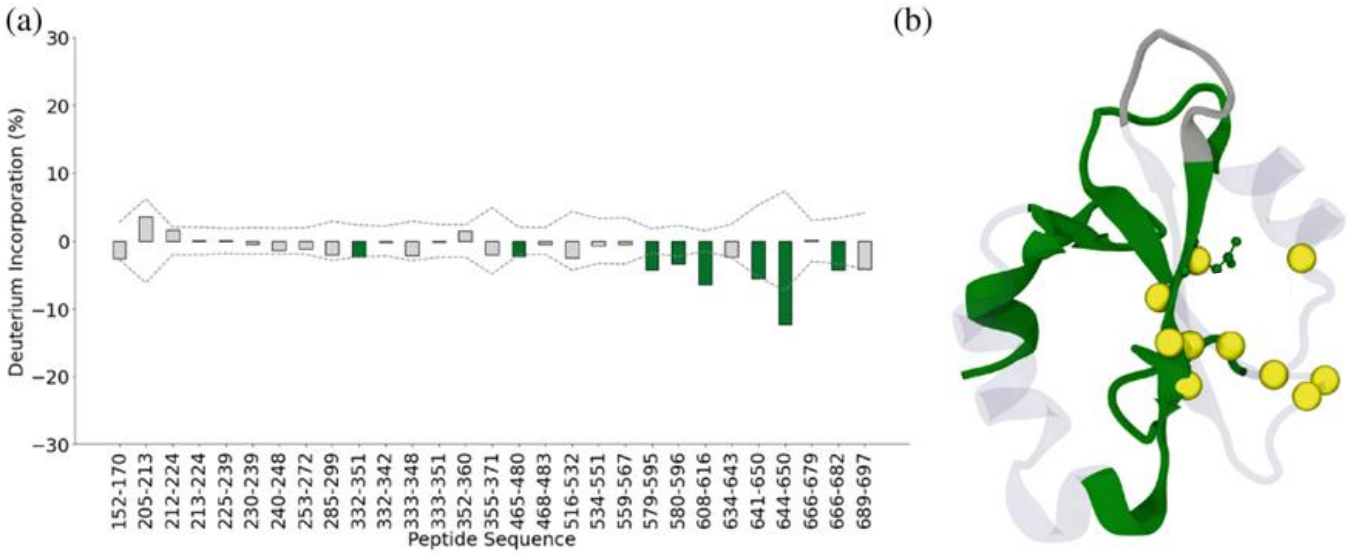


Figure 2.2 | Differential HDX uptakes (%) were calculated between apo and phosphotyrosine peptide-bound STAT5B. (a) Significant decreases in deuterium uptake were observed upon complexation (green), with dashed lines showing uncertainty. (b) Differential uptake was mapped onto the SH2 domain of the STAT5B structure (PDB: 6MBW), highlighting regions of reduced uptake (green). Grey indicates unchanged residues, transparent indicates no peptide coverage. Significance was defined as uptake exceeding the propagated error (3σ) threshold.

2.4.1 SH2 domain mutations produce distinct stabilization effects within the pY+3 pocket.

To characterize the structural consequences of disease-associated mutations within the STAT5B SH2 domain, differential HDX-MS was performed on constructs encompassing the coiled-coil, DNA-binding, linker, and SH2 domains (residues 136–787). Deuterium uptake profiles for wild-type STAT5B were compared with SH2-domain variants N642H, Y665F, T648S, and T628S to assess mutation-dependent changes in backbone flexibility across the dimerization interface.

The N642H mutation, the most frequently observed activating STAT5B mutation in T-cell malignancies, produced the most pronounced reduction in deuterium uptake among the SH2-domain variants examined. Differential HDX-MS analysis revealed strong protection localized to peptides immediately surrounding residue 642 within the phosphotyrosine-binding (pY) pocket, indicating substantial stabilization of secondary and tertiary

structure in the vicinity of the mutation (Figure 2.3). In contrast to the broader protection patterns observed for other activating variants, the effects of N642H were remarkably confined, with no significant changes detected in neighbouring regions of the SH2 domain or in distal structural elements. This highly localized HDX signature suggests that N642H does not induce widespread conformational rearrangement but rather stabilizes a specific structural state of the phosphotyrosine-recognition surface.

Residue N642 occupies a critical position within the pY-binding pocket and contributes to the hydrogen-bonding network responsible for phosphotyrosine recognition during STAT5B activation. Substitution with histidine is proposed to strengthen local interactions within this region, thereby favouring conformations associated with phosphotyrosine engagement. Consistent with this hypothesis, previous biochemical studies have demonstrated prolonged phosphorylation, enhanced transcriptional activity, and increased transforming potential of STAT5B^{N642H} relative to the wild-type protein. The observed reduction in deuterium uptake therefore provides a direct structural explanation for the gain-of-function phenotype by indicating a decreased propensity for local unfolding and an increased stability of the phosphotyrosine-binding interface.

Importantly, the HDX-MS observations were supported by extensive all-atom molecular dynamics simulations, which identified two dominant conformational states for the N642H variant. One of these conformations displayed structural features resembling the active parallel dimer configuration adopted following phosphorylation, suggesting that the mutation shifts the conformational equilibrium toward signalling-competent states. Computational analysis further confirmed that stabilization remained largely restricted to the immediate vicinity of the mutation, in agreement with the experimental HDX-MS data. Together, these findings established N642H as a paradigm for mutation-induced activation of STAT5B through localized stabilization of the pY-binding pocket and provide a useful reference framework for interpreting the structural consequences of additional disease-associated SH2-domain variants.[73]

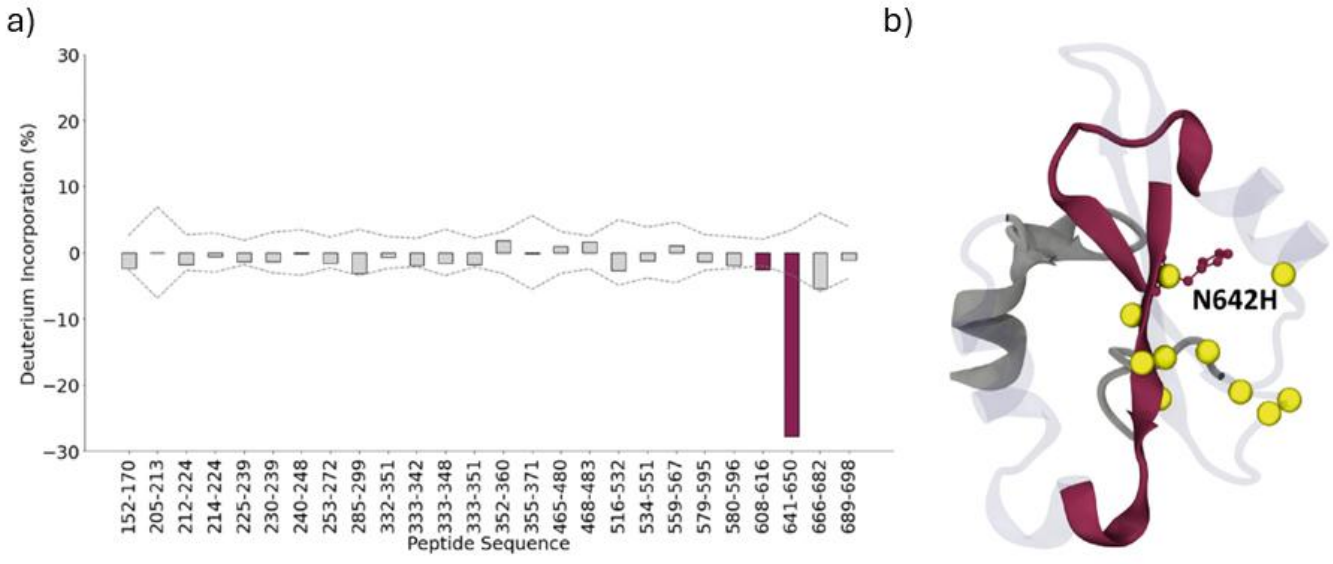


Figure 2.3 | Differential HDX uptakes (%) were calculated between STAT5B wildtype and STAT5B^{N642H}. (a) Significant decreases in deuterium uptake are indicated by plum bars, with dashed lines showing uncertainty. (b) Differential uptake was mapped onto the SH2 domain of the STAT5B^{N642H} structure (PDB: 6MBZ), highlighting

regions of reduced uptake (plum). Grey indicates unchanged residues, transparent indicates no peptide coverage. Significance was defined as uptake exceeding the propagated error (3σ) threshold.

Additional mutations in the SH2 mutations were studied using the conventional HDX-MS set-up as outlined in the experimental section, in order to improve reproducibility and robustness of the experimental setup. The Y665F mutation produced widespread protection across the SH2 domain (Figure 2.4a, b). After correcting for intrinsic exchange differences between tyrosine and phenylalanine residues, the differential uptake profiles revealed maximal protection within peptides spanning the pY+3 pocket. Reduced exchange in this region reflects decreased backbone solvent accessibility and increased local structural stability. Notably, this stabilization extended into the adjacent linker and regions of the DNA-binding domain, suggesting ortho- and allosteric effects of this mutation. These data support a model in which the Y665F substitution increases the hydrophobicity of the pY+3 pocket, thereby enhancing dimer stability and increasing resistance to diphosphatase attack, consistent with previously reported data.[76,85]

In contrast, the T648S mutation, a less aggressive mutation,[67] induced a more spatially restricted decrease in deuterium uptake, primarily localized to residues 651–665 corresponding to the αB and αB' helices (Figure 2.4 c, d). These helices form a key structural component of the pY+3 pocket and directly contribute to the dimerization interface. The localized nature of this protection suggests that T648S perturbs backbone dynamics through subtle changes of local hydrogen bonding or polarity rather than through extensive structural rearrangement. Compared to Y665F, the magnitude of protection is reduced and localized, suggesting increased dimer stability through stabilization of pY+3 residues.

The T628S mutation, located within the phosphotyrosine-binding (pY) pocket, did not produce measurable differences in deuterium uptake relative to wild-type STAT5B under the experimental conditions (Figure 2.4 e, f). The absence of detectable exchange perturbation suggests that this mutation does not significantly alter intrinsic backbone dynamics in the apo state. Given the functional role of the pY pocket in phosphotyrosine recognition, this observation is consistent with a mechanism in which the effects of T628S are dependent on ligand binding or phosphorylation-induced conformational changes rather than intrinsic stability.[69]

Collectively, these results support previous hypotheses and predictive considerations of disease-causing point-mutations occurring within the SH2 domain.[69,86] Mutations within the pY+3 pocket that increase the hydrophobic character or improve aromatic-based interactions of the region have been suspected to be associated with gain-of-function STAT activity through increased rigidity of the pocket. This is consistent with observations of reduced deuterium uptake in pY+3 mutations such as Y665F. In contrast, point mutations in the pY pocket are predominantly associated with altering cognate phospho-peptide binding interactions through perturbed sterics and electronics as opposed to changes within the overall protein fold. As the pY pocket is largely solvent exposed, this is consistent with the lack of changes in deuterium uptake of T628S compared to the wild-type protein.

These structural observations are also consistent with the disease-associated phenotypes of SH2-domain mutations, where variants such as N642H and Y665F, severe oncogenic mutations, and T648S have been identified in hematologic malignancies, including T-cell acute lymphoblastic leukemia and large granular lymphocytic leukemia, and are associated with enhanced STAT5B phosphorylation and constitutive signalling

activity.[76,77] The observed stabilization of the αB and αB' helices within the pY+3 pocket provides a structural basis for these gain-of-function effects by promoting the formation and stabilization of the dimerization interface.

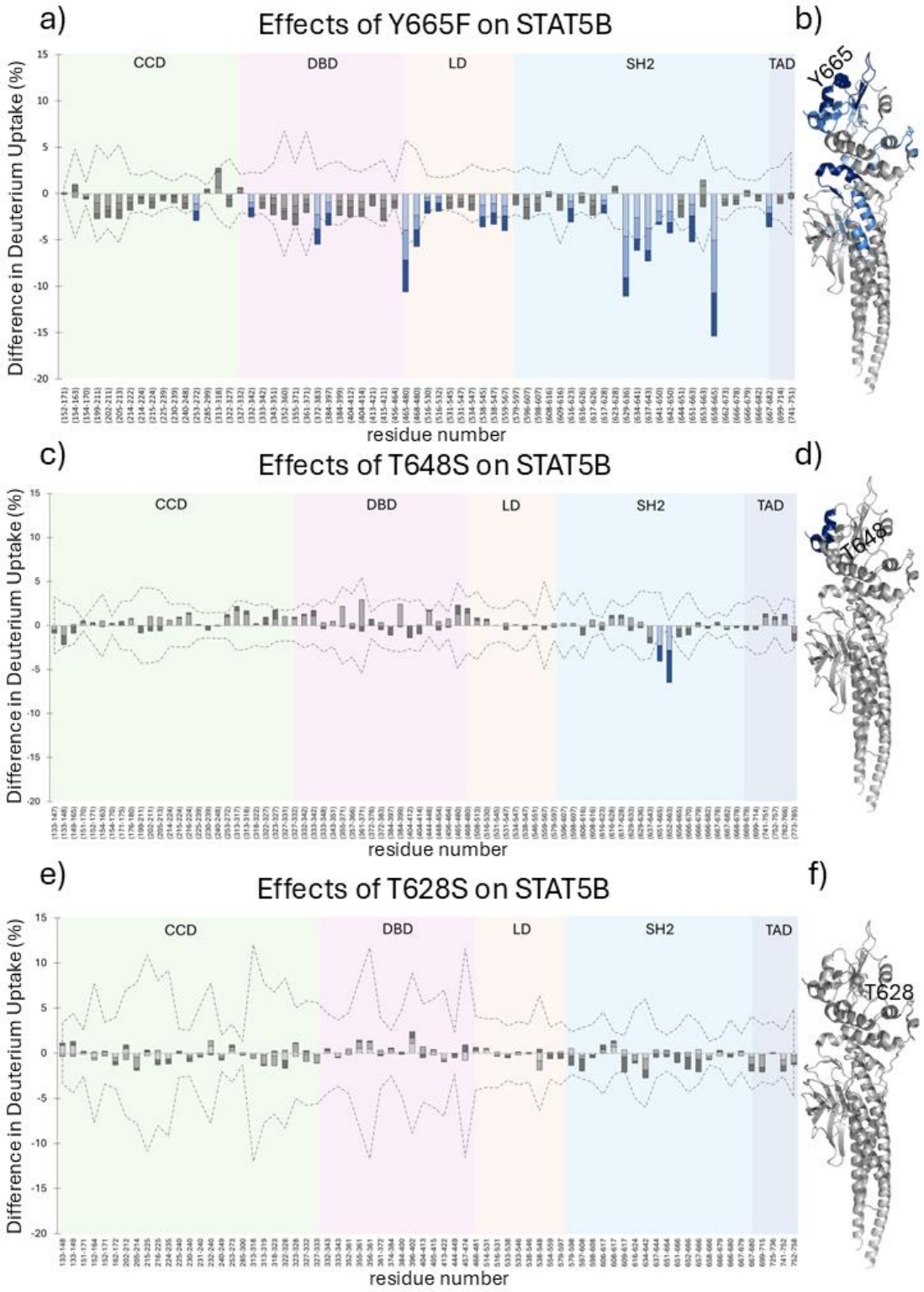


Figure 2.4 | Differential HDX uptakes (%) were calculated between STAT5B wildtype and disease-associated mutations within the SH2 domain. (a) STAT5B^{Y665F} shows the strongest stabilization within the SH2, particularly in the pY+3 specificity pocket and adjacent linker domain. (c) STAT5B^{T648S} shows localized stabilization in the pY+3 pocket proximal to the mutation site. (e) STAT5B^{T628S}, located in the pY pocket, shows no significant changes under the observed experimental conditions. Blue bars denote significant decreases, while the grey bars represent non-significant changes. Significance was defined as uptake exceeding the propagated error (3σ) threshold. (b, d, f) Differential uptake mapped onto the STAT5B structure (PDB: 6MBW). Dark blue indicates the largest decrease in deuterium uptake, mid blue indicates moderate changes, and light blue indicates minor but significant changes.

2.4.2. Non-SH2 domain mutations reveal allosteric effects on the SH2 domain and divergent dynamic outcomes

To assess whether mutations outside the SH2 domain influence STAT5B conformational dynamics, HDX-MS analysis was extended to variants located in the coiled-coil domain (L327M) and the DNA-binding domain (S434L), using matched truncated constructs (residues 136–703) (Figure 2.5).

The S434L mutation, located within a flexible loop of the DNA-binding domain, showed no measurable differences in deuterium uptake across all peptides examined. This may be a consequence of the labelling timescale used for deuterium exchange in conventional HDX experiments, which generally masks the difference in uptake in intrinsically disordered regions of the protein.[87,88] Additionally, no allosteric changes in SH2 dynamics were observed (Figure 2.5c,d).

In contrast, the L327M mutation produced a distinct HDX signature indicative of long-range structural perturbation. Increased deuterium uptake was observed within peptides spanning the αB and αB' helices of the SH2-domain pY+3 pocket, indicating localized destabilization of the dimerization interface. Additional increases in exchange were detected within the linker region and portions of the DNA-binding domain, consistent with a redistribution of conformational flexibility across multiple domains. A minor decrease in deuterium uptake within the αA helix of the pY pocket may suggest compensatory stabilization within adjacent structural regions (Figure 2.5a, b).

The spatial separation between the mutation site in the coiled-coil domain and the observed changes in the SH2 domain indicates the presence of long-range intramolecular coupling. These data provide direct experimental evidence that distal mutations modulate SH2-domain dynamics through long-range allosteric coupling.

Further support for this allosteric network is provided by consistent perturbations observed in peptides spanning R566 within the linker domain for both Y665F and L327M variants. This region has previously been identified as a regulatory element mediating structural coupling between the linker domain and the SH2 domain.[89] Changes in deuterium uptake at this site suggest that both stabilizing and destabilizing mutations can propagate through a shared pathway linking the pY+3 pocket to the linker region.

Collectively, these results demonstrate that mutations outside the SH2 domain can influence STAT5B function by modulating backbone dynamics within the SH2 dimerization interface. The convergence of both SH2 and non-SH2 mutations on the αB and αB' helices of the pY+3 pocket highlight this region as a key element in the structural regulation of STAT5B.

The destabilization of the SH2-domain pY+3 pocket induced by the L327M mutation is consistent with its association with loss-of-function phenotypes and immune dysregulation, where impaired STAT5B signalling has been linked to altered immune cell function.[78,90,91] In contrast, the absence of detectable perturbation for S434L suggests that not all disease-associated variants directly impact intrinsic conformational dynamics, reinforcing the importance of allosteric pathways in mediating mutation-specific functional outcomes.

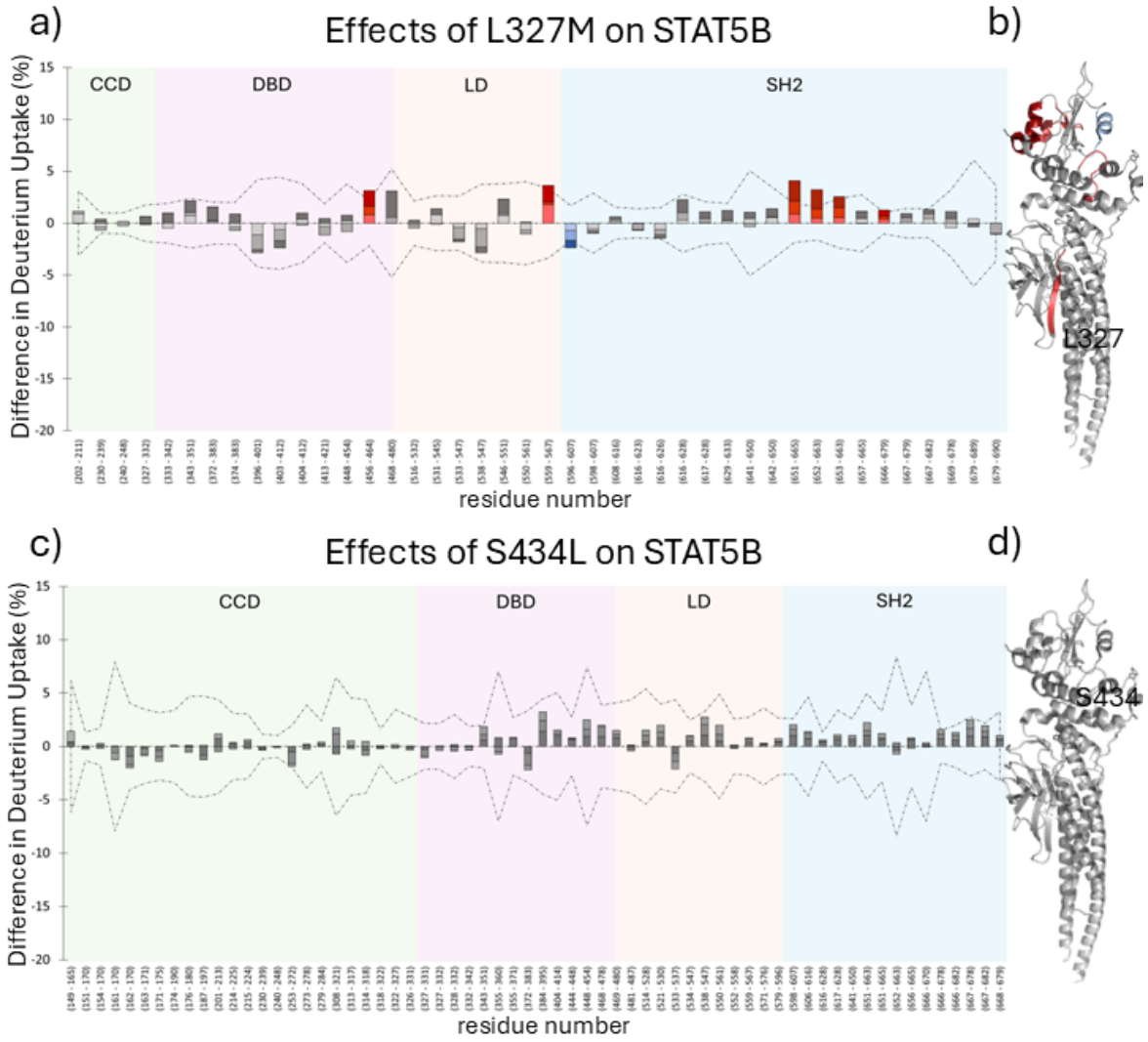


Figure 2.5 | Differential HDX uptakes (%) were calculated between STAT5B wildtype and disease-associated mutations outside the SH2 domain. (a) STAT5B^{L327M} induces significant destabilization within the SH2 domain pY+3 pocket and linker region, consistent with long-range allosteric effects. (b) STAT5B^{S434L} shows no significant changes in deuterium uptake across the protein. Blue bars denote significant decreases, while the grey bars represent non-significant changes. Significance was defined as uptake exceeding the propagated error (3σ) threshold. (c, d) Differential uptake mapped onto the STAT5B structure (PDB: 6MBW), with colour coding as described in Figure 2.4.

2.5. Conclusion

Together, these findings establish a structure–dynamics–function relationship in which STAT5B signalling is dependent on mutation-specific changes that affect the conformational dynamics within the pY+3 pocket and

its associated allosteric network. Gain-of-function mutations stabilize the αB and αB' helices and the adjacent linker region, thereby favouring the formation of the dimerization interface. In contrast, destabilizing mutations shift the conformational equilibrium toward less competent signalling states. Rather than acting through discrete structural rearrangements, these variants appear to modulate the energetic landscape governing the SH2 domain dynamics.

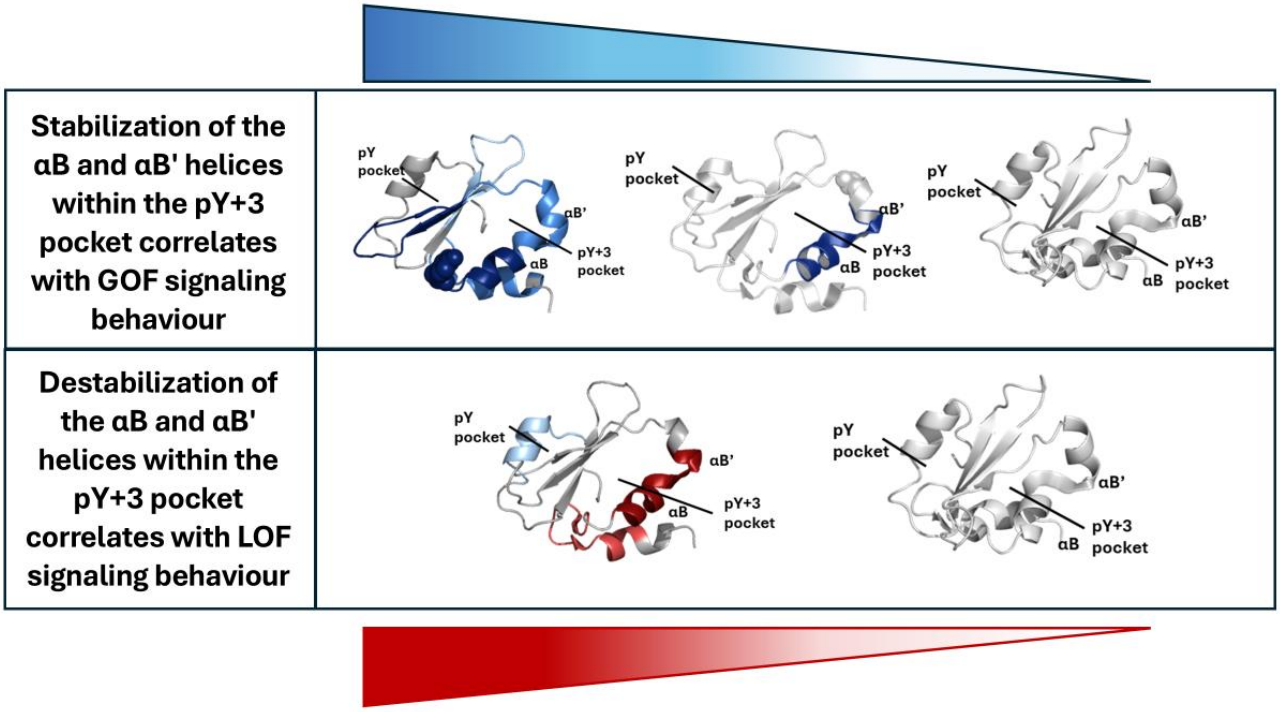


Figure 2.6 | Proposed model illustrating how disease-associated STAT5B mutations alter protein function through mutation-specific changes in conformational dynamics centred on the SH2 domain pY+3 binding pocket. Stabilization of the αB and αB' helices correlates with gain-of-function phenotypes, while increased dynamics within these regions are associated with impaired signaling activity. Together, these observations implicate SH2 domain dynamics as a key determinant of STAT5B function.

More broadly, this work highlights the importance of protein dynamics in STAT5B regulation and demonstrates the unique utility of HDX-MS for resolving mutation-specific conformational effects that remain inaccessible to static structural approaches alone.[67–69,82] By directly linking localized changes in backbone flexibility to functional phenotypes, HDX-MS provides mechanistic insight into how single-residue substitutions reshape STAT5B signalling through a shared dynamic framework and correlating this information with clinical outcomes of patients identified to harbour these mutations. These findings complement existing structural and computational studies while identifying conformationally sensitive regions that may be therapeutically exploitable.[67,68,82] Furthermore, these structural studies provide a basis for leveraging biochemical and structural studies to predict the clinical impact of newly identified disease-causing mutations within the STAT proteins of patient samples.

From a therapeutic perspective, the identification of the pY+3 pocket as a dynamically regulated hotspot has important implications for the development of STAT5B-targeted inhibitors. Although the SH2 domain has long

been recognized as a pharmacological target, direct inhibition of phosphotyrosine recognition has proven challenging because of the shallow and highly conserved nature of the pY-binding surface.[67,69] In contrast, the present findings indicate that modulation of conformational stability within the αB and αB' helices of the pY+3 pocket and the linker domain may provide an alternative strategy for selectively perturbing aberrant STAT5B signaling. Targeting dynamic stability rather than the phosphotyrosine residue binding may therefore represent a more effective approach for disrupting pathogenic STAT5B activation in hematologic malignancies.

In conclusion, this study demonstrates that disease-associated STAT5B mutations alter protein function through mutation-specific remodelling of conformational dynamics centred on the SH2 domain pY+3 pocket. Stabilization of the αB and αB' helices correlates with gain-of-function signaling behaviour, whereas destabilization of the same structural elements is associated with reduced activity. The additional involvement of the linker domain further supports the existence of an extended allosteric network coordinating STAT5B activation. Together, these findings refine current mechanistic models of STAT5B regulation and establish HDX-MS as a powerful approach for defining the dynamic basis of STAT5B dysfunction in disease.

CHAPTER 3

Millisecond Hydrogen–Deuterium Exchange Mass Spectrometry Reveals Kinase-Specific Conformational Biases within the Tau Ensemble

Joseph Anacleto[1], Cristina Lento[1], Vladimir Sarpe[2], Ayesha Maqsood[1], Banafsheh Mehrazma[1], David Schriemer[2], Derek J. Wilson[1]

[1]*Department of Chemistry, York University, Toronto, Ontario, M3J 1P3, Canada*.

[2]*Department of Biochemistry and Molecular Biology, Calgary, Alberta, T2N 4N1, Canada*.

A portion of this chapter has been published in *Anal. Chem*. 2023, 95, 9, 4421–4428.
https://doi.org/10.1021/acs.analchem.2c05003.
Published February 22, 2023
Copyright © 2023 The Authors. Published by the American Chemical Society.

A.M. performed protein purification, HDX-MS experiments, and data analysis under the supervision of D.J.W.

3.1. Summary

Tau is a microtubule-associated protein found in neuronal cells whose primary function is the stabilization of microtubules. However, modifications to tau resulting in the formation of insoluble amyloid aggregates known as neurofibrillary tangles (NFTs) have been found in patients suffering from neurodegenerative diseases, including Alzheimer's Disease (AD). Hyperphosphorylation is one of the most prevalent modifications associated with the formation of these pathological inclusions. Increased activity of a combination of kinases has been associated with tau hyperphosphorylation in AD patients. Out of these, GSK3β, a proline-directed kinase, has been extensively studied in its effects on tau hyperphosphorylation. However, there is still a lack of understanding of the conformational biases induced by a combination of different classes of kinases. Furthermore, due to the intrinsically disordered nature of the protein, structural studies have also been vastly limited. Preliminary hydrogen-deuterium exchange mass spectrometry (HDX-MS) studies on GSK3β-phosphorylated tau demonstrated a general increase in deuterium uptake, particularly at the N- and C-termini as well as the hexapeptide regions. The goal of this work is to employ HDX-MS at a millisecond timescale to provide a comparison of structural biases in the tertiary structure of full-length tau protein when phosphorylated by different classes of kinases, including serine/threonine or tyrosine kinases.

3.2. Introduction

Tau is a neuronal microtubule-associated protein that plays a critical role in maintaining microtubule stability, regulating axonal transport, and supporting neuronal architecture.[92] In the healthy brain, tau exists as a highly soluble intrinsically disordered protein (IDP) that lacks persistent tertiary structure and instead populates a heterogeneous ensemble of rapidly interconverting conformations.[93] Although tau does not adopt a single well-defined fold, transient intramolecular interactions contribute to residual structural organization that is thought to regulate its interaction with microtubules and other cellular binding partners. The dynamic nature of tau is therefore fundamental to its physiological function but also contributes to its susceptibility to pathological misfolding.[94,95]

Abnormal phosphorylation of tau is one of the defining molecular hallmarks of Alzheimer's disease (AD) and related tauopathies. Hyperphosphorylated tau is a critical post-translational modification associated with the formation of neurofibrillary tangles (NFTs), intracellular aggregates whose accumulation correlates strongly with disease progression and cognitive decline.[92,93] More than eighty phosphorylation sites have been identified throughout the tau sequence, and many are targeted by multiple kinases involved in neuronal signalling pathways. While extensive evidence links tau phosphorylation to neurodegeneration, the molecular mechanisms by which specific phosphorylation events contribute to disease remain poorly understood.[52]

Historically, tau hyperphosphorylation has often been associated with a similar shift in the conformational landscape, regardless of the extent of such modification. However, emerging evidence suggests that the biological consequences of phosphorylation depend not only on the extent of modification but also on the specific kinase involved and the residues targeted. Different kinases modify distinct regions of tau and participate in diverse cellular pathways associated with neurodegeneration.[94–98] Consequently, phosphorylation by individual kinases may generate structurally and functionally distinct phospho-tau species with unique pathological outcomes. Understanding how individual kinases influence the tau conformational landscape is

therefore essential for elucidating the molecular mechanisms driving disease progression and for identifying kinase-specific therapeutic strategies.

Protein kinases (PKs) have emerged as some of the most extensively investigated therapeutic targets in neurodegenerative disease, particularly in Alzheimer's disease, where dysregulated phosphorylation contributes directly to tau pathology. [99] Among these, glycogen synthase kinase 3β (GSK3β) is one of the best-characterized tau kinases and has been implicated in both tau hyperphosphorylation and NFT formation. Aberrant activation of GSK3β during aging and disease promotes phosphorylation at numerous disease-associated sites and has been linked to microtubule destabilization, synaptic dysfunction, and enhanced tau aggregation. Previous studies from the Wilson lab demonstrated that GSK3β-mediated hyperphosphorylation induces significant conformational changes within tau, including increased solvent accessibility and structural remodelling of regions associated with aggregation propensity.[52] These findings established a structural framework linking hyperphosphorylation to pathological tau behaviour and provided an important foundation for investigating less-characterized tau kinases.

In addition to GSK3β, growing evidence implicates microtubule affinity-regulating kinase 4 (MARK4) and the Src-family tyrosine kinase Fyn as important contributors to tau-mediated neurodegeneration. MARK4 phosphorylates tau within the microtubule-binding region, particularly at Ser262 and Ser356, residues that play critical roles in regulating tau–microtubule interactions. Phosphorylation at these sites reduces microtubule binding affinity and has been associated with increased tau toxicity and aggregation. Elevated MARK4 activity has been reported in Alzheimer's disease, and inhibition of MARK-family kinases has emerged as a potential therapeutic strategy for limiting tau pathology.

On the other hand, Fyn kinase contributes to disease progression through a distinct mechanism. In addition to phosphorylating tau directly at the Tyr18 residue, Fyn participates in signalling pathways associated with synaptic dysfunction and Aβ toxicity. Interactions between tau and Fyn facilitate aberrant signalling at the postsynaptic density and have been implicated in neuronal toxicity during early stages of Alzheimer's disease. Tyrosine-phosphorylated tau has been identified in paired helical filaments (PHFs) and neurofibrillary tangles (NFTs) isolated from AD brains, suggesting that Fyn-mediated phosphorylation may influence tau pathology through mechanisms that extend beyond aggregation alone. Despite the growing therapeutic interest in both MARK4 and Fyn, comparatively little is known regarding the structural consequences of phosphorylation by these kinases and how they alter the dynamic conformational ensemble of tau.

Characterizing phosphorylation-induced structural changes in tau remains challenging because of its intrinsically disordered nature. Conventional structural biology techniques, including X-ray crystallography and cryo-electron microscopy, are limited in their ability to investigate the highly dynamic conformations populated by soluble tau prior to aggregation. Although NMR has provided valuable insights into local structural preferences, the conformational heterogeneity and rapid exchange kinetics of tau continue to present significant experimental challenges.

Hydrogen–deuterium exchange mass spectrometry (HDX-MS) offers a powerful alternative for studying intrinsically disordered proteins (IDPs) because it directly probes backbone dynamics, solvent accessibility, and conformational changes under near-native conditions. In particular, time-resolved electrospray ionization HDX-

MS (TRESI-HDX) enables measurements on the millisecond timescale, making it uniquely suited for investigating rapidly exchanging structural features within disordered proteins. To facilitate these studies, an automated Continuous Flow Injection-TRESI-HDX (CFI-TRESI-HDX) with a chromatographic separation platform was implemented and optimized to improve experimental robustness, reproducibility, and analytical sensitivity. The automated workflow increased peptide coverage, reduced experimental variability, and enhanced characterization of highly dynamic regions of tau, thereby providing a more comprehensive view of phosphorylation-induced conformational changes.

The objective of this study was to determine how phosphorylation by GSK3β, MARK4, and Fyn alters the conformational ensemble of full-length human tau. GSK3β-phosphorylated tau was initially examined as a positive control to validate the automated CFI-TRESI-HDX workflow against previously established findings. The optimized platform was subsequently applied to investigate the structural consequences of MARK4- and Fyn-mediated phosphorylation. By integrating phosphoproteomics, millisecond HDX-MS, and circular dichroism spectroscopy, this work sought to determine whether different kinases generate distinct phospho-tau conformational ensembles and to establish how kinase-specific structural remodelling may contribute to the molecular mechanisms underlying Alzheimer's disease progression.

3.3. Experimental Methods

3.3.1. Expression and purification of Tau

Recombinant full-length human tau (htau40) was expressed and purified as previously described with minor modifications.[100] Briefly, *Escherichia coli (E. coli)* BL21 cells were transformed with a pET-29b expression vector encoding full-length htau40. Transformed cells were cultured at 37 °C until an optical density at 600 nm (OD_{600}) of 0.5–0.6 was reached, after which protein expression was induced with isopropyl β-D-thiogalactopyranoside (IPTG) for 3.5 h. Cells were harvested by centrifugation at 6,000 × *g* for 20 min and resuspended in lysis buffer. The resulting lysate was heat-treated at 100°C for 20 min to denature endogenous bacterial proteins while preserving heat-stable tau protein. Precipitated proteins were subsequently removed by centrifugation, and the soluble fraction containing tau was dialyzed overnight against cation-exchange buffer. Tau purification was performed using cation-exchange chromatography on an SP Sepharose Fast Flow column. Purified fractions were pooled and assessed for purity by SDS-PAGE, while protein identity and molecular mass were confirmed by native mass spectrometry.

3.3.2. Expression and purification of GSK3β

Recombinant GSK3β was expressed and purified as previously described with minor modifications.[101] *E. coli* BL21 cells transformed with the GSK3β-pGEX expression plasmid (provided by Dr. Jim Woodgett) were cultured at 37 °C until the optical density at 600 nm reached approximately 0.5. Protein expression was induced by the addition of isopropyl β-D-thiogalactopyranoside (IPTG), and cultures were incubated for a further at 37 °C for 4 h. Following induction, cells were harvested by centrifugation and resuspended in wash buffer containing 30 mM Tris-HCl, 100 mM NaCl, 0.1 mM EGTA, 0.1 mM EDTA, and 0.25 mM DTT (pH 7.3). Lysates were prepared by sonication on ice for a total of 8 min using alternating cycles of 15 s sonication and 30 s cooling. Lysates were further pelleted by centrifugation at 40,000 × *g* for 1 h at 4 °C. The supernatant was then loaded onto a GST

affinity gravity-flow column, and the bound protein was eluted using wash buffer with 10 mM reduced glutathione. Eluted fractions containing GSK3β were concentrated and buffer-exchanged into wash buffer using 10 kDa MWCO Vivaspin tubes. Purified protein was aliquoted in the presence of 20% (v/v) glycerol and stored at −80 °C until further use.

3.3.2. Phosphorylation of tau using GSK3β, MARK4, and Fyn kinases.

MARK4 and Fyn kinases were purchased from Abcam (MARK 4: # ab105211, Fyn: #ab84696). 100 µM of Tau was incubated with 2.5-5 µM GSK3β, MARK4 or Fyn kinases at 37°C for 30 hours in phosphorylation buffer containing 50 mM Tris-HCl, 10 mM MgCl2, 5 mM DTT and 3 mM ATP (pH 7.5). The reaction was stopped by heating the reaction mixture at 100°C for 2 minutes to denature the enzyme. It was then centrifuged, and the supernatant containing a heterogeneous mixture of phosphorylated tau was confirmed using SDS-PAGE gel electrophoresis. Where no mobility shift was observed, hyperphosphorylated proteins were subjected to tryptic digestion, followed by phosphopeptide enrichment using Fe^{3+}-$IMAC^{+}$ affinity chromatography.[102] The phosphorylation sites were detected using MS/MS.

3.3.3. Identification of tau using Native Mass Spectrometry

Aliquots of concentrated native tau were buffer exchanged with a 10 kDa MWCO dialysis cassette in 100 mM ammonium acetate (pH 7) for 16-18 hours. The native structure of 10 µM purified tau protein was acquired using nanoflow electrospray ionization in Waters Synapt G2-Si (Q-TOF-MS) under positive ion mode. The spectrum was deconvoluted using ESIPROT.[83]

3.3.4. Continuous flow injection TRESI-HDX (CFI-TRESI-HDX)

CFI-TRESI was performed using the setup previously described.[58] The sample was exchanged into 100 mM ammonium acetate by performing overnight dialysis using a 10 MWCO dialysis cassette. The protein at 4 µL/min and deuterium oxide (D_2O) at 12 µL/min were injected into the reaction chamber using inner and outer capillaries, respectively. The labelling was performed by manually adjusting the reaction chamber to reach three time points (0.98, 1.57 and 1.92 seconds), before being quenched by 3% Formic Acid in 40 mM ammonium acetate (pH 2.5). The acid was set at a flow rate of 64 µL/min. The labelled protein then entered an in-house protease XIII/pepsin column before being sprayed into the Waters Synapt G2 using an electrospray ionization. The data was acquired using ion-mobility separation and calibrated using internal standards. Relative deuterium uptake was calculated using Mass Spec Studio 2.0.[84]

3.3.5. CFI-TRESI-HDX with trap column (CFIT-TRESI-HDX)

The experiment was carried out as described in section 3.3.4. with some modifications. The acid-quenched and digested peptides were loaded onto in-house protease XIII/pepsin column held at 15 °C. The peptides were eluted onto a C18 VanGuard desalting column using 0.1% formic acid in water at 100µL/min for 2 min and eluted using 0.1% formic acid in acetonitrile. Peptide identification was conducted using Protein Lynx Global Server (PLGS), and relative deuterium incorporation was analyzed with DynamX 3.0. The summed difference in deuterium uptake (%) was calculated for three replicates of native and phosphorylated states. Peptides were

considered statistically significant when the summed differential HDX uptake exceeded two times the propagated error (2σ).

3.3.6. CFI-TRESI-HDX with complete LC separation (CFID-TRESI-HDX)

The experiment was conducted as described in section 3.3.5. with additional reversed-phase separation using BEN C18 column at 40 µL/min and eluted using Mobile phase B (0.1% formic acid in acetonitrile). The eluted peptides were similarly sprayed into the Waters Synapt G2 using electrospray ionization, and peptide identification and relative deuterium uptake calculations were performed using PLGS and DynamX 3.0, respectively.

3.3.7. Circular Dichroism (CD) spectroscopy of tau

Circular dichroism (CD) spectroscopy was performed as previously described with minor modifications.[103] Briefly, CD spectra were acquired using a Jasco J-815 spectropolarimeter (JASCO, Tokyo, Japan) at 25 °C under a constant nitrogen atmosphere. Measurements were collected between 185 and 500 nm using a 0.2 mm quartz cuvette. Unmodified and phosphorylated tau samples were buffer exchanged into 100 mM ammonium acetate using a 10 kDa MWCO dialysis cassette. Each reported spectrum represents the average of three consecutive scans.

3.4. Results and Discussion

3.4.1 Optimization and implementation of an automated CFIT-TRESI-HDX for tau analysis

An important part of the work was to optimize and implement an automated Continuous Flow Injection-Time Resolved Electrospray Ionization (CFI-TRESI) technique with an LC separation workflow for the analysis of intrinsically disordered proteins (IDPs). Compared to the conventional HDX-MS methods, millisecond HDX approaches, at millisecond to second timescales, are particularly well suited for studying proteins such as tau, whose highly dynamic conformational ensembles undergo rapid deuterium exchange and are often challenging to characterize using traditional labelling timescales.

The automated platform was developed by the Wilson lab to improve the reproducibility, robustness, and throughput of previous manually operated TRESI-HDX workflows. This setup also allowed the incorporation of CFI-TRESI with full liquid chromatography, referred to as CFID-TRESI mode, or CFI-TRESI with a short C18 column, referred to as the CFIT-TRESI mode. The addition of orthogonal separation allowed increased sensitivity and the ability to use a wide range of buffers in such experiments. The CFID-TRESI workflow showed increased peptide coverage from 47% (Figure S3.6) to over 78% with 2.50 redundancy (Figure 3.1). This was a significant improvement for the proteolysis stage of the bottom-up HDX-MS workflow, given that tau is a challenging target for pepsin and protease XIII due to its high positive charges. This data was acquired over 12 labelling time points (ranging from 150 ms to 4 h), which allowed us to obtain the time points where maximum exchange occurred, i.e. between 0.9 s and 1.9 s on average. This data was also used in future experiments in which modifications were made to the setup to reduce back-exchange (Figure S3.5) and increase throughput.

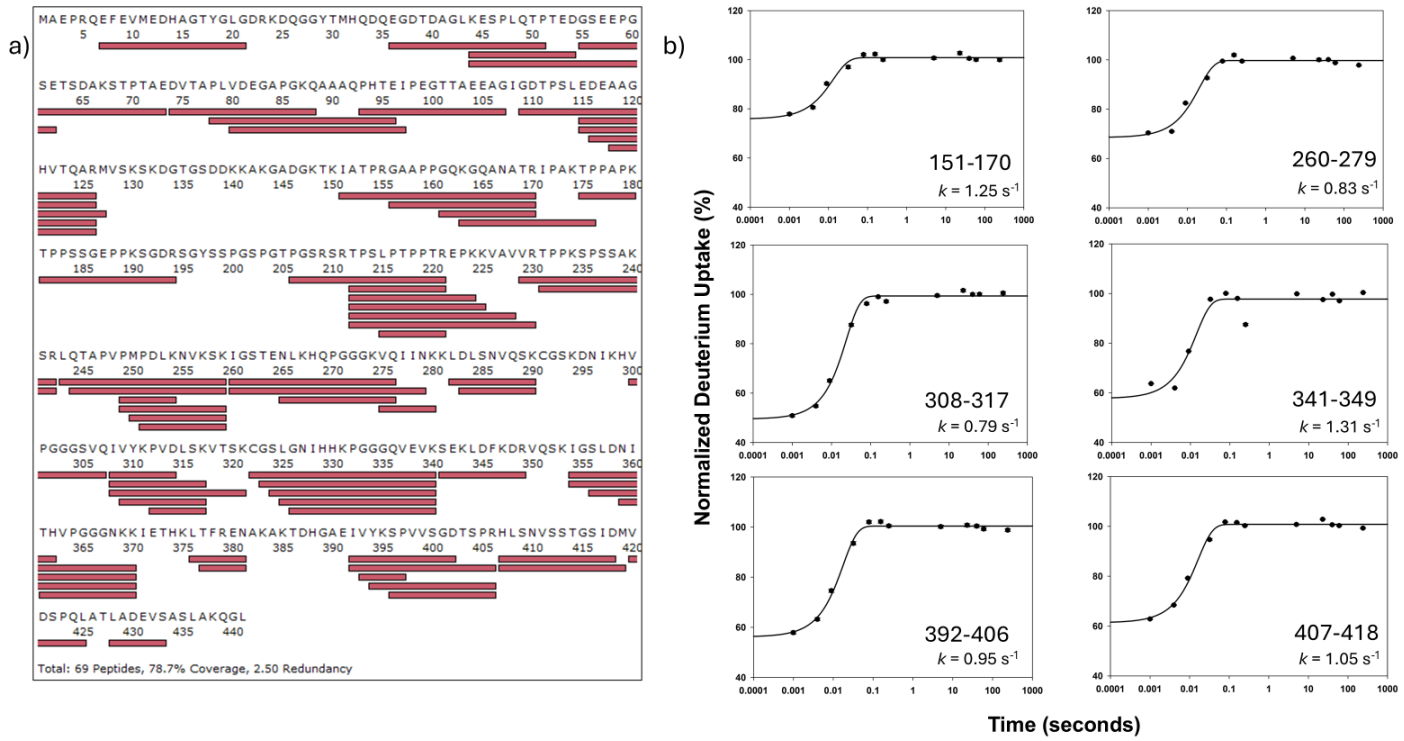


Figure 3.1 | Discrete time point mode of operation with LC separation. (a) The number of observable peptides for Tau increased to 78.7% coverage with 2.50 redundancy. (b) Uptake curves for Tau peptides and their respective rates obtained from CFI-TRESI-HDX with LC separation and discrete time points ranging from 50 ms to 4 h. The exchange data were normalized to 100%, with back-exchange levels ranging between 30 and 40%.[58]

To validate the performance of the automated platform prior to its implementation for characterization of additional phosphorylation states, tau phosphorylated by glycogen synthase kinase 3β (GSK3β) was analyzed as a positive control. GSK3β-mediated phosphorylation of tau has been extensively characterized previously and was therefore selected as a benchmark for assessing whether the automated system reproduced known phosphorylation-induced structural changes.

3.4.2. Automated CFIT-TRESI-HDX reproduces previously observed conformational effects of GSK3β-mediated tau phosphorylation

HDX-MS analysis of GSK3β-phosphorylated tau demonstrated uptake patterns consistent with those previously observed using earlier TRESI-HDX configurations (Figure 3.2).[52] Relative to unmodified tau, hyperphosphorylated tau exhibited increased deuterium incorporation across multiple regions of the protein, indicating increased solvent accessibility and reduced structural protection.

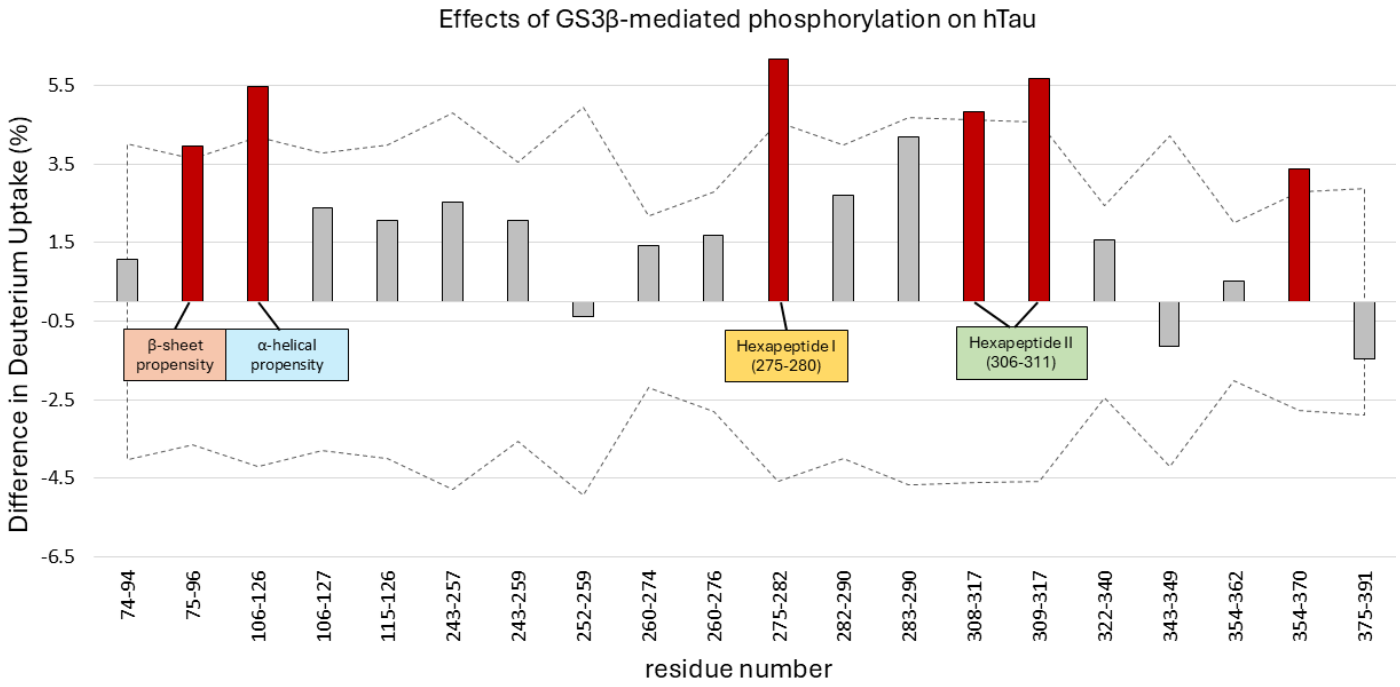


Figure 3.2 | Differential CFI-TRESI-HDX on GSK3β-mediated tau hyperphosphorylation. An increase in deuterium uptake was observed in peptides in the microtubule-binding domain (Hexapeptide I and II) and parts of the N- and C-terminus, represented by red bars, while grey bars represent non-significant changes. Significance was defined as uptake exceeding the propagated error (2σ) threshold for three technical replicates.

The observed increases in deuterium uptake were consistent with disruption of transient long-range intramolecular contacts that are believed to stabilize native tau conformations. Although tau lacks a stable tertiary structure, numerous studies have proposed that native tau adopts a compact conformational ensemble maintained through weak interactions between the N-terminal region, proline-rich domain, and microtubule-binding region. Phosphorylation by GSK3β appeared to weaken these interactions, shifting the conformational ensemble toward more extended and solvent-accessible states.

Particularly notable increases in deuterium uptake were observed within and adjacent to the microtubule-binding region, including peptides encompassing the aggregation-prone hexapeptide I (275-280) and II (306-311) motifs. These motifs constitute the structural core of paired helical filaments (PHFs) and neurofibrillary tangles (NFTs) found in Alzheimer's disease (AD) and related tauopathies. Increased exposure of these regions following phosphorylation supports the hypothesis that hyperphosphorylation facilitates aggregation by increasing solvent accessibility of amyloidogenic motifs.

Importantly, the reproduction of these previously reported HDX signatures confirmed that the automated CFIT-TRESI-HDX workflow accurately captured biologically relevant conformational changes, along with high sequence coverage (Figure S3.6), providing confidence for subsequent studies investigating less-characterized kinase systems.

3.4.3. Identification of MARK4 and Fyn-Mediated Tau Phosphorylation

Following validation of the automated CFI-TRESI platform, attention was directed toward characterizing conformational changes induced by phosphorylation with microtubule affinity-regulating kinase 4 (MARK4) and Fyn kinase. Initial assessment of kinase activity was performed using SDS-PAGE analysis. In contrast to GSK3β-hyperphosphorylated tau, neither MARK4- nor Fyn-treated samples exhibited a mobility shift relative to unmodified tau (Figure S3.7). These observations suggested that phosphorylation stoichiometry alone was insufficient to produce large electrophoretic changes, highlighting the limitations of gel-based approaches for confirming modification of intrinsically disordered proteins.

To verify phosphorylation and identify modification sites, phosphopeptide enrichment using immobilized metal affinity chromatography (IMAC) followed by tandem mass spectrometry (MS/MS) analysis was performed (S3.8). Site mapping confirmed successful phosphorylation of tau by both MARK4 and Fyn kinases at Ser356 and Tyr18 residues, respectively. These residues have been associated with their involvement in the formation of pathological tau species.[99] These experiments further established that the absence of an electrophoretic shift did not indicate a lack of phosphorylation but rather reflected the limited sensitivity of gel-based methods for detecting subtle changes in highly disordered proteins.

3.4.4. Kinase-specific phosphorylation produces distinct phospho-tau conformational ensembles

Differential HDX-MS analysis following phosphorylation by GSK3β, MARK4, and Fyn revealed that the structural consequences of tau phosphorylation are highly dependent on the identity of the modifying kinase and the residues targeted. These observations support an emerging view of tau biology in which phosphorylation acts not merely as a cumulative post-translational modification but as a conformational regulator capable of redistributing the intrinsically disordered tau ensemble into structurally and functionally distinct substates. Increasing evidence suggests that different phosphorylation patterns encode unique conformational biases that ultimately influence tau function, aggregation propensity, and cellular toxicity.

Phosphoproteomic analysis confirmed phosphorylation of Ser356 following MARK4 treatment, consistent with the established substrate specificity of MARK family kinases. Phosphorylation within the microtubule-binding region, particularly at Ser262 and Ser356, has been widely implicated in the early stages of tau dysfunction due to its ability to weaken tau–microtubule interactions and increase the pool of soluble cytosolic tau available for pathological self-association. The HDX-MS data demonstrate that MARK4-mediated phosphorylation is accompanied by widespread increases in deuterium incorporation across multiple domains of the protein, indicative of reduced conformational protection and increased accessibility of the backbone amide network.

The most pronounced effects were observed within the microtubule-binding region, particularly in peptides encompassing and flanking hexapeptide II (residues 306–311) (Figure 3.3a). This sequence forms a key component of the ordered β-sheet core present in paired helical filaments and neurofibrillary tangles and is recognized as one of the principal aggregation-driving motifs within tau. Increased exchange within this region suggests that MARK4 phosphorylation shifts the conformational equilibrium toward states in which aggregation-prone elements become more solvent-exposed and therefore more available for intermolecular interactions. Similar increases in uptake were also detected within portions of the N-terminal and C-terminal regions that

have previously been reported to retain residual structural organization despite the intrinsically disordered nature of tau. Collectively, these observations indicate that phosphorylation-induced destabilization extends beyond the immediate vicinity of the modification site and propagates through long-range intramolecular interactions that normally contribute to maintaining compact conformational substates.

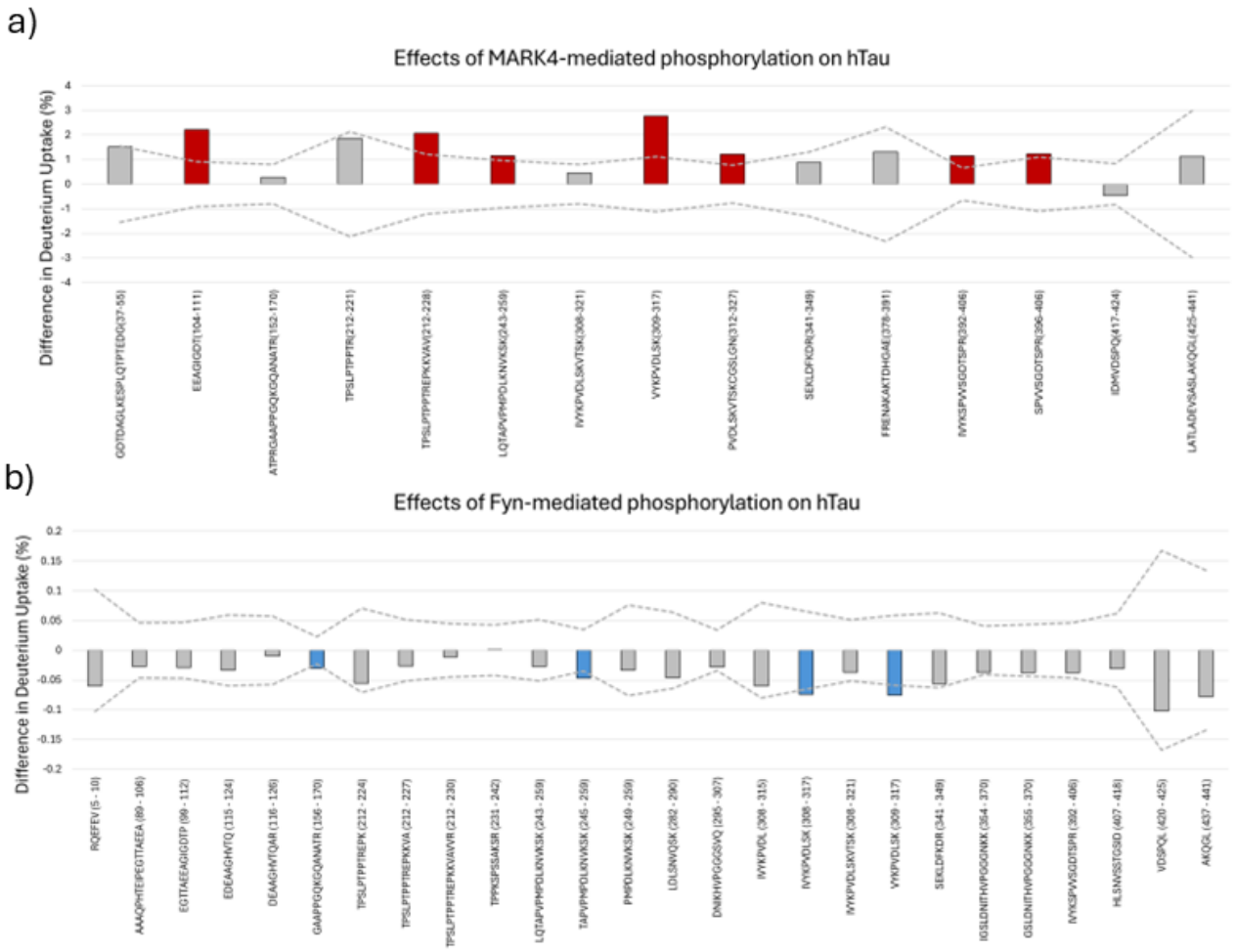


Figure 3.3 | Differential CFI-TRESI-HDX on phosphorylated tau. Differential CFI-TRESI-HDX analysis of tau following phosphorylation by MARK4 and Fyn. (a) MARK4-phosphorylated tau exhibited increased deuterium uptake, represented by red bars, indicative of enhanced solvent accessibility and reduced conformational stability. (b) Fyn-phosphorylated tau displayed decreased deuterium uptake in specific regions, represented by blue bars, consistent with increased conformational protection and stabilization of the highlighted peptides. Grey bars represent non-significant changes. Significance was defined as uptake exceeding the propagated error (2σ) threshold for three technical replicates.

These findings are consistent with current models proposing that phosphorylation within the repeat domain promotes aggregation not solely through electrostatic perturbation, but through redistribution of the conformational ensemble toward aggregation-competent states. In this context, MARK4 appears to function as a structural modulator that increases exposure of regions required for pathological self-association while simultaneously destabilizing residual tertiary contacts that contribute to the native ensemble.

In contrast, phosphorylation by Fyn generated a markedly different HDX signature characterized predominantly by localized reductions in deuterium incorporation and increased protection from solvent exchange (Figure 3.3b). Whereas MARK4 phosphorylation promoted widespread destabilization, Fyn phosphorylation appeared to stabilize specific regions of the protein and induce the formation of alternative intramolecular interactions. The most pronounced changes were observed within the microtubule-binding region surrounding hexapeptide II, accompanied by additional protection within the N-terminal region, particularly residues 156–170. Although spatially distant in the primary sequence, these regions have previously been implicated in long-range interactions that contribute to higher-order organization within the tau ensemble.

The observed decrease in exchange suggests that phosphorylation at Tyr18 promotes formation of a more compact and structurally organized conformational subpopulation. Importantly, this increased protection should not be interpreted as restoration of a native or non-pathological state. Rather, it likely reflects stabilization of a distinct phospho-tau ensemble. Fyn is increasingly recognized as a critical mediator of synaptic dysfunction in Alzheimer's disease through its interactions with tau and downstream signalling partners. Previous studies have demonstrated that Fyn-dependent phosphorylation facilitates recruitment of signalling complexes involved in excitotoxicity and neuronal toxicity. Consequently, the enhanced protection observed by HDX-MS may reflect conformational states optimized for protein–protein interactions rather than aggregation.

Further support for kinase-specific conformational remodelling was obtained through circular dichroism (CD) spectroscopy (Figure 3.4). Both MARK4- and Fyn-phosphorylated tau exhibited spectral features distinct from those of unmodified tau, indicating measurable changes in secondary structural bias. Notably, Fyn-phosphorylated tau displayed evidence of increased structural organization and α-helical propensity relative to both native tau and MARK4-phosphorylated tau. Although interpretation of secondary structure within intrinsically disordered proteins remains inherently challenging, the spectroscopic data are consistent with the HDX-MS findings and support the existence of a more ordered conformational ensemble following Fyn phosphorylation.

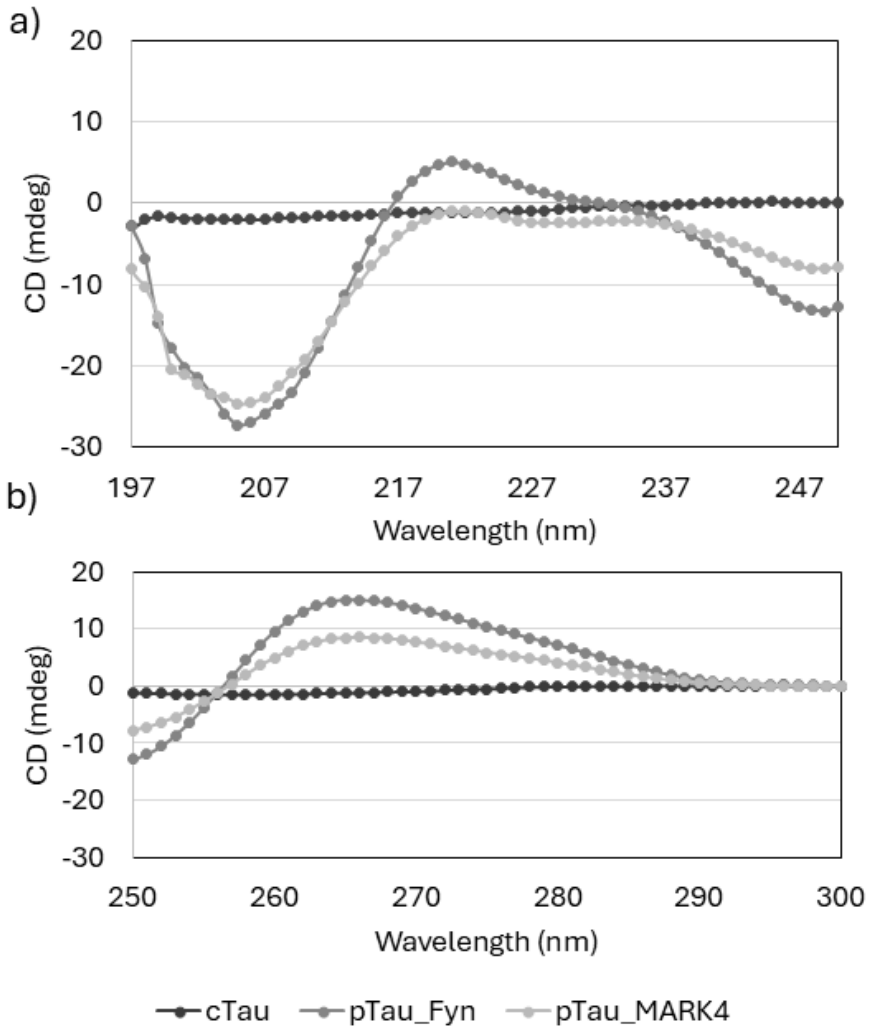


Figure 3.4 | Monitoring the spectrum from CD spectroscopy of native and phosphorylated tau. The CD spectra for (a) far- and (b) near- UV regions indicate potential changes in the secondary and tertiary structure upon MARK4- and Fyn-mediated phosphorylation.

Taken together, the HDX-MS and spectroscopic data reveal that phosphorylation remodels the tau conformational landscape through multiple, kinase-dependent structural pathways. Rather than producing a uniform hyperphosphorylated state, individual kinases selectively stabilize distinct conformational substates within the broader tau ensemble. MARK4 phosphorylation promotes destabilization of residual intramolecular contacts and enhanced exposure of aggregation-prone motifs within the microtubule-binding region, consistent with a mechanism that facilitates amyloid formation and neurofibrillary tangle development. In contrast, Fyn phosphorylation favours a more structurally organized ensemble characterized by increased protection from solvent exchange, suggesting a mechanistic role in pathological signalling processes rather than direct promotion of aggregation. These findings support a growing paradigm in which the progression of Alzheimer's disease is driven not simply by the accumulation of phosphorylated tau, but by the emergence of structurally distinct phospho-tau species possessing unique biochemical and pathological properties.

More broadly, this work demonstrates the utility of millisecond HDX-MS for resolving subtle conformational biases within highly dynamic intrinsically disordered proteins. By combining automated CFI-TRESI-HDX with

phosphoproteomics and complementary spectroscopic measurements, this study provides a framework for linking site-specific post-translational modifications to structural outcomes that are inaccessible to conventional structural biology approaches. The ability to distinguish kinase-dependent phospho-tau ensembles offers new opportunities for understanding the molecular origins of tau heterogeneity in neurodegenerative disease and highlights the potential of kinase-specific therapeutic strategies aimed at selectively targeting pathogenic conformational states before the onset of irreversible aggregation.

3.5. Conclusion

Tau hyperphosphorylation is a defining feature of Alzheimer's disease and related tauopathies; however, the structural consequences of individual phosphorylation events remain poorly understood. In this study, millisecond HDX-MS, phosphoproteomics, and circular dichroism spectroscopy were combined to investigate how phosphorylation by GSK3β, MARK4, and Fyn alters the conformational ensemble of full-length human tau.

Implementation of an automated Continuous Flow Injection Time-Resolved Electrospray Ionization HDX-MS (CFI-TRESI-HDX) workflow provided a robust and reproducible platform for studying the rapid conformational dynamics of this intrinsically disordered protein. Validation using GSK3β-hyperphosphorylated tau successfully reproduced previously reported conformational signatures, confirming the suitability of the automated platform for phospho-tau studies.

Phosphoproteomic analysis confirmed phosphorylation at Ser356 following MARK4 treatment and Tyr18 following Fyn treatment. Differential HDX-MS revealed that the structural consequences of phosphorylation were strongly kinase dependent. MARK4 phosphorylation increased deuterium uptake across multiple regions of tau, particularly within the microtubule-binding domain and around the aggregation-prone hexapeptide II motif, consistent with destabilization of residual intramolecular interactions and increased exposure of aggregation-relevant sequences. In contrast, Fyn phosphorylation produced localized decreases in deuterium uptake, indicative of increased conformational protection and stabilization of a more structurally organized ensemble. These observations were further supported by circular dichroism spectroscopy, which suggested increased structural ordering following Fyn-mediated phosphorylation.

Collectively, these findings demonstrate that tau does not adopt a single pathological phospho-state. Rather, individual kinases generate distinct phospho-tau conformational ensembles that may contribute to disease progression through different molecular mechanisms. While GSK3β and MARK4 phosphorylation favour conformations associated with microtubule dissociation and increased aggregation propensity, Fyn phosphorylation appears to stabilize conformational states that may facilitate pathological signaling interactions. These results highlight the importance of site-specific phosphorylation patterns in regulating tau structure and function and provide new insight into the molecular heterogeneity underlying tauopathies.

More broadly, this work demonstrates the value of millisecond HDX-MS for characterizing subtle conformational changes within intrinsically disordered proteins and establishes a framework for linking kinase-specific phosphorylation events to structural outcomes relevant to neurodegenerative disease.

CHAPTER 4

Development of a Targeted LC-MS Proteomics Workflow for Quantitative Analysis of Clinical Protein Biomarkers in Human Serum

Ayesha Maqsood[1], Kerene Brown[2], and Derek J. Wilson[1]

[1] *Department of Chemistry, York University, Toronto, M3J 1P3, Canada*

[2] *Product and Development, Dynacare, Brampton, Ontario, L6T 5M3.*

This work was conducted at the Product & Service Development Laboratory at Dynacare. **A.M.** designed and conducted the method development and validation. K.B. and D.J.W. provided supervision.

4.1. Summary

Mass spectrometry (MS)–based proteomics has emerged as a powerful platform for clinical diagnostics due to its high specificity, sensitivity, and multiplexing capability.[104,105] However, translating proteomics workflows into robust clinical assays remains challenging, particularly with respect to reproducibility, quantitation, and sample complexity.[105,106] In this work, we present the development of a bottom-up proteomics method using liquid chromatography-mass spectrometry (LC-MS) aimed at targeted quantitation of clinically relevant proteins in human serum.

Method development was performed using standard proteins to systematically evaluate proteolytic digestion efficiency, chromatographic resolution, and peptide ionization under reversed-phase LC conditions coupled to electrospray ionization mass spectrometry. The optimized workflow was subsequently applied to complex biological matrices, with human serum used to assess analytical performance for clinically relevant biomarkers, including human thyroglobulin and albumin. A quantitative LC-MS method was developed using multiple reaction monitoring (MRM) to address challenges associated with wide dynamic range, matrix effects, and ion suppression inherent to serum proteomics.

This work highlights the feasibility of MS-based proteomics as an alternative or complementary approach to immunoassays in clinical diagnostics, laying the foundation for future expansion of multiplexed protein panels. It also emphasizes the analytical robustness, reproducibility, and compatibility with clinically relevant sample matrices and throughput requirements, addressing key barriers that often limit the translation of bioanalytical MS methods into real-world clinical implementation.

4.2. Introduction

Mass spectrometry (MS)-based proteomics has emerged as a powerful analytical platform for the characterization and quantitation of proteins in increasingly complex biological systems.[105,106] While much of modern proteomics research has focused on structural characterization and conformational analysis of proteins, there has also been substantial growth in the application of MS toward targeted protein quantitation in clinical diagnostics.[107,108] The work presented throughout this thesis primarily focuses on the characterization of ordered and intrinsically disordered proteins using hydrogen-deuterium exchange mass spectrometry (HDX-MS). However, this chapter expands the broader theme of the thesis by demonstrating how mass spectrometry can additionally be implemented for quantitative protein analysis in clinically relevant matrices.

Protein biomarkers are widely used in clinical diagnostics because their concentration can reflect physiological or pathological states associated with disease progression, tissue damage, or therapeutic response.[108,109] Accurate detection and quantitation of protein biomarkers are therefore critical for disease diagnosis, prognosis, and treatment monitoring.[109] Traditionally, clinical protein quantitation has relied heavily on immunochemical techniques such as enzyme-linked immunosorbent assays (ELISA), chemiluminescence assays, and radioimmunoassay.[110–112] Although these approaches are well established in clinical laboratories, they possess several limitations, including antibody cross-reactivity, batch-to-batch variability, limited multiplexing capability, long development timelines, and high reagent costs.[113]

Mass spectrometry-based proteomics offers a compelling alternative to conventional immunoassays due to its high analytical specificity and selectivity, as well as its multiplexing capability.[106,114] In contrast to immunoassay-based methods, LC-MS approaches identify analytes based on their accurate mass, retention time, and fragmentation patterns, thereby reducing the probability of false-positive identification.[113] Furthermore, targeted proteomics workflows permit simultaneous monitoring of multiple proteins or peptides within a single analytical run, increasing throughput and improving analytical efficiency.[114]

Targeted bottom-up proteomics is one of the most commonly implemented strategies for quantitative LC-MS workflows. In this approach, intact proteins are enzymatically digested into peptides, followed by chromatographic separation and mass spectrometric analysis of peptides representative of their parent protein. Quantitation can be subsequently achieved using multiple reaction monitoring (MRM), which can specifically quantify the target peptide along with quality controls and calibration standards.[115]

This chapter demonstrates how mass spectrometry can bridge both structural characterization and quantitative analysis of proteins. Whereas previous chapters focused on protein conformational dynamics using HDX-MS, the work described here illustrates the translational application of MS toward clinically relevant biomarker quantitation. Specifically, a simplified and robust targeted LC-MS workflow was developed for quantitative analysis of serum proteins using a quadrupole time-of-flight (QTOF) mass spectrometer. The workflow was initially optimized using bovine serum albumin (BSA) as a protein standard before being implemented for quantitative analysis of human albumin and thyroglobulin in serum and plasma matrices.

The overall objective of this work was to establish a streamlined LC-MS-based proteomics workflow capable of supporting future clinical biomarker assays while reducing workflow complexity and manual method development burden. Although the analytical sensitivity achieved using the QTOF platform did not match that typically attainable using triple quadrupole (QQQ) instrumentation with peptide enrichment, the work establishes a strong proof-of-concept for clinically adaptable targeted proteomics.

4.3. Experimental procedures

4.3.1. Proteolysis of human albumin and thyroglobulin

Human albumin and thyroglobulin (TG) (purchased from Millipore Sigma) were digested using an optimized bottom-up proteomics workflow. Briefly, the protein was denatured in 5 M urea prepared in 50 mM ammonium bicarbonate and incubated at room temperature for 15 min. Disulfide bonds were reduced using 5 mM tris(2-carboxyethyl) phosphine (TCEP), followed by alkylation with 30 mM 2-chloroacetamide for 30 min at room temperature. A total of 200 µg of denatured protein was digested with sequencing-grade trypsin (6.7 µg) (purchased from Sigma Aldrich) at 37 °C for 1 h. Proteolysis was terminated by acidification with formic acid to a final concentration of 5%. Calibration standards and quality control (QC) samples were prepared by spiking digested peptides into 200 µL of charcoal-treated human serum. Bovine serum albumin (BSA) digest was added to all samples as an internal standard at a final amount of 100 fmol. Calibration standards contained 0, 1, 2, 5, 10, 25, and 70 µg of Tg digest, while QC samples contained 30 and 50 µg of TG digest.

4.3.2. Solid-phase extraction of the digested protein biomarkers

Peptide cleanup was performed using Sep-Pak C18 solid-phase extraction cartridges (Waters, Milford, MA, USA). Cartridges were conditioned with 3 mL of 0.1% formic acid (FA) in acetonitrile (ACN) and equilibrated with 3 mL of 0.1% FA in water. Individual calibration standards and QC samples (200 µL) were loaded onto separate cartridges and washed sequentially with 3 mL of 5% methanol in 0.1% FA and 3 mL of 0.1% FA in water to remove salts and matrix components. Bound peptides were eluted with 1 mL of 80% ACN and concentrated to dryness under a stream of nitrogen. Dried samples were reconstituted in 100 µL of 0.1% FA in water prior to LC–MS/MS analysis.

4.3.3. Quantitation of human albumin and thyroglobulin using MRM-HR mass spectrometry

A 20 µL of digested protein was injected using Sciex Exion LC pumps and autosamplers onto the Kinetex C18 (2.6 µm) column and reverse-phase separated at 0.3 uL/min using a linear gradient from 5 to 60% Buffer B (0.1% FA in ACN) over 5 minutes. Eluted peptides were ionized using electrospray ionization into the Sciex x500r Quadrupole-Time-of-Flight (Q-TOF) instrument under positive ion mode. The peptide of interest (m/z of 507.2 for albumin and 636.8 for thyroglobulin) was selectively fragmented, and five transitions along with their optimal collision energies (CE) were recorded for quantitation using MRM-HR. Calibration curves were constructed using five calibrants for albumin and six calibrants for thyroglobulin, as well as two quality control samples. Quantitative analysis was normalized using internal peptide standards, including BSA-derived peptides. Linear regression analysis was subsequently performed to determine calibration curve correlation coefficients and evaluate quantitative performance.

4.4. Results and Discussion

4.4.1. Development of a Simplified Bottom-Up Proteomics Workflow

A major objective of this work was the development of a simplified yet reproducible sample preparation workflow that could be completed within a timeframe compatible with future clinical proteomics applications. Unlike highly specialized research workflows that often require extensive manual optimization and lengthy processing times, the present study focused on establishing a generalized method that could be readily adapted for the quantitation of multiple protein biomarkers in a clinical laboratory setting. Emphasis was placed on minimizing sample handling steps while maintaining analytical robustness, reproducibility, and proteolytic efficiency.

The workflow began with protein denaturation using urea, followed by reduction of disulfide bonds with tris(2-carboxyethyl) phosphine (TCEP). Several parameters, including incubation temperature and reaction time, were optimized to maximize reduction efficiency while minimizing overall sample preparation time. Under the conditions evaluated, TCEP provided efficient reduction without the prolonged incubation periods often required for dithiothreitol (DTT). Furthermore, the reduction and alkylation steps could be performed sequentially within the same workflow without negatively affecting downstream proteolytic digestion, thereby simplifying sample preparation and improving throughput.

To further reduce processing time, trypsin was selected as the proteolytic enzyme due to its high specificity for lysine and arginine residues and its ability to generate peptides that are well suited for LC-MS analysis. The

predictable peptide products produced by tryptic digestion facilitate reproducible peptide mapping, robust protein identification, and targeted quantitative analysis. Digestion conditions were systematically optimized by evaluating different temperatures (25°C, 37°C, and 55°C), incubation times ranging from 5 min to 24 h, and mixing conditions with and without agitation. Optimization criteria were based on the generation of high-intensity signals for characteristic peptides while maintaining reproducible digestion profiles.

The optimized digestion conditions were initially evaluated using bovine serum albumin (BSA) as a model protein to assess chromatographic reproducibility and peptide generation in a controlled system. The workflow was subsequently applied to protein-spiked charcoal-stripped serum and protein-spiked human serum samples. Charcoal-stripped serum, which is depleted of endogenous hormones, steroids, lipids, and other small molecules, was used to reduce background interference during method development. These experiments demonstrated that efficient denaturation and adequate enzyme accessibility were critical for achieving high peptide yield and reproducible digestion patterns within complex biological matrices.

Following optimization of the digestion protocol, the necessity of a sample clean-up step was evaluated. Because future clinical implementation would benefit from rapid sample processing, it was important to determine whether acceptable analytical performance could be achieved without additional sample preparation. Initially, 20 µL of the digested sample was diluted in 0.1% formic acid in water and directly injected onto the LC-MS system without further processing (Figure 4.1a). The remaining digest was subjected to C18 solid-phase extraction (SPE) to remove salts, residual reagents, and matrix-derived interferences prior to analysis.

To minimize processing time during SPE, a positive-pressure manifold was employed. This system uses a stream of high-purity nitrogen gas to facilitate solvent evaporation following the SPE elution step while allowing multiple samples to be processed simultaneously, thereby improving sample throughput. A reconstitution volume of 200 µL was selected to reduce solvent evaporation time while maintaining sufficient analyte concentration for LC-MS analysis. Following SPE clean-up, samples were reconstituted in 0.1% formic acid in water, and 20 µL was injected onto the LC-MS system.

Comparison of the resulting chromatograms demonstrated a substantial improvement in analytical sensitivity following SPE clean-up. The intensity of the representative peptide increased from approximately 580 counts per second (cps) prior to SPE to approximately 23,000 cps after SPE treatment, corresponding to an approximately 40-fold enhancement in signal intensity (Figure 4.1b). This increase is consistent with the removal of matrix-derived interferences and improved ionization efficiency following sample clean-up.

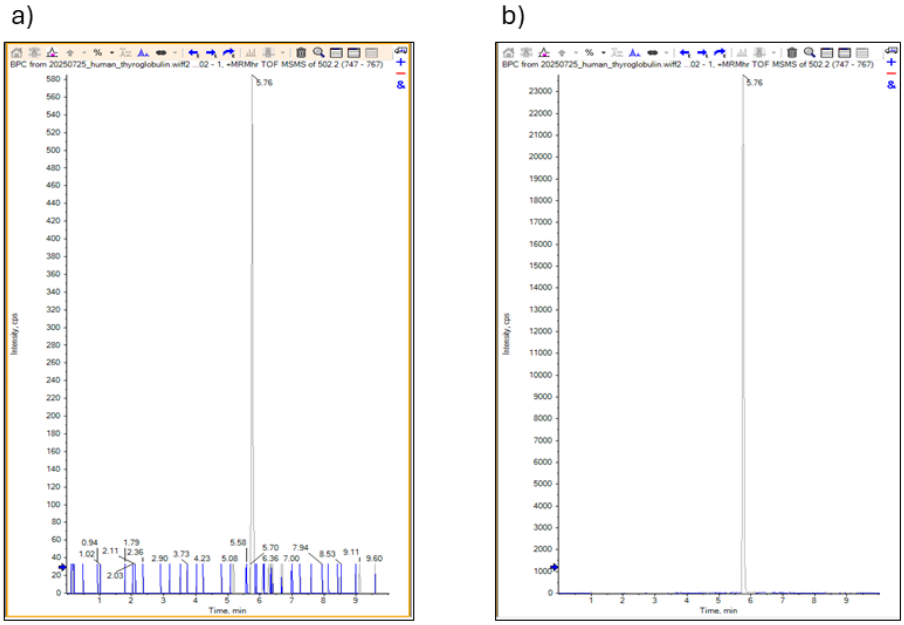


Figure 4.1 | Base Peak Chromatogram demonstrating the increase in peptide intensity upon SPE cleanup. The intensity of the representative peptide increased from (a) about 580 counts per second without SPE cleanup to (b) about 23000 counts per second with SPE cleanup.

Collectively, these results established the optimal digestion conditions and demonstrated the importance of incorporating an SPE clean-up step to achieve sufficient analytical sensitivity and data quality. Although SPE introduces an additional sample preparation step, the overall workflow remains operationally simple, reproducible, and readily adaptable to clinical laboratory environments. By prioritizing workflow simplicity, throughput, and analytical performance, the method provides a practical foundation for future targeted LC-MS-based protein biomarker assays.

4.4.2. LC-MS Method Optimization

Following optimization of the sample preparation workflow, chromatographic conditions were evaluated to develop a rapid LC-MS method suitable for high-throughput protein biomarker analysis. A major objective of this study was to minimize total analysis time while maintaining adequate chromatographic performance, peptide detectability, and quantitative reproducibility. Since future clinical implementation may require the analysis of large sample cohorts, reducing instrument run times is critical for improving laboratory throughput and reducing per-sample analysis costs.

Traditional bottom-up proteomics methods frequently employ chromatographic gradients ranging from 15 to 90 min to maximize peptide separation and proteome coverage. While these approaches are highly effective for discovery-based proteomics applications, they are often impractical for targeted clinical assays where only a limited number of predefined protein biomarkers are monitored. Therefore, this work focused on developing a rapid targeted LC-MS method using a total gradient length of 5 min.

Several gradient conditions were evaluated to achieve sufficient retention and separation of the target peptides while minimizing analysis time. Optimization criteria included peak shape, chromatographic resolution, retention

time reproducibility, signal intensity, and total run duration. Particular attention was given to ensuring that the target peptides eluted within a narrow retention window while remaining sufficiently separated from matrix-derived background components. The optimized method employed a reversed-phase C18 analytical column operated under acidic conditions using water and acetonitrile containing 0.1% formic acid as the mobile phases. A rapid linear gradient was used to elute the target peptides within a 5 min chromatographic run (S4.6 and S4.7). The use of formic acid enhanced peptide protonation during electrospray ionization while maintaining compatibility with mass spectrometric detection.

Retention time reproducibility was evaluated through repeated injections of protein-spiked serum samples. Minimal variation in retention time was observed across replicate analyses, demonstrating the robustness of the chromatographic method. This level of reproducibility is particularly important for targeted proteomics workflows, where accurate peak identification and integration rely on consistent chromatographic performance.

The implementation of a 5 min gradient significantly increased sample throughput compared with conventional proteomics workflows. Assuming continuous operation, the optimized method would permit the analysis of substantially more samples per day than traditional long-gradient approaches, making it more suitable for future clinical laboratory implementation. Importantly, this increase in throughput was achieved without compromising peptide detection or overall analytical performance (Figure 4.2).

a) b)

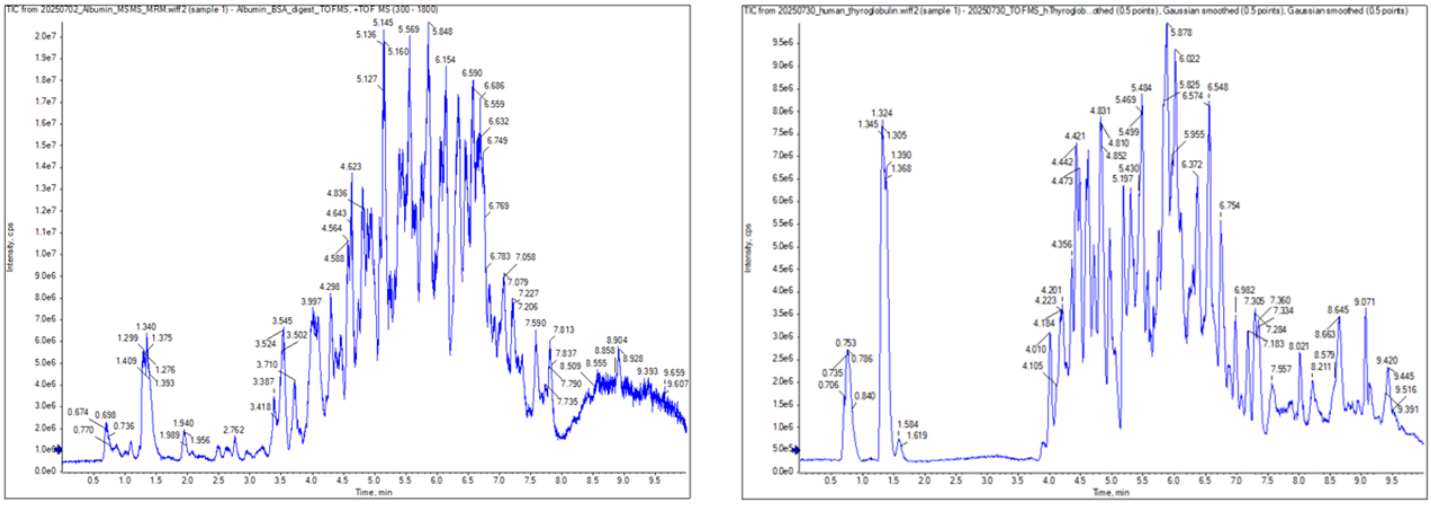


Figure 4.2 | A total ion chromatogram of digested proteins of (a) Albumin and (b) human Thyroglobulin over a 5-minute LC gradient.

Collectively, these results demonstrate that rapid chromatographic separations can be successfully integrated with the optimized sample preparation workflow developed in this study. The resulting method provides a balance between analytical sensitivity, reproducibility, and throughput, supporting its potential application in targeted LC-MS-based protein biomarker quantitation within clinical laboratory environments.

4.4.3. Quantitation of Human Albumin

The optimized workflow was first evaluated for the quantitative analysis of human albumin. Albumin was selected as a clinically relevant model biomarker due to its high abundance in serum, well-established physiological role as the primary transport protein in circulation, and its routine use as an indicator of nutritional status, liver function, and renal disease progression.[116–118] In addition, its relatively high serum concentration provided an ideal system for assessing the analytical performance of the developed LC-MS workflow prior to application to lower-abundance protein biomarkers.

A proteotypic peptide commonly used for albumin quantitation was identified following tryptic digestion and subjected to tandem mass spectrometric characterization. Product ion spectra were acquired to confirm peptide identity and to identify high-intensity fragment ions suitable for targeted analysis (Table S4.1). Guided MRM-high resolution (MRM-HR) acquisition strategies were subsequently implemented to monitor multiple fragment ion transitions originating from the selected precursor ion. Monitoring several transitions increased confidence in peptide identification while improving analytical specificity within the complex serum matrix. Quantitation was performed using digested bovine serum albumin (BSI) internal standard to compensate for variability introduced during sample preparation, chromatographic separation, and electrospray ionization.

Method performance was evaluated through the construction of calibration curves consisting of five calibrators spanning the expected concentration range, together with two independent quality control samples. Linear regression analysis demonstrated excellent linearity across the calibration range, yielding a correlation coefficient (r) of 0.999 (Figure 4.3). The quality control samples were quantified within acceptable limits of the nominal concentrations, demonstrating satisfactory assay accuracy and reproducibility.

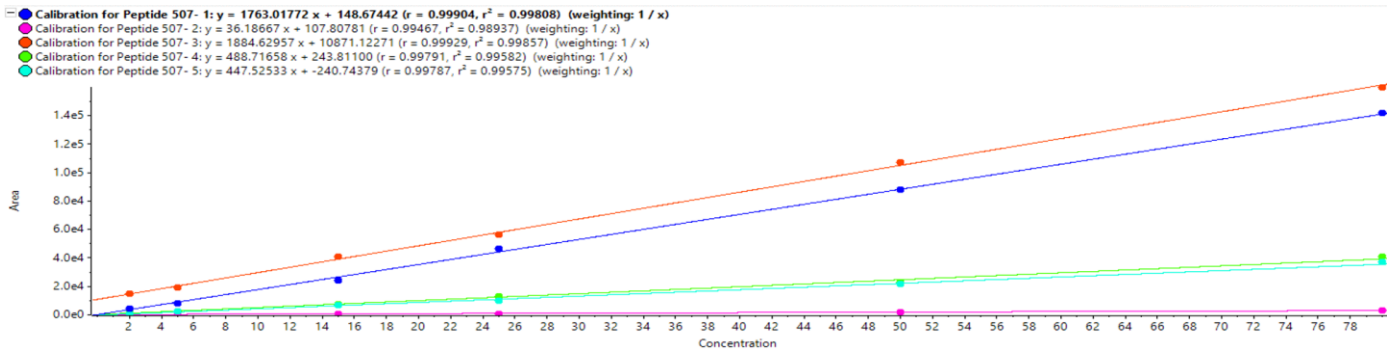


Figure 4.3 | Calibration curve for a characteristic peptide for the quantitation of human Albumin using five calibrants, two quality controls and an internal standard. A correlation coefficient of the calibration curve (r) was obtained by fitting the data to a linear regression model.

Collectively, these results demonstrate that the optimized sample preparation and LC-MS workflow can reliably quantify protein biomarkers in complex serum matrices. The excellent linearity achieved for albumin, together with the reproducible chromatographic and mass spectrometric performance, establishes a strong analytical foundation for the application of the method to lower-abundance protein targets. Furthermore, successful

quantitation of unknown albumin concentrations confirmed the suitability of the workflow for targeted clinical proteomics applications.

4.4.4. Quantitation of Thyroglobulin (TG)

Following successful implementation of the workflow for albumin quantitation, the method was applied to the targeted analysis of thyroglobulin (TG). TG is a clinically important biomarker used in the monitoring of differentiated thyroid cancer following thyroidectomy and radioactive iodine treatment.[119,120] Unlike albumin, TG is typically present at substantially lower concentrations in circulation and is frequently affected by analytical interferences encountered in conventional immunoassays, particularly in the presence of anti-thyroglobulin autoantibodies.[119] Consequently, TG represents an analytically challenging target and serves as an appropriate model for evaluating the clinical applicability of LC-MS-based protein quantitation workflows.[121]

Following tryptic digestion and chromatographic separation, several TG-derived peptides were detected with sufficient signal intensity for targeted analysis. Several peptides were identified at high intensity, suitable for MRM analysis. Among the detected peptides, the precursor ion at m/z 638.8 produced the highest signal intensity and was selected for further optimization. Collision energy optimization was performed on the selected peptide by incrementally increasing the collision energy from 0 to 150 V while monitoring the response of five candidate fragment ion transitions. The optimal collision energy for each transition was determined based on fragment ion abundance and signal reproducibility (Figure 4.4 a). These optimized parameters were subsequently incorporated into the final MRM acquisition method to ensure reliable peptide identification and quantity within the complex serum matrix. The use of multiple high-resolution transitions provided additional confidence in analyte identification while minimizing the likelihood of matrix-related interferences (Table S4.1).

Quantitative analysis was conducted using six calibrators spanning the target concentration range together with two quality control samples and an internal standard. A calibration curve was generated and fitted using a linear regression model. Excellent linearity was observed across the evaluated concentration range, yielding a correlation coefficient (r) of 0.9989 (Figure 4.4b). The quality control samples demonstrated consistent quantitative performance, supporting the reproducibility of the assay.

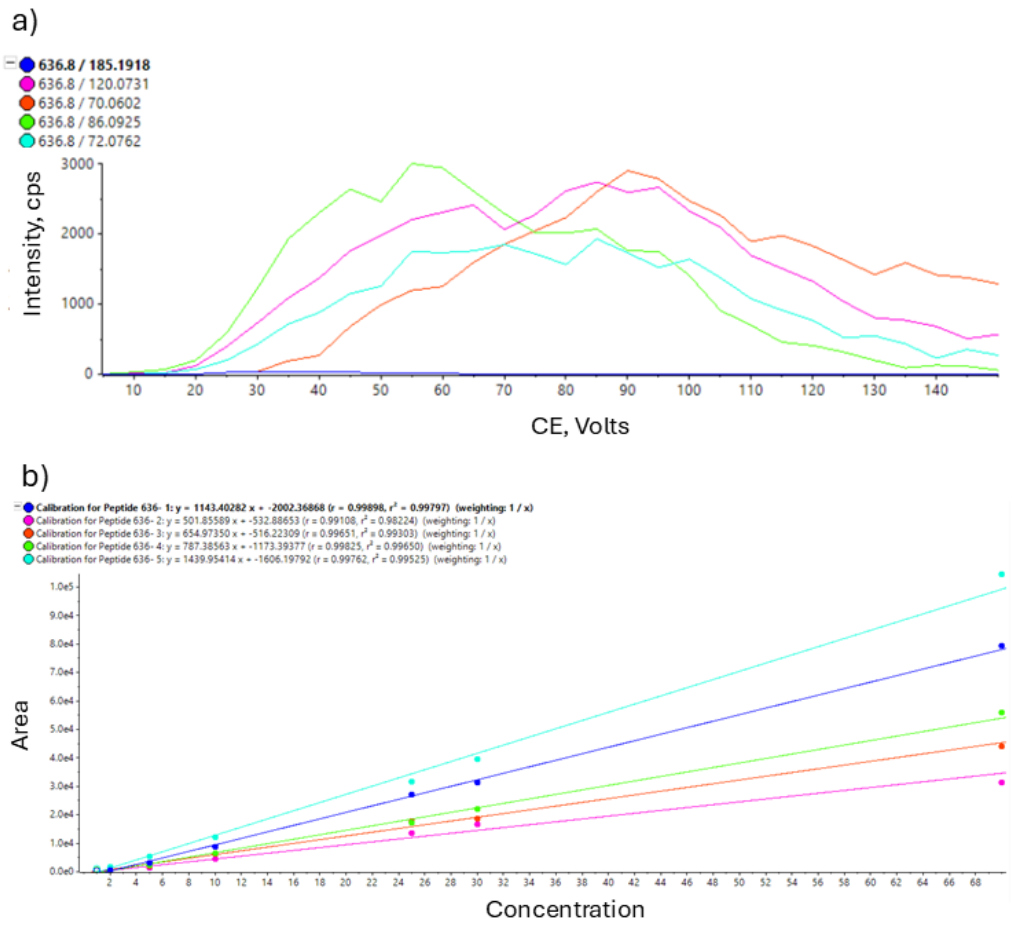


Figure 4.4 | Calibration curve for a characteristic peptide for the quantitation of human Thyroglobulin using six calibrants, two quality controls and an internal standard. (a) The optimal collisional energies (CE) for each of the five transition states of the peptide were obtained. (b) A correlation coefficient of the calibration curve (r) was then obtained after fitting the data to a linear regression model.

The optimized workflow successfully detected TG at concentrations below 1 µg/mL in human serum, demonstrating the ability of the method to quantify relatively low-abundance protein biomarkers within a complex biological matrix. Although the achieved limit of quantitation remained higher than those typically reported for dedicated triple quadrupole-based clinical assays, the results nevertheless demonstrate the feasibility of performing targeted protein quantitation using a streamlined QTOF-based MRM workflow. Importantly, these findings highlight the potential of high-resolution mass spectrometry to combine peptide confirmation and quantitative analysis within a single platform, providing a flexible alternative for targeted clinical proteomics applications where assay speed and analytical specificity are important considerations.

4.5. Conclusion

This chapter described the development of a simplified and robust targeted LC-MS workflow for the quantitative analysis of clinically relevant protein biomarkers. The method integrated optimized protein denaturation and digestion, SPE clean-up, rapid chromatographic separation, and MRM-HR analysis into a streamlined bottom-up proteomics workflow designed with future clinical implementation in mind.

Using bovine serum albumin as a model protein, key sample preparation and analytical parameters were systematically optimized before the workflow was applied to the quantitation of human albumin and thyroglobulin in serum matrices. The resulting calibration curves demonstrated excellent linearity and reproducibility, supporting the suitability of the method for targeted protein biomarker quantitation.

Although the analytical sensitivity achieved using the QTOF platform was lower than that typically attainable with dedicated triple quadrupole instruments and peptide enrichment strategies, the workflow nonetheless demonstrated the feasibility of performing targeted protein quantitation using a simplified, high-throughput LC-MS approach.

Importantly, this chapter complements the overall theme of the thesis by demonstrating the application of mass spectrometry for quantitative protein analysis, alongside the structural characterization studies presented in earlier chapters. Collectively, the work presented in this thesis highlights the versatility of mass spectrometry as a powerful platform for both the characterization and quantitation of proteins across a broad range of biological and clinical applications.

CHAPTER 5

Conclusion and Future Work

5.1. Conclusions

The work presented in this thesis demonstrates the versatility of mass spectrometry for investigating proteins across multiple levels of structural and analytical complexity. Through the application of hydrogen-deuterium exchange mass spectrometry (HDX-MS), millisecond time-resolved HDX-MS methodologies, and targeted LC-MS workflows, this research illustrates how modern mass spectrometry can provide insights into protein structure, conformational dynamics, and quantitative biomarker analysis.

Chapter 1 introduced the fundamental principles underlying protein mass spectrometry and HDX-MS, including the mechanisms governing hydrogen-deuterium exchange, data acquisition, and experimental design. These concepts provide the foundation for understanding how protein structure and dynamics can be investigated under near-native solution conditions.

In Chapter 2, HDX-MS was used to characterize the structural effects of disease-associated STAT5B mutations. The results demonstrated that these mutations primarily influence localized conformational dynamics rather than inducing large-scale structural rearrangements. Gain-of-function mutations produced distinct stabilization patterns that converged on the pY+3 binding pocket within the SH2 domain, consistent with stabilization of an active-like state. In contrast, the loss-of-function mutation destabilized regions associated with dimerization and signalling. These findings establish the SH2 domain as a key regulatory hotspot within STAT5B and highlight the ability of HDX-MS to reveal mutation-specific structural phenotypes that are not readily apparent from static structural models.

Chapter 3 extended these studies to the intrinsically disordered protein Tau. Using CFI-TRESI-HDX-MS, the effects of kinase-specific phosphorylation on Tau conformational dynamics were examined. Distinct structural signatures were observed depending on the kinase involved, with GSK3β and MARK4 promoting destabilization of the aggregation-prone hexapeptide II region, while Fyn kinase induced localized stabilization. These findings provide further insight into the structural consequences of tau phosphorylation and demonstrate the utility of millisecond HDX-MS for studying highly dynamic protein systems. Additionally, this work contributed to the development of an automated and higher-throughput workflow for investigating disordered proteins and transient conformational states.

Finally, Chapter 4 demonstrated the application of mass spectrometry to quantitative clinical proteomics through the development of a targeted LC-MS workflow for protein biomarker quantitation. The resulting method combined streamlined sample preparation, rapid chromatographic separation, and MRM analysis to enable reproducible quantitation of clinically relevant proteins in serum. This work highlights the growing role of LC-MS-based methods in clinical laboratories, where improved analytical specificity and multiplexing capabilities offer important advantages over traditional immunoassays.

Collectively, the studies presented in this thesis demonstrate the depth of biological information accessible through mass spectrometry. From elucidating mutation-induced conformational changes and phosphorylation-dependent structural dynamics to enabling quantitative biomarker measurements, mass spectrometry provides a powerful and versatile platform for addressing complex biological and clinical questions. More broadly, this work reinforces the importance of protein structural dynamics in regulating biological function and disease, while highlighting the continuing impact of mass spectrometry in structural biology, translational research, and clinical diagnostics.

5.2 Limitations and Future Directions

While the studies presented in this dissertation provide new insights into protein conformational dynamics and quantitative protein analysis using mass spectrometry, several limitations remain that present opportunities for future investigation.

Hydrogen-deuterium exchange mass spectrometry has become a powerful tool for probing protein structure and conformational dynamics under near-native conditions; however, its spatial resolution remains limited in conventional bottom-up workflows, where deuterium incorporation is averaged across proteolytic peptides. As a result, localized structural perturbations cannot always be assigned to individual amino acid residues. While the conformational consequences of disease-associated STAT5B mutations and tau phosphorylation events were successfully characterized in this work, recent advances in electron capture dissociation (ECD)-based HDX-MS have demonstrated the ability to localize differential deuterium uptake at near residue-level resolution.[122] Applying these approaches to the STAT5B and tau systems examined herein could provide deeper insight into the specific regions affected by mutation, phosphorylation, and ligand binding, thereby improving mechanistic understanding of these biologically relevant processes.

The millisecond HDX-MS experiments described in this thesis further highlight both the strengths and current limitations of rapid-exchange methodologies. The continuous-flow TRESI platform enables characterization of highly dynamic proteins and transient conformational states that are often inaccessible using conventional HDX-MS timescales. However, acquisition of different labeling times currently requires manual adjustment of capillary positions for each exchange point. This process can be time-consuming and introduces potential variability between experiments. Future development of fully automated TRESI instrumentation capable of software-controlled adjustment of reaction volumes and mixing distances would improve reproducibility, increase throughput, and facilitate the collection of more comprehensive kinetic datasets. Such developments would be particularly valuable for studying intrinsically disordered proteins and other rapidly exchanging systems.

The biological systems examined in this dissertation also provide several avenues for future study. For STAT5B, the mutations investigated were examined individually to isolate their structural effects. However, disease progression frequently involves the accumulation of multiple genetic alterations. Future HDX-MS studies examining combinations of disease-associated mutations within a single construct may reveal cooperative effects on protein stability, allosteric effects, and activation that cannot be observed through analysis of individual variants alone. Such studies may provide a more complete understanding of the molecular mechanisms underlying STAT5B-driven disease.

Similarly, the tau phosphorylation states characterized in this work represent only a subset of the post-translational modifications observed in neurodegenerative disorders. Pathological tau contains numerous phosphorylation sites that accumulate throughout disease progression and contribute to aggregation and neurofibrillary tangle formation. Future studies should therefore focus on more disease-relevant hyperphosphorylated tau species containing multiple phosphorylation events. Characterization of these conformational states may improve understanding of the structural transitions that precede aggregation and may aid the development of therapeutics designed to selectively target aggregation-prone conformations.

Beyond structural biology, the quantitative LC-MS workflow developed in Chapter 4 demonstrates the growing utility of mass spectrometry for clinical protein analysis. While the targeted assays developed here successfully quantified clinically relevant proteins, future work should focus on expanding these methods toward larger multiplexed biomarker panels capable of simultaneously monitoring numerous proteins from a single patient sample. Such approaches offer several advantages over conventional immunoassays, including improved analytical specificity, reduced susceptibility to antibody-related interferences, and greater flexibility for multiplexed measurements. Continued advances in sample preparation, automation, instrument sensitivity, and data analysis are expected to further accelerate the adoption of LC-MS-based assays within clinical laboratories and precision medicine workflows.

Collectively, these limitations and future directions highlight the continued evolution of mass spectrometry as both a structural biology and analytical platform. Advances in automation, instrumentation, and analytical methodologies are already and will continue to expand the scope of HDX-MS and quantitative proteomics, enabling increasingly detailed characterization of protein structure, dynamics, and abundance in complex biological and clinical systems.

Reference

(1) Hu, Y.; Cheng, K.; He, L.; Zhang, X.; Jiang, B.; Jiang, L.; Li, C.; Wang, G.; Yang, Y.; Liu, M. NMR-Based Methods for Protein Analysis. *Anal. Chem.* **2021**, *93* (4), 1866–1879. https://doi.org/10.1021/acs.analchem.0c03830.

(2) Carroni, M.; Saibil, H. R. Cryo Electron Microscopy to Determine the Structure of Macromolecular Complexes. *Methods* **2016**, *95*, 78–85. https://doi.org/10.1016/j.ymeth.2015.11.023.

(3) Smyth, M. S.; Martin, J. H. J. *X* Ray Crystallography. *Mol Path* **2000**, *53* (1), 8–14. https://doi.org/10.1136/mp.53.1.8.

(4) Mukrasch, M. D.; Bibow, S.; Korukottu, J.; Jeganathan, S.; Biernat, J.; Griesinger, C.; Mandelkow, E.; Zweckstetter, M. Structural Polymorphism of 441-Residue Tau at Single Residue Resolution. *PLoS Biol* **2009**, *7* (2), e1000034. https://doi.org/10.1371/journal.pbio.1000034.

(5) Ozenne, V.; Schneider, R.; Yao, M.; Huang, J.; Salmon, L.; Zweckstetter, M.; Jensen, M. R.; Blackledge, M. Mapping the Potential Energy Landscape of Intrinsically Disordered Proteins at Amino Acid Resolution. *J. Am. Chem. Soc.* **2012**, *134* (36), 15138–15148. https://doi.org/10.1021/ja306905s.

(6) Kragelj, J.; Ozenne, V.; Blackledge, M.; Jensen, M. R. Conformational Propensities of Intrinsically Disordered Proteins from NMR Chemical Shifts. *ChemPhysChem* **2013**, *14* (13), 3034–3045. https://doi.org/10.1002/cphc.201300387.

(7) Piersimoni, L.; Kastritis, P. L.; Arlt, C.; Sinz, A. Cross-Linking Mass Spectrometry for Investigating Protein Conformations and Protein–Protein Interactions–A Method for All Seasons. *Chem. Rev.* **2022**, *122* (8), 7500–7531. https://doi.org/10.1021/acs.chemrev.1c00786.

(8) Narang, D.; Lento, C.; J. Wilson, D. HDX-MS: An Analytical Tool to Capture Protein Motion in Action. *Biomedicines* **2020**, *8* (7), 224. https://doi.org/10.3390/biomedicines8070224.

(9) Griffiths, J. A Brief History of Mass Spectrometry. *Anal. Chem.* **2008**, *80* (15), 5678–5683. https://doi.org/10.1021/ac8013065.

(10) Downard, K. M. Francis William Aston: The Man Behind the Mass Spectrograph. *Eur J Mass Spectrom (Chichester)* **2007**, *13* (3), 177–190. https://doi.org/10.1255/ejms.878.

(11) Dempster, A. J. A New Method of Positive Ray Analysis. *Phys. Rev.* **1918**, *11* (4), 316–325. https://doi.org/10.1103/PhysRev.11.316.

(12) Karas, Michael.; Hillenkamp, Franz. Laser Desorption Ionization of Proteins with Molecular Masses Exceeding 10,000 Daltons. *Anal. Chem.* **1988**, *60* (20), 2299–2301. https://doi.org/10.1021/ac00171a028.

(13) Carr, S. A.; Annan, R. S. Overview of Peptide and Protein Analysis by Mass Spectrometry. *CP Protein Science* **1996**, *4* (1). https://doi.org/10.1002/0471140864.ps1601s04.

(14) Tanaka, M.; Iijima, Y.; Masuda, Y.; Sato, T.; Mineta, T. Adjustment Method of MEMS Dual-Cantilever Deflection Using Plastic Deformation of Al and Ni Thin Film by Thermal Annealing. *Electronics* **2023**, *12* (14), 3153. https://doi.org/10.3390/electronics12143153.

(15) Vinciauskaite, V.; Masson, G. R. Fundamentals of HDX-MS. *Essays in Biochemistry* **2023**, *67* (2), 301–314. https://doi.org/10.1042/EBC20220111.

(16) Morris, H. R.; Paxton, T.; Panico, M.; McDowell, R.; Dell, A. A Novel Geometry Mass Spectrometer, the Q-TOF, for Low-Femtomole/Attomole-Range Biopolymer Sequencing. *J Protein Chem* **1997**, *16* (5), 469–479. https://doi.org/10.1023/A:1026309410737.
(17) Konermann, L.; Ahadi, E.; Rodriguez, A. D.; Vahidi, S. Unraveling the Mechanism of Electrospray Ionization. *Anal. Chem.* **2013**, *85* (1), 2–9. https://doi.org/10.1021/ac302789c.
(18) Meher, A. K.; Chen, Y.-C. Electrospray Modifications for Advancing Mass Spectrometric Analysis. *Mass Spectrometry* **2017**, *6* (2), S0057–S0057. https://doi.org/10.5702/massspectrometry.S0057.
(19) Kristensen, D. B.; Imamura, K.; Miyamoto, Y.; Yoshizato, K. Mass Spectrometric Approaches for the Characterization of Proteins on a Hybrid Quadrupole Time-of-Flight (Q-TOF) Mass Spectrometer. *Electrophoresis* **2000**, *21* (2), 430–439. https://doi.org/10.1002/(SICI)1522-2683(20000101)21:2%3C430::AID-ELPS430%3E3.0.CO;2-0.
(20) Roepstorff, P. Mass Spectrometry in Protein Studies from Genome to Function. *Current Opinion in Biotechnology* **1997**, *8* (1), 6–13. https://doi.org/10.1016/S0958-1669(97)80151-6.
(21) Chernushevich, I. V.; Loboda, A. V.; Thomson, B. A. An Introduction to Quadrupole–Time-of-flight Mass Spectrometry. *J. Mass Spectrom.* **2001**, *36* (8), 849–865. https://doi.org/10.1002/jms.207.
(22) Waters Corporation. *TriWave – More Complete Characterization of Mixtures and Molecules*; White Paper; White Paper Library Number: LITR134678884; Waters Corporation: Milford, MA, 2012. https://www.waters.com/webassets/cms/library/docs/720004176en.pdf.
(23) Kelly, R. T.; Tolmachev, A. V.; Page, J. S.; Tang, K.; Smith, R. D. The Ion Funnel: Theory, Implementations, and Applications. *Mass Spectrometry Reviews* **2010**, *29* (2), 294–312. https://doi.org/10.1002/mas.20232.
(24) Giles, K.; Pringle, S. D.; Worthington, K. R.; Little, D.; Wildgoose, J. L.; Bateman, R. H. Applications of a Travelling Wave-based Radio-frequency-only Stacked Ring Ion Guide. *Rapid Comm Mass Spectrometry* **2004**, *18* (20), 2401–2414. https://doi.org/10.1002/rcm.1641.
(25) Maher, S.; Jjunju, F. P. M.; Taylor, S. *Colloquium* : 100 Years of Mass Spectrometry: Perspectives and Future Trends. *Rev. Mod. Phys.* **2015**, *87* (1), 113–135. https://doi.org/10.1103/RevModPhys.87.113.
(26) Viehland, L. A.; Mason, E. A. Gaseous Lon Mobility in Electric Fields of Arbitrary Strength. *Annals of Physics* **1975**, *91* (2), 499–533. https://doi.org/10.1016/0003-4916(75)90233-X.
(27) Dodds, J. N.; Baker, E. S. Ion Mobility Spectrometry: Fundamental Concepts, Instrumentation, Applications, and the Road Ahead. *J. Am. Soc. Mass Spectrom.* **2019**, *30* (11), 2185–2195. https://doi.org/10.1007/s13361-019-02288-2.
(28) Revercomb, H. E.; Mason, E. A. Theory of Plasma Chromatography/Gaseous Electrophoresis. Review. *Anal. Chem.* **1975**, *47* (7), 970–983. https://doi.org/10.1021/ac60357a043.
(29) May, J. C.; Goodwin, C. R.; Lareau, N. M.; Leaptrot, K. L.; Morris, C. B.; Kurulugama, R. T.; Mordehai, A.; Klein, C.; Barry, W.; Darland, E.; Overney, G.; Imatani, K.; Stafford, G. C.; Fjeldsted, J. C.; McLean, J. A. Conformational Ordering of Biomolecules in the Gas Phase: Nitrogen Collision Cross Sections Measured on a Prototype High Resolution Drift Tube Ion Mobility-Mass Spectrometer. *Anal. Chem.* **2014**, *86* (4), 2107–2116. https://doi.org/10.1021/ac4038448.
(30) Charles, L.; Chendo, C.; Poyer, S. Ion Mobility Spectrometry – Mass Spectrometry Coupling for Synthetic Polymers. *Rapid Comm Mass Spectrometry* **2020**, *34* (S2), e8624. https://doi.org/10.1002/rcm.8624.

(31) Morsa, D.; Gabelica, V.; De Pauw, E. Fragmentation and Isomerization Due to Field Heating in Traveling Wave Ion Mobility Spectrometry. *J. Am. Soc. Mass Spectrom.* **2014**, *25* (8), 1384–1393. https://doi.org/10.1007/s13361-014-0909-9.
(32) Hamid, Z.; Armirotti, A. Traveling Wave Ion Mobility-Mass Spectrometry to Enhance the Detection of Low Abundance Features in Untargeted Lipidomics. In *Ion Mobility-Mass Spectrometry*; Paglia, G., Astarita, G., Eds.; Methods in Molecular Biology; Springer US: New York, NY, 2020; Vol. 2084, pp 103–117. https://doi.org/10.1007/978-1-0716-0030-6_6.
(33) Smith, D. P.; Knapman, T. W.; Campuzano, I.; Malham, R. W.; Berryman, J. T.; Radford, S. E.; Ashcroft, A. E. Deciphering Drift Time Measurements from Travelling Wave Ion Mobility Spectrometry-Mass Spectrometry Studies. *Eur J Mass Spectrom (Chichester)* **2009**, *15* (2), 113–130. https://doi.org/10.1255/ejms.947.
(34) Pringle, S. D.; Giles, K.; Wildgoose, J. L.; Williams, J. P.; Slade, S. E.; Thalassinos, K.; Bateman, R. H.; Bowers, M. T.; Scrivens, J. H. An Investigation of the Mobility Separation of Some Peptide and Protein Ions Using a New Hybrid Quadrupole/Travelling Wave IMS/Oa-ToF Instrument. *International Journal of Mass Spectrometry* **2007**, *261* (1), 1–12. https://doi.org/10.1016/j.ijms.2006.07.021.
(35) Knapman, T. W.; Berryman, J. T.; Campuzano, I.; Harris, S. A.; Ashcroft, A. E. Considerations in Experimental and Theoretical Collision Cross-Section Measurements of Small Molecules Using Travelling Wave Ion Mobility Spectrometry-Mass Spectrometry. *International Journal of Mass Spectrometry* **2010**, *298* (1–3), 17–23. https://doi.org/10.1016/j.ijms.2009.09.011.
(36) Riches, E.; Palmer, M. E. Application of a Novel Cyclic Ion Mobility-mass Spectrometer to the Analysis of Synthetic Polymers: A Preliminary Evaluation. *Rapid Comm Mass Spectrometry* **2020**, *34* (S2), e8710. https://doi.org/10.1002/rcm.8710.
(37) Giles, K.; Ujma, J.; Wildgoose, J.; Pringle, S.; Richardson, K.; Langridge, D.; Green, M. A Cyclic Ion Mobility-Mass Spectrometry System. *Anal. Chem.* **2019**, *91* (13), 8564–8573. https://doi.org/10.1021/acs.analchem.9b01838.
(38) Morsa, D.; Gabelica, V.; De Pauw, E. Effective Temperature of Ions in Traveling Wave Ion Mobility Spectrometry. *Anal. Chem.* **2011**, *83* (14), 5775–5782. https://doi.org/10.1021/ac201509p.
(39) Michelmann, K.; Silveira, J. A.; Ridgeway, M. E.; Park, M. A. Fundamentals of Trapped Ion Mobility Spectrometry. *J. Am. Soc. Mass Spectrom.* **2015**, *26* (1), 14–24. https://doi.org/10.1007/s13361-014-0999-4.
(40) Swearingen, K. E.; Moritz, R. L. High-Field Asymmetric Waveform Ion Mobility Spectrometry for Mass Spectrometry-Based Proteomics. *Expert Review of Proteomics* **2012**, *9* (5), 505–517. https://doi.org/10.1586/epr.12.50.
(41) Hjernø, K.; Højrup, P. Interpretation of Tandem Mass Spectrometry (MSMS) Spectra for Peptide Analysis. In *Peptide Antibodies*; Houen, G., Ed.; Methods in Molecular Biology; Springer New York: New York, NY, 2015; Vol. 1348, pp 83–102. https://doi.org/10.1007/978-1-4939-2999-3_10.
(42) Boyd, R.; Somogyi, Á. The Mobile Proton Hypothesis in Fragmentation of Protonated Peptides: A Perspective. *J. Am. Soc. Mass Spectrom.* **2010**, *21* (8), 1275–1278. https://doi.org/10.1016/j.jasms.2010.04.017.
(43) Smith, D. L.; Deng, Y.; Zhang, Z. Probing the Non-Covalent Structure of Proteins by Amide Hydrogen Exchange and Mass Spectrometry. *J. Mass Spectrom.* **1997**, *32* (2), 135–146. https://doi.org/10.1002/(SICI)1096-9888(199702)32:2%3C135::AID-JMS486%3E3.0.CO;2-M.

(44) Molday, R. S.; Englander, S. W.; Kallen, R. G. Primary Structure Effects on Peptide Group Hydrogen Exchange. *Biochemistry* **1972**, *11* (2), 150–158. https://doi.org/10.1021/bi00752a003.
(45) Bai, Y.; Milne, J. S.; Mayne, L.; Englander, S. W. Primary Structure Effects on Peptide Group Hydrogen Exchange. *Proteins* **1993**, *17* (1), 75–86. https://doi.org/10.1002/prot.340170110.
(46) Qian, H.; Chan, S. I. Hydrogen Exchange Kinetics of Proteins in Denaturants: A Generalized Two-Process Model † †Dedicated to Dr Andrew Morton, Who Tragically Passed Away on July 17, 1998, for the Living Memory of Many Long Discussions on Hydrogen Exchange Kinetics and Protein Folding Intermediates. 1 1Edited by P. E. Wright. *Journal of Molecular Biology* **1999**, *286* (2), 607–616. https://doi.org/10.1006/jmbi.1998.2484.
(47) Englander, J. J.; Del Mar, C.; Li, W.; Englander, S. W.; Kim, J. S.; Stranz, D. D.; Hamuro, Y.; Woods, V. L. Protein Structure Change Studied by Hydrogen-Deuterium Exchange, Functional Labeling, and Mass Spectrometry. *Proc. Natl. Acad. Sci. U.S.A.* **2003**, *100* (12), 7057–7062. https://doi.org/10.1073/pnas.1232301100.
(48) Zhang, Z.; Smith, D. L. Determination of Amide Hydrogen Exchange by Mass Spectrometry: A New Tool for Protein Structure Elucidation. *Protein Science* **1993**, *2* (4), 522–531. https://doi.org/10.1002/pro.5560020404.
(49) Nguyen, D.; Mayne, L.; Phillips, M. C.; Walter Englander, S. Reference Parameters for Protein Hydrogen Exchange Rates. *J. Am. Soc. Mass Spectrom.* **2018**, *29* (9), 1936–1939. https://doi.org/10.1007/s13361-018-2021-z.
(50) Connelly, G. P.; Bai, Y.; Jeng, M.; Englander, S. W. Isotope Effects in Peptide Group Hydrogen Exchange. *Proteins* **1993**, *17* (1), 87–92. https://doi.org/10.1002/prot.340170111.
(51) Keppel, T. R.; Howard, B. A.; Weis, D. D. Mapping Unstructured Regions and Synergistic Folding in Intrinsically Disordered Proteins with Amide H/D Exchange Mass Spectrometry. *Biochemistry* **2011**, *50* (40), 8722–8732. https://doi.org/10.1021/bi200875p.
(52) Zhu, S.; Shala, A.; Bezginov, A.; Sljoka, A.; Audette, G.; Wilson, D. J. Hyperphosphorylation of Intrinsically Disordered Tau Protein Induces an Amyloidogenic Shift in Its Conformational Ensemble. *PLoS ONE* **2015**, *10* (3), e0120416. https://doi.org/10.1371/journal.pone.0120416.
(53) Masson, G. R.; Burke, J. E.; Ahn, N. G.; Anand, G. S.; Borchers, C.; Brier, S.; Bou-Assaf, G. M.; Engen, J. R.; Englander, S. W.; Faber, J.; Garlish, R.; Griffin, P. R.; Gross, M. L.; Guttman, M.; Hamuro, Y.; Heck, A. J. R.; Houde, D.; Iacob, R. E.; Jørgensen, T. J. D.; Kaltashov, I. A.; Klinman, J. P.; Konermann, L.; Man, P.; Mayne, L.; Pascal, B. D.; Reichmann, D.; Skehel, M.; Snijder, J.; Strutzenberg, T. S.; Underbakke, E. S.; Wagner, C.; Wales, T. E.; Walters, B. T.; Weis, D. D.; Wilson, D. J.; Wintrode, P. L.; Zhang, Z.; Zheng, J.; Schriemer, D. C.; Rand, K. D. Recommendations for Performing, Interpreting and Reporting Hydrogen Deuterium Exchange Mass Spectrometry (HDX-MS) Experiments. *Nat Methods* **2019**, *16* (7), 595–602. https://doi.org/10.1038/s41592-019-0459-y.
(54) Karch, K. R.; Coradin, M.; Zandarashvili, L.; Kan, Z.-Y.; Gerace, M.; Englander, S. W.; Black, B. E.; Garcia, B. A. Hydrogen-Deuterium Exchange Coupled to Top- and Middle-Down Mass Spectrometry Reveals Histone Tail Dynamics before and after Nucleosome Assembly. *Structure* **2018**, *26* (12), 1651-1663.e3. https://doi.org/10.1016/j.str.2018.08.006.
(55) Langford, J. B.; Ahmed, E.; Fang, M.; Cupp-Sutton, K.; Smith, K.; Wu, S. Strategies for Top–Down Hydrogen Deuterium Exchange-Mass Spectrometry: A Mini Review and Perspective. *J Mass Spectrom* **2024**, *59* (11), e5097. https://doi.org/10.1002/jms.5097.

(56) Rob, T.; Liuni, P.; Gill, P. K.; Zhu, S.; Balachandran, N.; Berti, P. J.; Wilson, D. J. Measuring Dynamics in Weakly Structured Regions of Proteins Using Microfluidics-Enabled Subsecond H/D Exchange Mass Spectrometry. *Anal. Chem.* **2012**, *84* (8), 3771–3779. https://doi.org/10.1021/ac300365u.
(57) Konermann, L.; Pan, J.; Wilson, D. J. Protein Folding Mechanisms Studied by Time-Resolved Electrospray Mass Spectrometry. *BioTechniques* **2006**, *40* (2), 135–141. https://doi.org/10.2144/06402TE01.
(58) Anacleto, J.; Lento, C.; Sarpe, V.; Maqsood, A.; Mehrazma, B.; Schriemer, D.; Wilson, D. J. Apparatus for Automated Continuous Hydrogen Deuterium Exchange Mass Spectrometry Measurements from Milliseconds to Hours. *Anal. Chem.* **2023**, *95* (9), 4421–4428. https://doi.org/10.1021/acs.analchem.2c05003.
(59) Wales, T. E.; Engen, J. R. Hydrogen Exchange Mass Spectrometry for the Analysis of Protein Dynamics. *Mass Spectrometry Reviews* **2006**, *25* (1), 158–170. https://doi.org/10.1002/mas.20064.
(60) Hoofnagle, A. N.; Resing, K. A.; Ahn, N. G. Practical Methods for Deuterium Exchange/Mass Spectrometry. In *MAP Kinase Signaling Protocols*; Humana Press: New Jersey, 2004; Vol. 0, pp 283–298. https://doi.org/10.1385/1-59259-671-1:283.
(61) Verhoeven, Y.; Tilborghs, S.; Jacobs, J.; De Waele, J.; Quatannens, D.; Deben, C.; Prenen, H.; Pauwels, P.; Trinh, X. B.; Wouters, A.; Smits, E. L. J.; Lardon, F.; Van Dam, P. A. The Potential and Controversy of Targeting STAT Family Members in Cancer. *Seminars in Cancer Biology* **2020**, *60*, 41–56. https://doi.org/10.1016/j.semcancer.2019.10.002.
(62) Hu, X.; Li, J.; Fu, M.; Zhao, X.; Wang, W. The JAK/STAT Signaling Pathway: From Bench to Clinic. *Sig Transduct Target Ther* **2021**, *6* (1), 402. https://doi.org/10.1038/s41392-021-00791-1.
(63) Awasthi, N.; Liongue, C.; Ward, A. C. STAT Proteins: A Kaleidoscope of Canonical and Non-Canonical Functions in Immunity and Cancer. *J Hematol Oncol* **2021**, *14* (1), 198. https://doi.org/10.1186/s13045-021-01214-y.
(64) Levy, D. E.; Darnell, J. E. STATs: Transcriptional Control and Biological Impact. *Nat Rev Mol Cell Biol* **2002**, *3* (9), 651–662. https://doi.org/10.1038/nrm909.
(65) Philips, R. L.; Wang, Y.; Cheon, H.; Kanno, Y.; Gadina, M.; Sartorelli, V.; Horvath, C. M.; Darnell, J. E.; Stark, G. R.; O'Shea, J. J. The JAK-STAT Pathway at 30: Much Learned, Much More to Do. *Cell* **2022**, *185* (21), 3857–3876. https://doi.org/10.1016/j.cell.2022.09.023.
(66) Xue, C.; Yao, Q.; Gu, X.; Shi, Q.; Yuan, X.; Chu, Q.; Bao, Z.; Lu, J.; Li, L. Evolving Cognition of the JAK-STAT Signaling Pathway: Autoimmune Disorders and Cancer. *Sig Transduct Target Ther* **2023**, *8* (1), 204. https://doi.org/10.1038/s41392-023-01468-7.
(67) De Araujo, E. D.; Erdogan, F.; Neubauer, H. A.; Meneksedag-Erol, D.; Manaswiyoungkul, P.; Eram, M. S.; Seo, H.-S.; Qadree, A. K.; Israelian, J.; Orlova, A.; Suske, T.; Pham, H. T. T.; Boersma, A.; Tangermann, S.; Kenner, L.; Rülicke, T.; Dong, A.; Ravichandran, M.; Brown, P. J.; Audette, G. F.; Rauscher, S.; Dhe-Paganon, S.; Moriggl, R.; Gunning, P. T. Structural and Functional Consequences of the STAT5BN642H Driver Mutation. *Nat Commun* **2019**, *10* (1), 2517. https://doi.org/10.1038/s41467-019-10422-7.
(68) Lin, J.; Buettner, R.; Yuan, Y.-C.; Yip, R.; Horne, D.; Jove, R.; Vaidehi, N. Molecular Dynamics Simulations of the Conformational Changes in Signal Transducers and Activators of Transcription, Stat1 and Stat3. *Journal of Molecular Graphics and Modelling* **2009**, *28* (4), 347–356. https://doi.org/10.1016/j.jmgm.2009.08.013.
(69) De Araujo, E. D.; Orlova, A.; Neubauer, H. A.; Bajusz, D.; Seo, H.-S.; Dhe-Paganon, S.; Keserű, G. M.; Moriggl, R.; Gunning, P. T. Structural Implications of STAT3 and STAT5 SH2 Domain Mutations. *Cancers* **2019**, *11* (11), 1757. https://doi.org/10.3390/cancers11111757.

(70) Bhattacharya, D.; Teramo, A.; Gasparini, V. R.; Huuhtanen, J.; Kim, D.; Theodoropoulos, J.; Schiavoni, G.; Barilà, G.; Vicenzetto, C.; Calabretto, G.; Facco, M.; Kawakami, T.; Nakazawa, H.; Falini, B.; Tiacci, E.; Ishida, F.; Semenzato, G.; Kelkka, T.; Zambello, R.; Mustjoki, S. Identification of Novel STAT5B Mutations and Characterization of TCRβ Signatures in CD4+ T-Cell Large Granular Lymphocyte Leukemia. *Blood Cancer J.* **2022**, *12* (2), 31. https://doi.org/10.1038/s41408-022-00630-8.
(71) Keating, A. How Do Mesenchymal Stromal Cells Suppress T Cells? *Cell Stem Cell* **2008**, *2* (2), 106–108. https://doi.org/10.1016/j.stem.2008.01.007.
(72) Hennighausen, L.; Robinson, G. W. Interpretation of Cytokine Signaling through the Transcription Factors STAT5A and STAT5B. *Genes Dev.* **2008**, *22* (6), 711–721. https://doi.org/10.1101/gad.1643908.
(73) Haas-Neill, L.; Meneksedag-Erol, D.; Chaudhry, A.; Novoselova, M.; Ashraf, Q. F.; De Araujo, E. D.; Wilson, D. J.; Rauscher, S. The Structural Influence of the Oncogenic Driver Mutation N642H in the STAT5B SH2 Domain. *Protein Science* **2025**, *34* (1), e70022. https://doi.org/10.1002/pro.70022.
(74) Küçük, C.; Jiang, B.; Hu, X.; Zhang, W.; Chan, J. K. C.; Xiao, W.; Lack, N.; Alkan, C.; Williams, J. C.; Avery, K. N.; Kavak, P.; Scuto, A.; Sen, E.; Gaulard, P.; Staudt, L.; Iqbal, J.; Zhang, W.; Cornish, A.; Gong, Q.; Yang, Q.; Sun, H.; d'Amore, F.; Leppä, S.; Liu, W.; Fu, K.; De Leval, L.; McKeithan, T.; Chan, W. C. Activating Mutations of STAT5B and STAT3 in Lymphomas Derived from Γδ-T or NK Cells. *Nat Commun* **2015**, *6* (1), 6025. https://doi.org/10.1038/ncomms7025.
(75) Heppler, L. N.; Frank, D. A. Rare Mutations Provide Unique Insight into Oncogenic Potential of STAT Transcription Factors. *Journal of Clinical Investigation* **2017**, *128* (1), 113–115. https://doi.org/10.1172/JCI98619.
(76) Rajala, H. L. M.; Eldfors, S.; Kuusanmäki, H.; Van Adrichem, A. J.; Olson, T.; Lagström, S.; Andersson, E. I.; Jerez, A.; Clemente, M. J.; Yan, Y.; Zhang, D.; Awwad, A.; Ellonen, P.; Kallioniemi, O.; Wennerberg, K.; Porkka, K.; Maciejewski, J. P.; Loughran, T. P.; Heckman, C.; Mustjoki, S. Discovery of Somatic STAT5b Mutations in Large Granular Lymphocytic Leukemia. *Blood* **2013**, *121* (22), 4541–4550. https://doi.org/10.1182/blood-2012-12-474577.
(77) Kontro, M.; Kuusanmäki, H.; Eldfors, S.; Burmeister, T.; Andersson, E. I.; Bruserud, Ø.; Brümmendorf, T. H.; Edgren, H.; Gjertsen, B. T.; Itälä-Remes, M.; Lagström, S.; Lohi, O.; Lundán, T.; Martí, J. M. L.; Majumder, M. M.; Parsons, A.; Pemovska, T.; Rajala, H.; Vettenranta, K.; Kallioniemi, O.; Mustjoki, S.; Porkka, K.; Heckman, C. A. Novel Activating STAT5B Mutations as Putative Drivers of T-Cell Acute Lymphoblastic Leukemia. *Leukemia* **2014**, *28* (8), 1738–1742. https://doi.org/10.1038/leu.2014.89.
(78) Jin, Y.; Purohit, S.; Chen, X.; Yi, B.; She, J.-X. Over-Expression of Stat5b Confers Protection against Diabetes in the Non-Obese Diabetic (NOD) Mice via up-Regulation of CD4+CD25+ Regulatory T Cells. *Biochemical and Biophysical Research Communications* **2012**, *424* (4), 669–674. https://doi.org/10.1016/j.bbrc.2012.06.162.
(79) Li, J.; Rodriguez, J. P.; Niu, F.; Pu, M.; Wang, J.; Hung, L.-W.; Shao, Q.; Zhu, Y.; Ding, W.; Liu, Y.; Da, Y.; Yao, Z.; Yang, J.; Zhao, Y.; Wei, G.-H.; Cheng, G.; Liu, Z.-J.; Ouyang, S. Structural Basis for DNA Recognition by STAT6. *Proc. Natl. Acad. Sci. U.S.A.* **2016**, *113* (46), 13015–13020. https://doi.org/10.1073/pnas.1611228113.
(80) Moriggl, R.; Berchtold, S.; Friedrich, K.; Standke, G. J. R.; Kammer, W.; Heim, M.; Wissler, M.; Stöcklin, E.; Gouilleux, F.; Groner, B. Comparison of the Transactivation Domains of Stat5 and Stat6 in Lymphoid Cells and Mammary Epithelial Cells. *Mol Cell Biol* **1997**, *17* (7), 3663–3678. https://doi.org/10.1128/MCB.17.7.3663.

(81) Lee, H. K.; Chen, J.; Philips, R. L.; Lee, S.-G.; Feng, X.; Wu, Z.; Liu, C.; Schultz, A. B.; Dalzell, M.; Meggendorfer, M.; Haferlach, C.; Birnbaum, F.; Sexton, J. A.; Keating, A. E.; O'Shea, J. J.; Young, N. S.; Villarino, A. V.; Furth, P. A.; Hennighausen, L. STAT5B Leukemic Mutations, Altering SH2 Tyrosine 665, Have Opposing Impacts on Immune Gene Programs. *Life Sci. Alliance* **2025**, *8* (7), e202503222. https://doi.org/10.26508/lsa.202503222.
(82) De Araujo, E. D.; Geletu, M.; Gunning, P. T. Strategies for Over-Expression and Purification of Recombinant Full Length STAT5B in Escherichia Coli. *Protein Expression and Purification* **2017**, *129*, 1–8. https://doi.org/10.1016/j.pep.2016.08.017.
(83) Winkler, R. ESIprot: A Universal Tool for Charge State Determination and Molecular Weight Calculation of Proteins from Electrospray Ionization Mass Spectrometry Data. *Rapid Comm Mass Spectrometry* **2010**, *24* (3), 285–294. https://doi.org/10.1002/rcm.4384.
(84) Rey, M.; Sarpe, V.; Burns, K. M.; Buse, J.; Baker, C. A. H.; van Dijk, M.; Wordeman, L.; Bonvin, A. M. J. J.; Schriemer, D. C. Mass Spec Studio for Integrative Structural Biology. *Structure* **2014**, *22* (10), 1538–1548. https://doi.org/10.1016/j.str.2014.08.013.
(85) Fahrenkamp, D.; Li, J.; Ernst, S.; Schmitz-Van De Leur, H.; Chatain, N.; Küster, A.; Koschmieder, S.; Lüscher, B.; Rossetti, G.; Müller-Newen, G. Intramolecular Hydrophobic Interactions Are Critical Mediators of STAT5 Dimerization. *Sci Rep* **2016**, *6* (1), 35454. https://doi.org/10.1038/srep35454.
(86) Bajusz, D.; Pándy-Szekeres, G.; Takács, Á.; de Araujo, E. D.; Keserű, G. M. SH2db, an Information System for the SH2 Domain. *Nucleic Acids Research* **2023**, *51* (W1), W542–W552. https://doi.org/10.1093/nar/gkad420.
(87) Seetaloo, N.; Kish, M.; Phillips, J. J. HDfleX : Software for Flexible High Structural Resolution of Hydrogen/Deuterium-Exchange Mass Spectrometry Data. *Anal. Chem.* **2022**, *94* (11), 4557–4564. https://doi.org/10.1021/acs.analchem.1c05339.
(88) Koide, S.; Jahnke, W.; Wright, PeterE. Measurement of Intrinsic Exchange Rates of Amide Protons in a 15N-Labeled Peptide. *J Biomol NMR* **1995**, *6* (3). https://doi.org/10.1007/BF00197811.
(89) Gräb, J.; Berg, A.; Blechschmidt, L.; Klüver, B.; Rubner, S.; Fu, D. Y.; Meiler, J.; Gräber, M.; Berg, T. The STAT5b Linker Domain Mediates the Selectivity of Catechol Bisphosphates for STAT5b over STAT5a. *ACS Chem. Biol.* **2019**, *14* (4), 796–805. https://doi.org/10.1021/acschembio.9b00137.
(90) Giffhorn, F.; Gottschalk, G. Inactivation of Citrate Lyase from Rhodopseudomonas Gelatinosa by a Specific Deacetylase and Inhibition of This Inactivation by L-(+1-Glutamate. *J Bacteriol* **1975**, *124* (3), 1052–1061. https://doi.org/10.1128/jb.124.3.1052-1061.1975.
(91) Koshiba, H. [Comparison of drug effects on the isolated rat colon and duodenum]. *Nihon Yakurigaku Zasshi* **1975**, *71* (5), 415–426.
(92) Buée, L.; Bussière, T.; Buée-Scherrer, V.; Delacourte, A.; Hof, P. R. Tau Protein Isoforms, Phosphorylation and Role in Neurodegenerative disorders11These Authors Contributed Equally to This Work. *Brain Research Reviews* **2000**, *33* (1), 95–130. https://doi.org/10.1016/S0165-0173(00)00019-9.
(93) Brion, J.-P.; Flament-Durand, J.; Dustin, P. ALZHEIMER'S DISEASE AND TAU PROTEINS. *The Lancet* **1986**, *328* (8515), 1098. https://doi.org/10.1016/S0140-6736(86)90495-2.
(94) Samimi, N.; Sharma, G.; Kimura, T.; Matsubara, T.; Huo, A.; Chiba, K.; Saito, Y.; Murayama, S.; Akatsu, H.; Hashizume, Y.; Hasegawa, M.; Farjam, M.; Shahpasand, K.; Ando, K.; Hisanaga, S. Distinct Phosphorylation

Profiles of Tau in Brains of Patients with Different Tauopathies. *Neurobiology of Aging* **2021**, *108*, 72–79. https://doi.org/10.1016/j.neurobiolaging.2021.08.011.
(95) Scheres, S. H.; Zhang, W.; Falcon, B.; Goedert, M. Cryo-EM Structures of Tau Filaments. *Current Opinion in Structural Biology* **2020**, *64*, 17–25. https://doi.org/10.1016/j.sbi.2020.05.011.
(96) Shi, Y.; Zhang, W.; Yang, Y.; Murzin, A. G.; Falcon, B.; Kotecha, A.; Van Beers, M.; Tarutani, A.; Kametani, F.; Garringer, H. J.; Vidal, R.; Hallinan, G. I.; Lashley, T.; Saito, Y.; Murayama, S.; Yoshida, M.; Tanaka, H.; Kakita, A.; Ikeuchi, T.; Robinson, A. C.; Mann, D. M. A.; Kovacs, G. G.; Revesz, T.; Ghetti, B.; Hasegawa, M.; Goedert, M.; Scheres, S. H. W. Structure-Based Classification of Tauopathies. *Nature* **2021**, *598* (7880), 359–363. https://doi.org/10.1038/s41586-021-03911-7.
(97) Rawat, P.; Sehar, U.; Bisht, J.; Selman, A.; Culberson, J.; Reddy, P. H. Phosphorylated Tau in Alzheimer's Disease and Other Tauopathies. *IJMS* **2022**, *23* (21), 12841. https://doi.org/10.3390/ijms232112841.
(98) Kitoka, K.; Skrabana, R.; Gasparik, N.; Hritz, J.; Jaudzems, K. NMR Studies of Tau Protein in Tauopathies. *Front. Mol. Biosci.* **2021**, *8*, 761227. https://doi.org/10.3389/fmolb.2021.761227.
(99) Basheer, N.; Smolek, T.; Hassan, I.; Liu, F.; Iqbal, K.; Zilka, N.; Novak, P. Does Modulation of Tau Hyperphosphorylation Represent a Reasonable Therapeutic Strategy for Alzheimer's Disease? From Preclinical Studies to the Clinical Trials. *Mol Psychiatry* **2023**, *28* (6), 2197–2214. https://doi.org/10.1038/s41380-023-02113-z.
(100) Barghorn, S.; Biernat, J.; Mandelkow, E. Purification of Recombinant Tau Protein and Preparation of Alzheimer-Paired Helical Filaments In Vitro. In *Amyloid Proteins*; Humana Press: New Jersey, 2004; Vol. 299, pp 035–052. https://doi.org/10.1385/1-59259-874-9:035.
(101) Wang, Q. M.; Fiol, C. J.; DePaoli-Roach, A. A.; Roach, P. J. Glycogen Synthase Kinase-3 Beta Is a Dual Specificity Kinase Differentially Regulated by Tyrosine and Serine/Threonine Phosphorylation. *J Biol Chem* **1994**, *269* (20), 14566–14574.
(102) Thingholm, T. E.; Larsen, M. R. Phosphopeptide Enrichment by Immobilized Metal Affinity Chromatography. In *Phospho-Proteomics*; Von Stechow, L., Ed.; Methods in Molecular Biology; Springer New York: New York, NY, 2016; Vol. 1355, pp 123–133. https://doi.org/10.1007/978-1-4939-3049-4_8.
(103) Ahmadi, S.; Zhu, S.; Sharma, R.; Wilson, D. J.; Kraatz, H.-B. Interaction of Metal Ions with Tau Protein. The Case for a Metal-Mediated Tau Aggregation. *Journal of Inorganic Biochemistry* **2019**, *194*, 44–51. https://doi.org/10.1016/j.jinorgbio.2019.02.007.
(104) Zhou, X.; Zhang, W.; Ouyang, Z. Recent Advances in On-Site Mass Spectrometry Analysis for Clinical Applications. *TrAC Trends in Analytical Chemistry* **2022**, *149*, 116548. https://doi.org/10.1016/j.trac.2022.116548.
(105) Wenk, D.; Zuo, C.; Kislinger, T.; Sepiashvili, L. Recent Developments in Mass-Spectrometry-Based Targeted Proteomics of Clinical Cancer Biomarkers. *Clin Proteom* **2024**, *21* (1), 6. https://doi.org/10.1186/s12014-024-09452-1.
(106) Thomas, S. N.; French, D.; Jannetto, P. J.; Rappold, B. A.; Clarke, W. A. Liquid Chromatography–Tandem Mass Spectrometry for Clinical Diagnostics. *Nat Rev Methods Primers* **2022**, *2* (1), 96. https://doi.org/10.1038/s43586-022-00175-x.
(107) Birhanu, A. G. Mass Spectrometry-Based Proteomics as an Emerging Tool in Clinical Laboratories. *Clin Proteom* **2023**, *20* (1), 32. https://doi.org/10.1186/s12014-023-09424-x.

(108) Findeisen, P.; Neumaier, M. Mass Spectrometry-Based Clinical Proteomics Profiling: Current Status and Future Directions. *Expert Review of Proteomics* **2009**, *6* (5), 457–459. https://doi.org/10.1586/epr.09.67.
(109) Lill, J. R.; Mathews, W. R.; Rose, C. M.; Schirle, M. Proteomics in the Pharmaceutical and Biotechnology Industry: A Look to the next Decade. *Expert Review of Proteomics* **2021**, *18* (7), 503–526. https://doi.org/10.1080/14789450.2021.1962300.
(110) Carter, M.; Shieh, J. Biochemical Assays and Intracellular Signaling. In *Guide to Research Techniques in Neuroscience*; Elsevier, 2015; pp 311–343. https://doi.org/10.1016/B978-0-12-800511-8.00015-0.
(111) Yang, R.; Li, F.; Zhang, W.; Shen, W.; Yang, D.; Bian, Z.; Cui, H. Chemiluminescence Immunoassays for Simultaneous Detection of Three Heart Disease Biomarkers Using Magnetic Carbon Composites and Three-Dimensional Microfluidic Paper-Based Device. *Anal. Chem.* **2019**, *91* (20), 13006–13013. https://doi.org/10.1021/acs.analchem.9b03066.
(112) Aydin, S.; Emre, E.; Ugur, K.; Aydin, M. A.; Sahin, İ.; Cinar, V.; Akbulut, T. An Overview of ELISA: A Review and Update on Best Laboratory Practices for Quantifying Peptides and Proteins in Biological Fluids. *J Int Med Res* **2025**, *53* (2), 03000605251315913. https://doi.org/10.1177/03000605251315913.
(113) Hoofnagle, A. N.; Wener, M. H. The Fundamental Flaws of Immunoassays and Potential Solutions Using Tandem Mass Spectrometry. *Journal of Immunological Methods* **2009**, *347* (1–2), 3–11. https://doi.org/10.1016/j.jim.2009.06.003.
(114) Rischke, S.; Hahnefeld, L.; Burla, B.; Behrens, F.; Gurke, R.; Garrett, T. J. Small Molecule Biomarker Discovery: Proposed Workflow for LC-MS-Based Clinical Research Projects. *Journal of Mass Spectrometry and Advances in the Clinical Lab* **2023**, *28*, 47–55. https://doi.org/10.1016/j.jmsacl.2023.02.003.
(115) Movassaghi, C. S.; Sun, J.; Jiang, Y.; Turner, N.; Chang, V.; Chung, N.; Chen, R. J.; Browne, E. N.; Lin, C.; Schweppe, D. K.; Malaker, S. A.; Meyer, J. G. Recent Advances in Mass Spectrometry-Based Bottom-Up Proteomics. *Anal. Chem.* **2025**, *97* (9), 4728–4749. https://doi.org/10.1021/acs.analchem.4c06750.
(116) Shiba, S.; Sychev, Z. E.; Evans, M. D.; Seegmiller, J. C. Liquid Chromatography Tandem Mass Spectrometry (LC-MS/MS) Candidate Reference Measurement Procedure for Urine Albumin. *Clinical Chemistry and Laboratory Medicine (CCLM)* **2025**, *63* (8), 1538–1547. https://doi.org/10.1515/cclm-2024-1374.
(117) Carvalho, J. R.; Machado, M. V. New Insights About Albumin and Liver Disease. *Annals of Hepatology* **2018**, *17* (4), 547–560. https://doi.org/10.5604/01.3001.0012.0916.
(118) Keller, U. Nutritional Laboratory Markers in Malnutrition. *JCM* **2019**, *8* (6), 775. https://doi.org/10.3390/jcm8060775.
(119) Kushnir, M. M.; Rockwood, A. L.; Roberts, W. L.; Abraham, D.; Hoofnagle, A. N.; Meikle, A. W. Measurement of Thyroglobulin by Liquid Chromatography–Tandem Mass Spectrometry in Serum and Plasma in the Presence of Antithyroglobulin Autoantibodies. *Clinical Chemistry* **2013**, *59* (6), 982–990. https://doi.org/10.1373/clinchem.2012.195594.
(120) Netzel, B. C.; Grant, R. P.; Hoofnagle, A. N.; Rockwood, A. L.; Shuford, C. M.; Grebe, S. K. G. First Steps toward Harmonization of LC-MS/MS Thyroglobulin Assays. *Clinical Chemistry* **2016**, *62* (1), 297–299. https://doi.org/10.1373/clinchem.2015.245266.
(121) Shuford, C. M.; Johnson, J. S.; Thompson, J. W.; Holland, P. L.; Hoofnagle, A. N.; Grant, R. P. More Sensitivity Is Always Better: Measuring Sub-Clinical Levels of Serum Thyroglobulin on a µLC–MS/MS System. *Clinical Mass Spectrometry* **2020**, *15*, 29–35. https://doi.org/10.1016/j.clinms.2020.01.001.

(122) Anacleto, J.; Wolf, E.; Ackloo, S.; Arrowsmith, C.; LeBlanc, Y.; Lento, C.; Wilson, D. J. Site-Specific Hydrogen–Deuterium Exchange Mass Spectrometry for Deep Explorations of Dynamic Shifts in Protein–Drug Interactions. *J. Am. Chem. Soc.* **2026**, jacs.6c03259. https://doi.org/10.1021/jacs.6c03259.

Appendices

Appendix A: Supplementary information for Chapter 2.

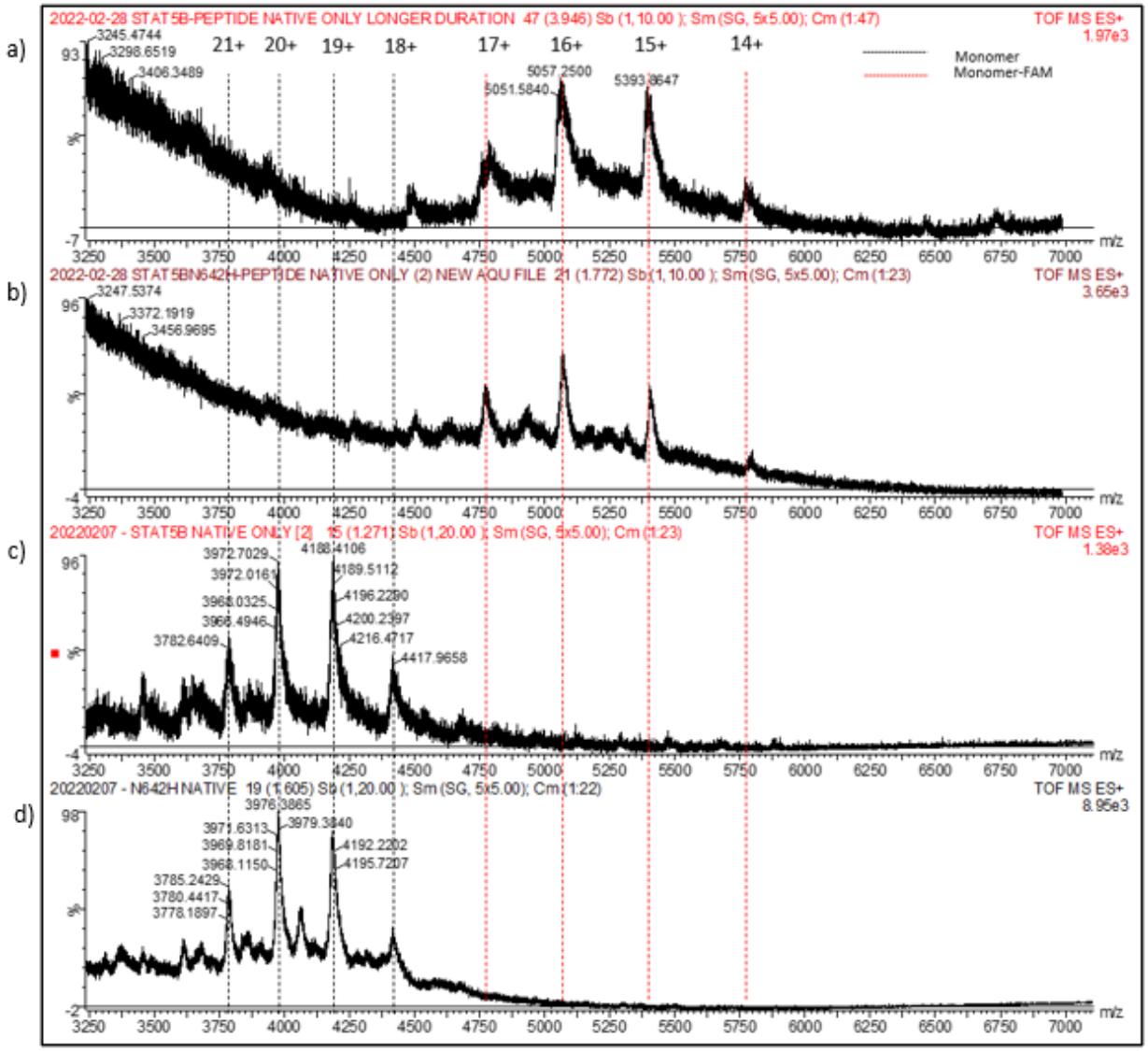


Figure S2.1. Native Mass Spectra: (a) STAT5B bound to FAM peptide in 0.7% DMSO (b) $STAT5B^{N642H}$ bound to FAM peptide in 0.7% (c) STAT5B in 0.7% DMSO, and (d) $STAT5B^{N642H}$ in 0.7% DMSO were buffer exchanged to 10 µM in 100 mM Ammonium Acetate (pH 7.0) using Thermo Scientific Zeba Spin Desalting column (40K MWCO) and infused into the Synapt G2-S mass spectrometer at a flow rate of 12 µL/min. Mass spectra were deconvoluted using ESIProt software.

Table S2.1: Relative deuterium uptake for peptides from STAT5B^{Y665F} over three time points along with their respective standard deviations (3σ).

Sequence	0.5 min	1 min	10 min	Summed3 sigma error
(152-171)	0.118647	-0.04117	-0.05212	0.707055
(154-163)	-0.41982	0.272844	0.723833	4.766759
(154-170)	-0.32477	-0.12309	-0.17208	1.213669
(199-211)	-1.05182	-1.17404	-0.47903	5.208361
(202-211)	-1.40281	-0.41849	-0.76608	3.803791
(205-213)	-1.04708	-0.72554	-0.94164	5.312548
(214-222)	-0.45081	-0.5211	-0.82366	2.161538
(214-224)	-0.35347	-0.08395	-0.66076	1.966151
(215-224)	-0.5278	-0.35239	-0.71578	2.428931
(225-239)	-0.19982	-0.17071	-0.42099	1.716815
(230-239)	-0.23788	-0.03297	-0.73621	1.344405
(240-248)	-0.34344	-0.66004	-0.63958	2.128699
(253-272)	-1.08977	-0.79149	-1.02949	1.749564
(285-299)	0.188336	0.12815	0.172071	0.871252
(313-318)	0.6765	1.65768	0.40956	2.790559
(322-327)	-0.26686	-0.35384	-0.8057	3.790597
(327-332)	0.1036	0.41914	0.11644	2.063282
(332-342)	-0.94676	-0.56976	-1.00916	2.305471
(333-342)	-0.48316	-0.49779	-0.62726	2.194418
(343-351)	-0.5	-0.74136	-1.06399	3.278318
(352-360)	-1.62738	-0.25654	-0.92351	6.733698
(355-371)	-1.31734	-0.8582	-1.21635	3.296075
(361-371)	-0.64048	-0.50048	-0.91105	6.705585
(372-383)	-2.28952	-1.54129	-1.63517	2.488051
(384-397)	-0.97122	-1.1821	-1.2804	3.242719
(384-399)	-0.80325	-0.61296	-0.94755	3.435922
(404-412)	-0.79777	-0.70631	-1.02269	2.555275
(404-414)	-0.89933	-0.75522	-0.84098	2.349246
(413-421)	-0.05171	-0.28376	-0.99531	3.007081
(415-421)	-0.71168	-0.90507	-1.33472	3.642574
(456-464)	-0.70729	-0.23552	-0.64542	1.320503
(465-480)	-3.94038	-3.2447	-3.40804	5.766964
(468-480)	-2.36789	-1.54094	-1.7896	4.678184
(516-530)	-0.40604	-0.44641	-1.26779	1.868849
(516-532)	-0.37266	-0.64901	-0.88647	1.735025
(531-545)	-0.41586	-0.57642	-0.65897	1.817419
(531-547)	-0.59149	-0.37482	-0.51475	2.223383
(534-547)	-0.27483	-0.85555	-0.68858	3.116884
(538-545)	-1.24646	-1.23751	-1.11217	2.62412
(538-547)	-1.08167	-1.01431	-1.19479	2.376006
(559-567)	-1.34019	-1.06571	-1.59014	2.749917

(579-597)	-0.14285	-0.26828	-0.81862	2.224303
(596-607)	-0.58445	-0.87147	-1.24743	2.891824
(598-607)	-0.42236	-0.66849	-0.83978	2.260391
(608-616)	-0.09014	0.229429	-0.27719	2.125886
(609-616)	-0.19065	-0.38775	-1.2354	5.430473
(616-623)	-0.82074	-0.77743	-1.45891	2.499697
(616-626)	-0.35074	0.07486	-0.65243	2.012462
(617-626)	-0.73238	-0.62463	-0.98209	2.769321
(617-628)	-0.72128	-0.52322	-0.87236	1.675178
(623-628)	0.30944	0.12236	0.37872	3.853403
(629-636)	-4.61489	-4.44974	-2.00806	3.822123
(634-641)	-2.59601	-2.29167	-1.23773	5.227921
(637-643)	-3.72175	-2.41642	-1.14133	4.379117
(641-650)	-1.87458	-1.19775	-0.2594	2.639095
(642-650)	-1.92653	-1.21513	-1.11943	2.024274
(644-651)	-0.76737	-0.54798	-1.24817	4.05329
(651-663)	-1.16323	-1.23876	-2.80798	3.446405
(653-663)	0.79943	0.66338	-1.42623	6.310453
(658-665)	-5.0829	-5.64629	-4.64013	2.432308
(662-673)	-0.62999	-0.34975	-0.33372	2.918149
(666-678)	-0.34934	-0.39238	-0.44923	1.688004
(666-679)	0.1118	-0.31847	0.221673	1.465358
(666-682)	-0.16816	-0.13004	-0.53505	1.423933
(667-682)	-1.47573	-0.63727	-1.47925	2.653293
(699-714)	-0.33651	-0.23899	-0.5079	2.904041
(741-751)	0.067438	-0.03215	-0.51684	4.502531

Table S2.2: Relative deuterium uptake for peptides from STAT5B^{T648S} over three time points along with their respective standard deviations (3σ).

Sequence	0.5 mins	10 min	Summed 3 sigma error
(133-147)	-0.52679	-0.36061	3.218922
(133-148)	-1.1684	-1.01074	2.450821
(149-165)	0.116863	-0.88012	2.152256
(151-170)	0.319179	0.200595	0.606462
(152-171)	0.166074	0.160895	2.079741
(154-163)	0.512011	-0.1327	3.588916
(154-170)	0.1535	0.089569	1.070365
(171-175)	0.013475	0.453325	2.764856
(176-180)	0.7412	0.04115	2.811719
(199-211)	0.007342	-0.84282	4.265678
(202-211)	1.038267	-0.63768	4.25663
(205-213)	0.915388	-0.58915	4.007893
(214-224)	0.57156	0.00351	2.38982
(215-224)	0.819767	0.114767	2.447806
(216-224)	1.278638	0.158063	2.427802
(225-239)	-0.02484	0.092679	1.500677
(230-239)	-0.05324	-0.48291	1.410707
(240-248)	-0.06949	0.048012	1.459567
(253-272)	0.969841	0.271453	1.442453
(273-277)	1.777775	0.869675	1.903415
(313-317)	1.667875	0.498525	2.851704
(313-318)	1.26348	0.41204	2.690135
(318-322)	0.16595	0.04605	2.254337
(322-327)	0.133	0.81332	2.521569
(323-327)	0.72205	1.0357	1.878778
(327-331)	1.03475	-0.04307	1.722075
(327-332)	0.76652	0.17466	1.810151
(332-342)	1.118475	0.172913	2.542483
(333-342)	1.061929	0.649443	2.107136
(333-348)	0.323592	-0.37522	3.023707
(343-351)	0.486625	-0.04666	2.368186
(355-371)	2.164886	-0.15285	4.365093
(357-366)	0.244913	-0.36796	3.560228
(361-371)	2.93355	-0.64654	5.467451
(372-376)	0.046925	0.65845	1.472331
(372-383)	0.347191	-0.47903	2.500903
(384-397)	-0.24281	-0.87302	2.823369
(384-399)	2.412753	-0.14374	3.022989
(404-412)	-0.02225	-1.3719	2.677148
(404-414)	0.05051	-0.9677	2.966749
(444-448)	1.622	0.1187	1.27622
(448-454)	0.44055	-0.53133	2.76102
(456-464)	0.754025	-0.21676	1.471258

(465-480)	1.271614	1.0346	4.858636
(468-480)	1.411475	0.519892	3.109295
(508-513)	0.56476	0.29364	3.883559
(516-530)	0.519321	0.218721	2.310283
(531-545)	-0.00921	0.003729	1.893011
(531-547)	0.267594	-0.50319	1.992133
(534-547)	0.017323	0.032885	2.926038
(538-547)	0.013433	-0.48041	2.548508
(546-551)	0.0982	-0.02132	0.916466
(559-567)	-0.02503	-0.42587	4.993415
(579-597)	0.237612	-0.21676	1.686534
(596-607)	0.222164	-0.07825	3.82994
(598-607)	0.241767	-0.06699	2.178727
(606-616)	-0.28034	-0.83544	3.785838
(608-616)	0.638057	-0.15429	1.288854
(616-623)	0.355414	-0.54014	0.934843
(616-628)	0.872033	0.272742	2.956925
(617-628)	0.838527	0.3537	2.149232
(629-633)	0.8814	-0.57617	2.591421
(629-636)	0.393729	-0.2699	3.972394
(637-643)	-1.33533	-0.65707	3.737004
(651-665)	-0.8165	-1.76699	0.974568
(652-663)	-0.81505	-1.65307	0.590129
(656-665)	-0.42571	-0.87721	2.640907
(666-670)	-0.37458	-0.6989	3.872483
(666-679)	-0.15569	0.334982	1.824923
(666-682)	-0.12877	-0.19193	0.73423
(667-678)	0.0282	0.342822	1.49969
(667-682)	-0.38203	-0.06897	0.991349
(668-678)	-0.0913	-0.16809	2.580003
(669-679)	-0.04347	-0.48909	2.410311
(699-714)	-0.0978	-0.38619	3.333339
(741-751)	0.955662	0.37195	3.058819
(752-757)	0.66868	0.35802	1.251835
(762-766)	0.733875	0.53525	3.114587
(773-785)	-0.95688	-0.77903	2.718881

Table S2.3: Relative deuterium uptake for peptides from STAT5B^{T628S} over three time points along with their respective standard deviations (3σ).

Sequence	1min	10min	60min	3 sigma error
133-148	0.879764	-0.36009	0.238571	3.338171
133-149	0.854833	-0.36497	0.44032	4.408504
151-171	-0.10703	0.085553	0.118126	2.563954
152-164	-0.51133	-0.24745	0.131409	7.718358
152-171	-0.23192	-0.06133	0.213944	3.430432

162-172	-0.47379	-0.46963	-0.37198	3.951889
202-212	0.494178	-0.71119	0.426944	7.092093
205-214	-0.42847	-1.23514	-0.22945	7.744682
215-225	-0.28379	0.148389	0.198456	10.87955
216-225	-0.75076	0.313688	-0.55075	8.060619
224-235	-0.65459	-0.08693	-0.43417	9.18579
225-240	-0.0586	0.089979	0.130779	2.653901
230-240	-0.27222	-0.2598	-0.39549	2.573391
231-240	0.026625	-0.31034	-0.11791	5.311465
232-240	0.775614	0.6147	-0.20376	7.752474
240-249	-0.26671	-0.30071	-0.19089	2.003703
253-273	0.250676	0.400265	0.254847	3.223969
285-300	-0.17046	0.074457	-0.06781	1.321764
313-318	-0.17015	-0.38908	-0.01893	12.04247
313-319	-0.20112	-1.07044	-0.12406	7.75731
318-323	-0.29453	-1.0903	0.239	6.773667
322-328	-0.77658	0.35646	-0.8893	8.293332
323-328	-0.3565	1.0656	0.08095	5.026407
327-332	-0.0976	-0.82612	0.281875	5.795943
327-333	-0.17634	-0.90914	-0.0201	5.622378
332-343	-0.01866	0.295337	0.194613	4.402055
333-343	-0.39711	0.030543	-0.09856	3.685248
352-361	-0.14924	0.453637	-0.00705	4.470483
355-361	0.51866	0.7422	0.18636	8.131569
356-361	0.48845	0.75535	0.102375	11.71474
361-372	-0.13241	0.309175	-0.15356	3.939504
374-384	-0.01778	0.492589	0.077167	2.547047
384-400	0.04154	0.10752	-0.12081	4.744664
396-402	1.09708	0.61422	0.66456	8.858718
404-413	-0.09186	0.697389	-0.4164	5.427184
405-415	-0.20099	0.3573	0.0274	5.987323
413-422	-0.65517	-0.2393	-0.0645	6.995911
444-449	-0.05483	-0.06765	-0.37379	2.350489
457-474	-0.79925	0.185742	0.728467	11.57226
468-481	0.276512	0.002613	0.346888	4.051476
514-531	0.364814	0.152036	0.000507	3.790847
516-531	0.14385	-0.28623	-0.0496	3.850583
533-538	-0.15541	-0.16623	-0.19493	3.011925
533-546	-0.22679	0.040014	0.103	3.502241
538-546	-0.06697	-0.00392	0.081833	3.202428
538-548	-0.84205	-1.0315	0.45105	6.361849
554-559	-0.09423	0.0981	-0.52677	2.866312
579-597	0.151247	-0.04345	-0.55721	3.502432
579-598	0.52155	-0.33279	-1.02349	2.366767
597-608	-0.29048	-0.33582	-1.34477	2.825688
598-608	-0.17276	-0.001	-0.35116	3.205479

606-617	0.054029	0.337829	0.528243	4.55709
608-617	0.660983	0.507383	0.2025	2.350841
609-617	0.3673	-0.42749	-1.65536	1.951975
616-624	-0.19199	-0.6805	-0.23363	4.955824
634-642	-0.60892	-1.25955	-0.88445	5.99948
637-644	-0.0163	0.375917	-0.43877	2.753296
651-664	0.145686	0.204764	-0.40904	2.025186
651-666	0.033615	0.055146	-1.04933	2.789882
652-666	0.110563	-0.47143	-1.31025	4.360228
657-666	0.398543	-0.70563	-1.36329	3.432959
658-666	-0.37797	-0.24604	-0.08592	1.312768
666-679	-0.31453	0.1428	0.160282	1.70603
666-680	-0.12203	0.0178	-0.33093	3.739973
667-679	-0.25223	-0.00556	0.22752	2.108059
667-680	-0.43113	-0.8112	-0.74999	4.091325
699-715	-0.2024	-1.39804	-0.49266	3.188191
725-736	0.090525	-0.01809	-0.04626	3.498328
741-752	-0.73638	-0.6797	-0.59772	2.569456
752-758	-0.2376	-0.82688	-0.21475	4.895607

Table S2.4: Relative deuterium uptake for peptides from STAT5B^{L327M} over three time points along with their respective standard deviations (3σ).

Sequence	0.5	1	10	3 sigma error
(202 - 211)	1.808502	0.813733	0.50844	3.130674
(230 - 239)	0.258566	0.297139	0.413098	0.968804
(240 - 248)	0.420354	0.329319	0.267429	1.017102
(327 - 332)	0.809389	0.396207	0.556323	1.761918
(333 - 342)	0.597556	0.607189	0.710814	1.915558
(343 - 351)	0.951829	0.798811	0.631556	2.382197
(372 - 383)	0.936465	0.795444	0.310969	2.042878
(374 - 383)	0.586733	0.635454	0.799581	2.021768
(396 - 401)	1.493223	1.54328	1.192721	4.229224
(403 - 412)	1.815044	1.682615	0.943433	4.441091
(404 - 412)	1.932243	0.98206	0.893635	3.807937
(413 - 421)	0.721667	0.592797	0.579926	1.894389
(448 - 454)	2.147679	1.076579	0.572076	3.796334
(456 - 464)	0.888916	0.604072	0.696515	2.189504
(468 - 480)	2.133549	1.451284	1.632182	5.217016
(516 - 532)	1.014443	0.654871	0.498974	2.168287
(531 - 545)	1.299112	0.965876	0.369641	2.63463
(533 - 547)	1.111353	0.947669	0.562336	2.621358
(538 - 547)	2.038367	1.052077	0.646763	3.737207
(546 - 551)	1.736389	1.121275	0.940041	3.797705
(550 - 561)	1.843932	1.58274	0.571301	3.997973
(559 - 567)	1.522269	1.282327	0.547737	3.352332
(596 - 607)	0.824778	0.734273	0.144645	1.703696
(598 - 607)	1.104252	1.024963	0.759787	2.889002
(608 - 616)	0.476578	0.544602	0.515692	1.536872
(616 - 623)	0.492598	0.687939	0.228887	1.409424
(616 - 626)	0.438901	0.54474	0.50776	1.491401
(616 - 628)	1.056499	0.796593	0.926858	2.77995
(617 - 628)	0.80595	0.681471	0.59347	2.080892
(629 - 633)	0.900178	0.567386	0.44461	1.912174
(641 - 650)	2.158155	1.777735	1.11963	5.055521
(642 - 650)	1.424033	1.332066	0.712297	3.468396
(651 - 665)	0.736393	0.683364	0.423822	1.84358
(652 - 663)	0.334753	0.935388	0.344698	1.614839
(653 - 663)	1.073015	0.792025	0.521281	2.386321
(657 - 665)	0.945396	1.137789	0.634393	2.717577
(666 - 679)	0.354595	0.469881	0.219087	1.043563
(667 - 679)	0.565619	0.481221	0.364478	1.411318
(667 - 682)	0.625827	0.476984	0.282419	1.38523
(669 - 678)	1.011299	0.914764	1.320154	3.246217
(679 - 689)	2.661528	1.810159	1.622263	6.09395
(679 - 690)	1.616385	1.284348	0.746759	3.647492

Table S2.5: Relative deuterium uptake for peptides from STAT5B^{S434L} over three time points along with their respective standard deviations (3σ).

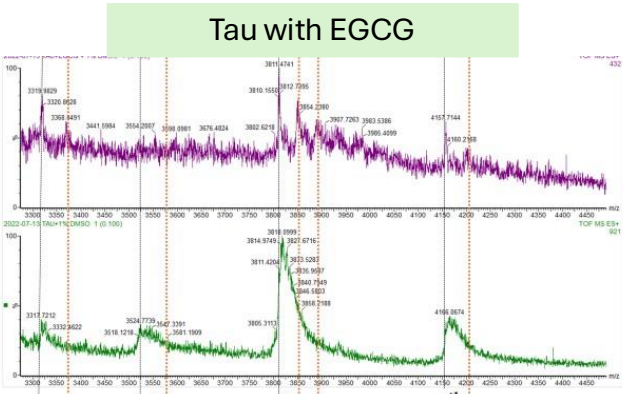
Sequence	0.5	1	10	3 sigma error
(202 - 211)	1.808502	0.813733	0.50844	3.130674
(230 - 239)	0.258566	0.297139	0.413098	0.968804
(240 - 248)	0.420354	0.329319	0.267429	1.017102
(327 - 332)	0.809389	0.396207	0.556323	1.761918
(333 - 342)	0.597556	0.607189	0.710814	1.915558
(343 - 351)	0.951829	0.798811	0.631556	2.382197
(372 - 383)	0.936465	0.795444	0.310969	2.042878
(374 - 383)	0.586733	0.635454	0.799581	2.021768
(396 - 401)	1.493223	1.54328	1.192721	4.229224
(403 - 412)	1.815044	1.682615	0.943433	4.441091
(404 - 412)	1.932243	0.98206	0.893635	3.807937
(413 - 421)	0.721667	0.592797	0.579926	1.894389
(448 - 454)	2.147679	1.076579	0.572076	3.796334
(456 - 464)	0.888916	0.604072	0.696515	2.189504
(468 - 480)	2.133549	1.451284	1.632182	5.217016
(516 - 532)	1.014443	0.654871	0.498974	2.168287
(531 - 545)	1.299112	0.965876	0.369641	2.63463
(533 - 547)	1.111353	0.947669	0.562336	2.621358
(538 - 547)	2.038367	1.052077	0.646763	3.737207
(546 - 551)	1.736389	1.121275	0.940041	3.797705
(550 - 561)	1.843932	1.58274	0.571301	3.997973
(559 - 567)	1.522269	1.282327	0.547737	3.352332
(596 - 607)	0.824778	0.734273	0.144645	1.703696
(598 - 607)	1.104252	1.024963	0.759787	2.889002
(608 - 616)	0.476578	0.544602	0.515692	1.536872
(616 - 623)	0.492598	0.687939	0.228887	1.409424
(616 - 626)	0.438901	0.54474	0.50776	1.491401
(616 - 628)	1.056499	0.796593	0.926858	2.77995
(617 - 628)	0.80595	0.681471	0.59347	2.080892
(629 - 633)	0.900178	0.567386	0.44461	1.912174
(641 - 650)	2.158155	1.777735	1.11963	5.055521
(642 - 650)	1.424033	1.332066	0.712297	3.468396
(651 - 665)	0.736393	0.683364	0.423822	1.84358
(652 - 663)	0.334753	0.935388	0.344698	1.614839
(653 - 663)	1.073015	0.792025	0.521281	2.386321
(657 - 665)	0.945396	1.137789	0.634393	2.717577
(666 - 679)	0.354595	0.469881	0.219087	1.043563
(667 - 679)	0.565619	0.481221	0.364478	1.411318
(667 - 682)	0.625827	0.476984	0.282419	1.38523
(669 - 678)	1.011299	0.914764	1.320154	3.246217

(679 - 689)	2.661528	1.810159	1.622263	6.09395
(679 - 690)	1.616385	1.284348	0.746759	3.647492

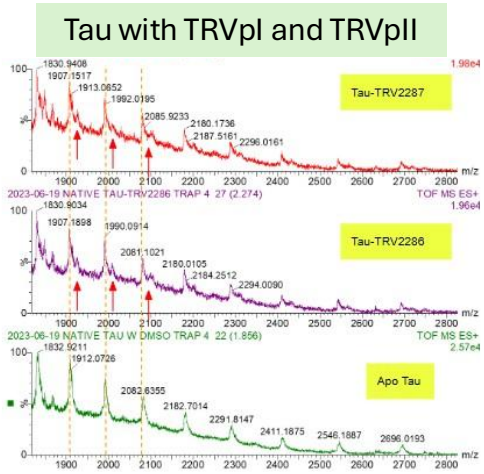
Appendix B: Supplementary information for Chapter 3.

Following successful expression and purification of native tau, native mass spectrometry was performed to confirm the purity of the protein (Figure S3.1a). Purified tau was subsequently screened against seven small-molecule drug candidates developed by collaborators at Treventis Corp (Figure S3.1 and Figure S3.3). The goal of this study was to identify potential candidates capable of binding monomeric tau and preventing its subsequent oligomerization. Of the seven candidates tested, only TRVpI and TRVpII showed mass increases corresponding to the expected masses of their respective binding partners (Figure S3.1b). However, no differences in deuterium uptake were observed for these candidates under CFI-TRESI-HDX conditions (Figure S3.2). This suggests that either the observed binding is non-specific or that the interaction does not induce significant perturbations to the hydrogen-bonding network, such as through interactions primarily involving amino acid side chains. Epigallocatechin gallate (EGCG) was used as a positive control for tau binding (Figure S3.1a).

(a)



(b)



S3.1: Native MS of Tau with positive binding partners (a) EGCG and (b) TRVpI and TRVpII.

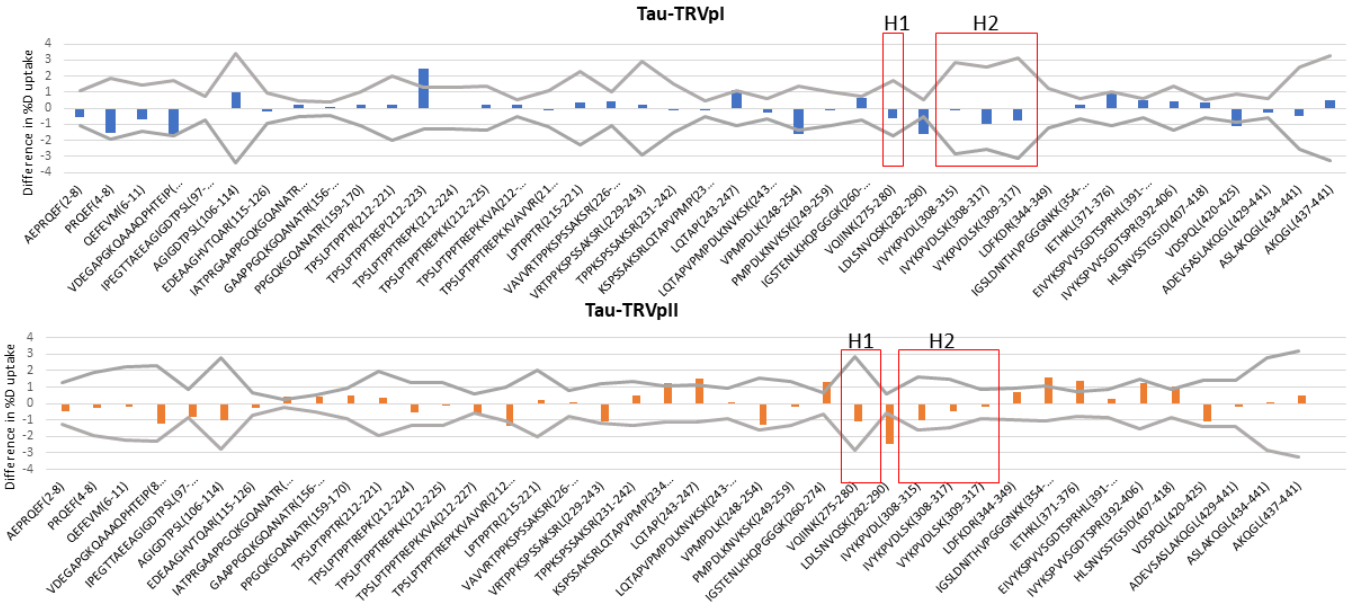
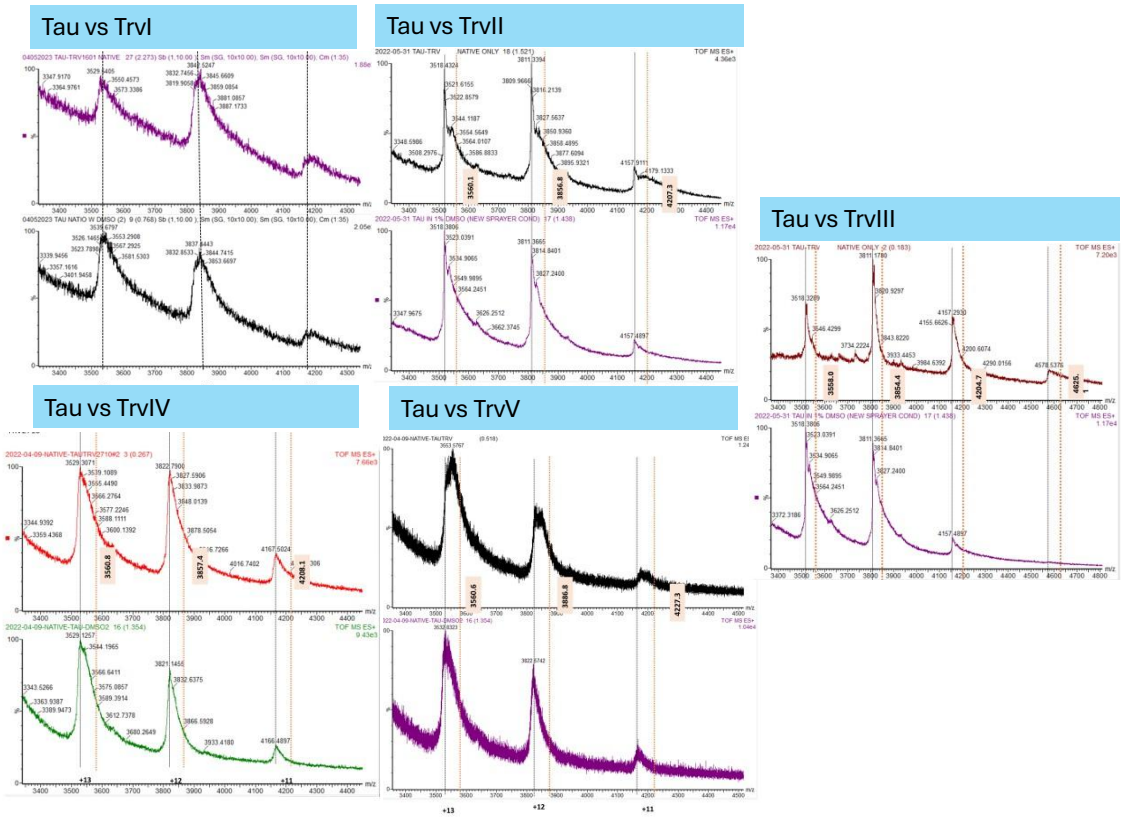
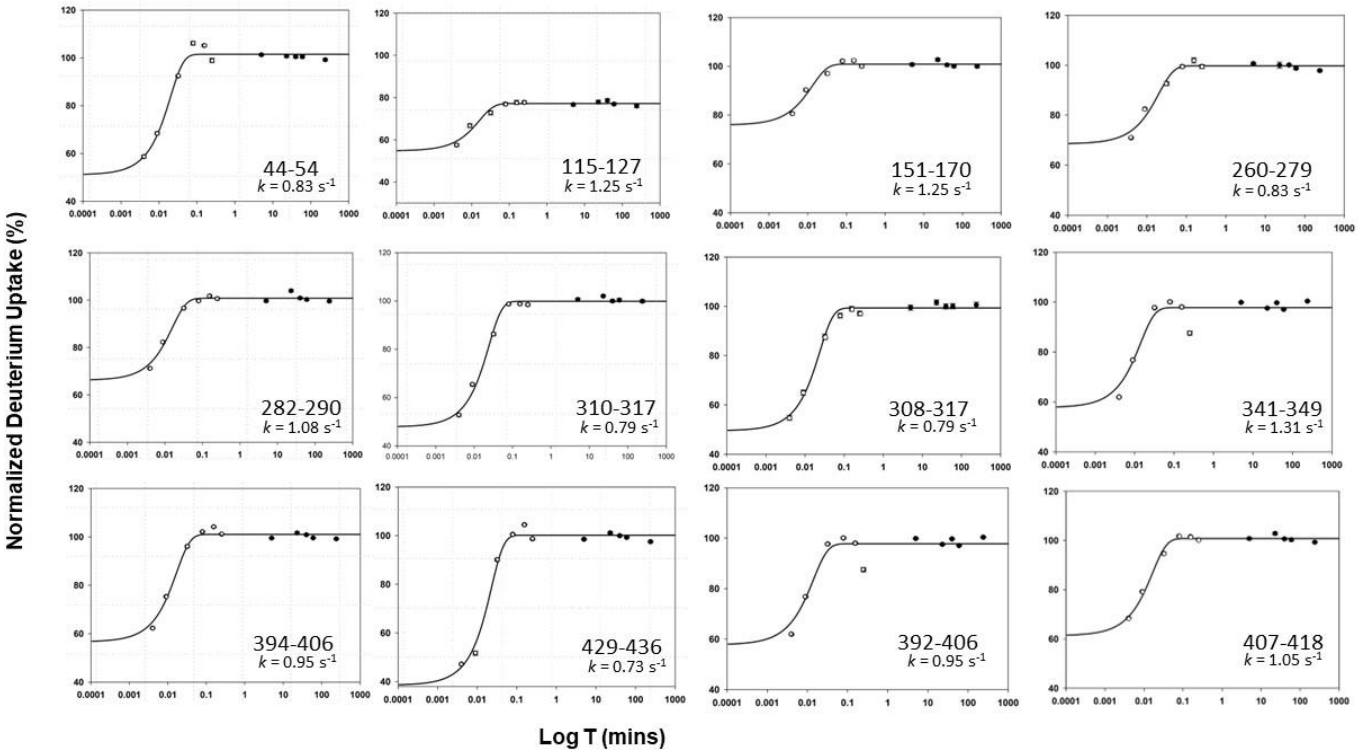


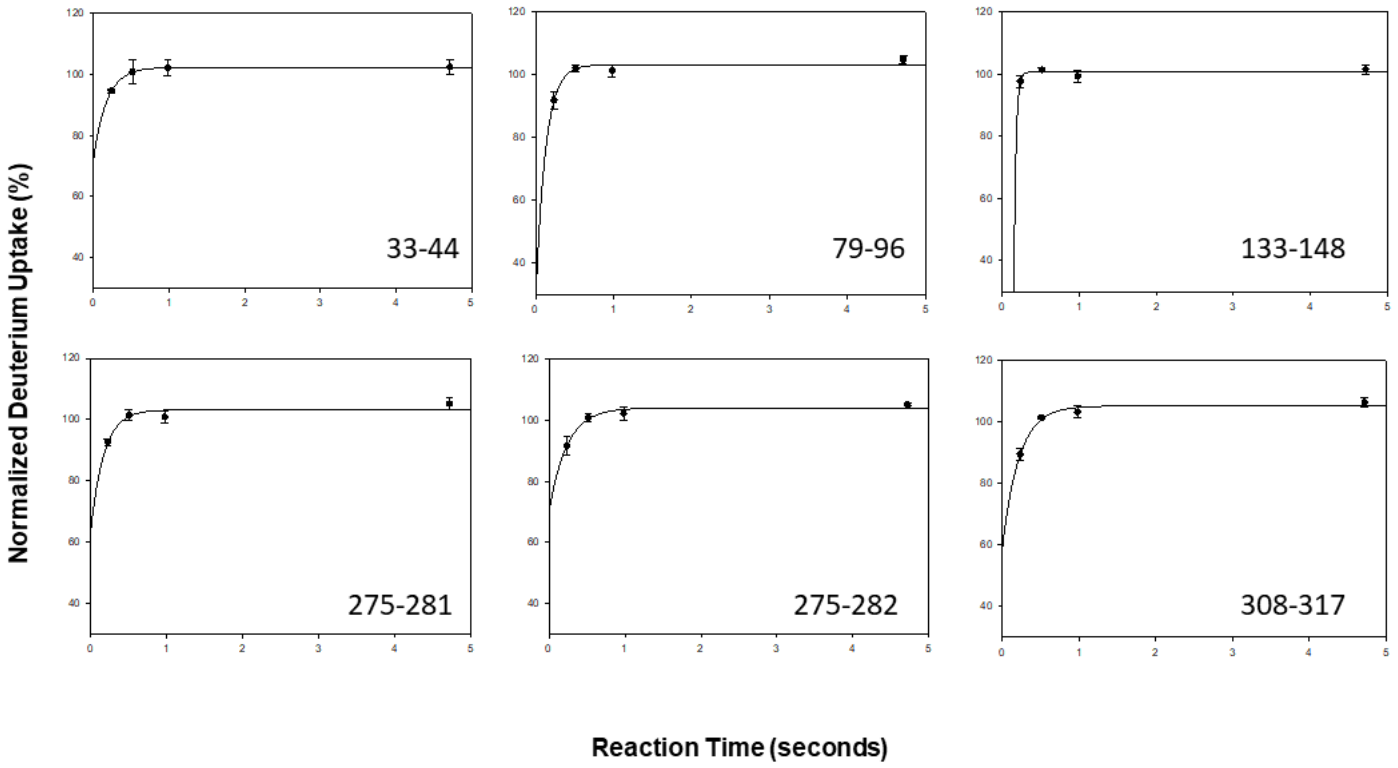
Figure 3.2: Difference in deuterium uptake upon binding of TRVpI and TRVpII to tau. No statistically significant differences in the hexapeptide I and II regions were observed upon binding.



S3.3: Native MS of Tau with potential drug candidates. No evidence of binding was observed between unbound tau (bottom spectra) and bound tau (top spectra).

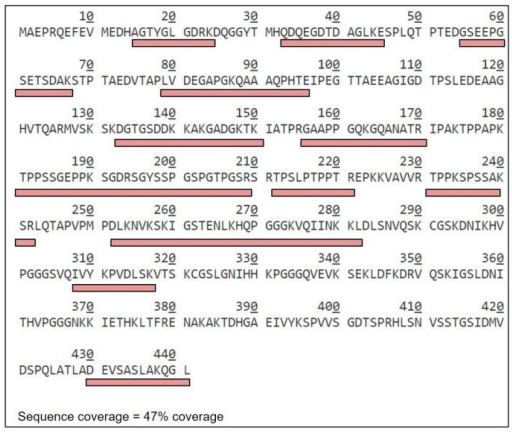


S3.4: Normalized deuterium uptake (%) curves for Tau peptides and their respective rates obtained from CFI-TRESI-HDX with LC separation and discrete time points ranging from 50 ms to 4 h.



S3.5: Normalized deuterium uptake (%) curves for Tau peptides and their respective rates obtained from CFI-TRESI-HDX without LC separation and discrete time points ranging from 50 ms to 5 minutes. This data represents a significant increase in overall deuterium uptake (or reduced back-exchange) compared to CFID mode with LC separation.

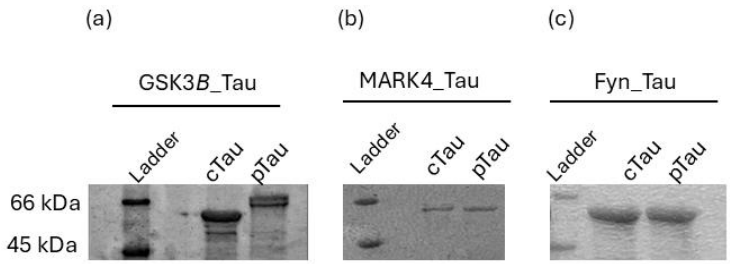
a)



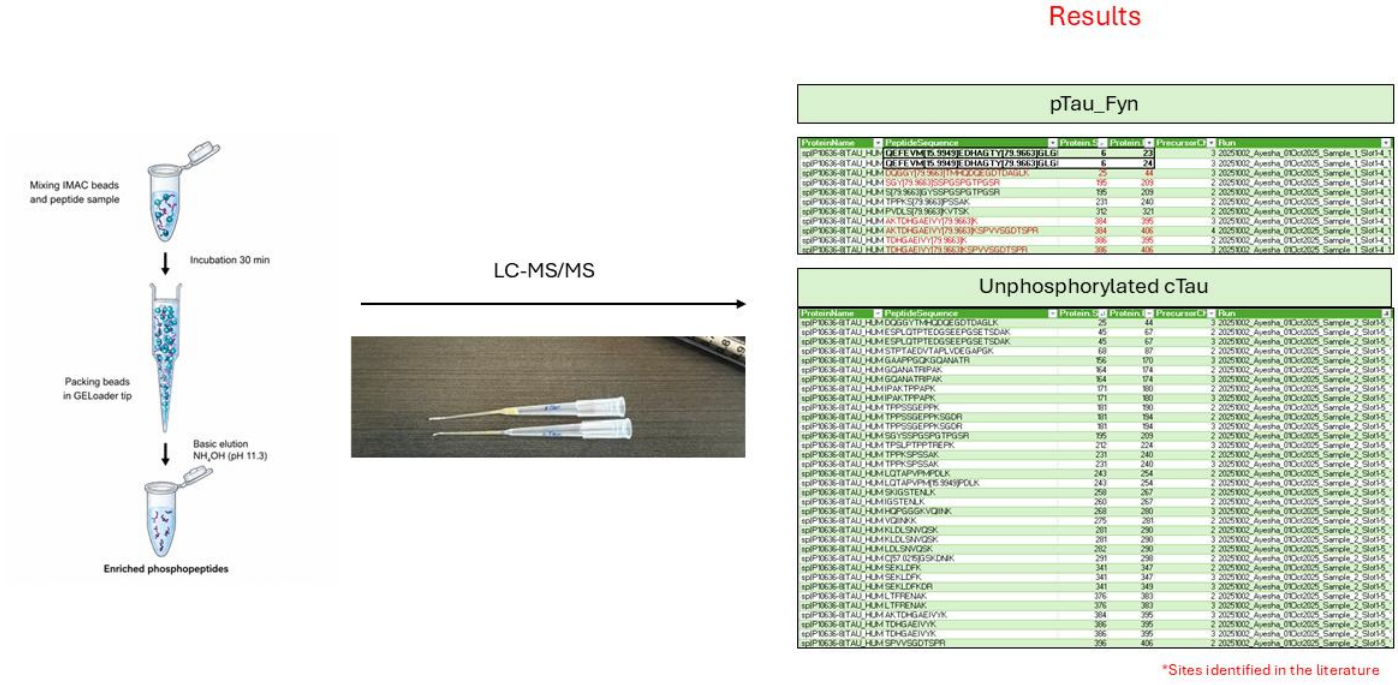
b)



S3.6: Increase in peptide sequence coverage for tau protein from 47% to 71.9% using (a) CFI-TRESI and (b) CFI-TRESI with trap column.



S3.7: Denaturing SDS-PAGE analysis of phosphorylated Tau. Phosphorylation of control tau (cTau) using (a) GSK3B, (b) MARK4, and (c) Fyn kinases was performed to obtain phosphorylated tau species. Only tau phosphorylated using GSK3B showed a mobility shift to a higher mass state, suggesting a successful phosphorylation reaction.



S3.8: Phosphoproteomics using Fe^{3+}-IMAC affinity beads packed in a micropipette for the enrichment of Tau phosphopeptides. The sample was then subjected to MS/MS experiments for the identification of phosphorylation sites.

Appendix C: Supplementary information for Chapter 4.

A. Materials

Table S4.1: Materials

Reagents	Cas No.	Vendor	Cat. No	Quality
Trypsin from porcine pancreas	9002-07-7	Sigma - Aldrich	T0303-1G	R&D use only
rLys-C	2026-11-05	Promega	V1671	Mass Spec Grade
Strata-X PRO	S432-0004	Phenomenex	8B-D536-FCH	LC-MS grade
Sep-Pak Vac 1cc tC18 cartridges	(Part no.) WAT054960	Waters	013332298B	LC-MS grade

B. Preparation of Reagents

Table S4.2 Reagents

Reagents	Cas No.	Vendor	Cat. No	Quality
Deionized Water	7732-18-5	Fisher Scientific	23-751-628	Deionized and Ozonated
Methanol	67-56-1	Fisher Chemicals	A452-4	HPLC Grade
Ammonium Bicarbonate	1066-33-7	Sigma - Aldrich	A6141-500G	Reagent Grade, 99%
Ammonium Acetate	631-61-8	Fisher Chemicals	A639-500	HPLC Grade
Acetonitrile	75-05-8	Fisher Chemicals	A998-4	HPLC grade
DTT	3483-t2-3	Roche	10197777001	R&D use only
Iodoacetamide	144-48-9	Sigma – Aldrich	I6125-5G	≥99%
2-Chroloacetamide	79-07-2	Sigma – Aldrich	C0267-100G	≥98%
Urea	57-13-6	Sigma – Aldrich	U5378-100G	≥98%
Formic Acid	64-18-6	Fisher Chemicals	A117-50	LC/MS grade
Dimethyl Sulfoxide	67-68-5	Fisher Chemicals	D159-4	HPLC grade

C. Preparation of Calibrators

Table S4.3 Calibrators and Internal Standard

Analyte	QTY	Vendor	Cat. No.	Purity
Human Albumin	5 g	Sigma - Aldrich	A9731-5G	≥ 96%
Bovine Thyroglobulin	100mg	Sigma - Aldrich	T1001-100MG	≥ 90%
Human Thyroglobulin	1 mg	Millipore Sigma	609312-1MG	≥ 95%
Pierce BSA protein digest standard	1nmol	Fisher Scientific	AA407883	LC-MS grade
Human Serum Double Charcoal treated and	100 mL	GoldenWest	SP1070	100%

delipidized from defibrinated plasma				
Normal Human Serum	500 mL	UTAK	D6254	100%

D. Preparation of Quality Control

Table S4.4 Quality Controls Standards

Standard	Quantity	Vendor	Cat. No.	Purity
Human Albumin	5 g	Sigma - Aldrich	A9731-5G	≥ 96%
Bovine Thyroglobulin	100mg	Sigma - Aldrich	T1001-100MG	≥ 90%
Human Thyroglobulin	1 mg	Millipore Sigma	609312-1MG	≥ 95%

E. Mass Spectrometer Instrument Parameters

Table S4.5 Mass Spectrometer Parameters

Instrument Manufacturer and Model: *Sciex X500r QTOF*	
Instrument Serial Number(s): *DM230162003-DGB7X63*	
Instrument Parameters	**Value**
Polarity	Positive
Scan Mode	Guided MRM HR
Ion Source	TurboIon Spray
Resolution Q1	
Resolution Q3	
CUR	25 psi
IS	5500v
TEM	650 °C
GS1	60 psi
GS2	50 psi
EP	70V
CAD	7
CEM	10
Dwell Time	0.1s

F. Chromatographic Parameters

Table S4.6 Liquid Chromatography Parameters

Instrument Manufacturer and Model: *Sciex ExionLC*
Instrument Serial Number(s): - *Channel Solvent Degasser (ABDG55873684)* - *AC pumps (ABDXR5872231 and ABDXR5872232)* - *Multiplate autosampler (ABAMP5870437)* - *Controller module for ExionLC S (ABCBM5873312)* - *Column Oven 120V (AB2ST5850508)*

Instrument/Method Parameters	Value
Mobile Phase	0.1% FA in water or acetonitrile
Column	Kinetex C18 2.6 um
Column Oven Temperature	40 °C
Flow Rate	0.30 ul/min
Acquisition Time	10 min
Injection Volume	10-20 ul

G. Elution Gradient

Table S4.7 Liquid Chromatography elution gradient

Step	Total Time (min)	Flow Rate (mL/min)	A (%)	B(%)
0	0.5	0.30	95.0	5.0
1	6.0	0.30	65.0	35.0
2	7.0	0.30	40.0	60.0
3	8.5	0.30	40.0	60.0
4	9.0	0.30	95.0	5.0
5	10.0	0.30	95.0	5.0

Table S4.1 | Optimized multiple reaction monitoring (MRM) transitions used for targeted LC–MS/MS quantification of albumin and human thyroglobulin (hTG) peptides. Product ions and collision energies (CE) were selected based on signal intensity and specificity. An internal standard (IS) was used for normalization and quantitative analysis in both assays.

Analyte	Precursor Ion (m/z)	Product Ion (m/z)	Collision Energy (V)
Albumin Peptide	507.21	189.1092	15
	507.21	86.0589	35
	507.21	712.3463	15
	507.21	825.4281	15
	507.21	143.1062	30
hTG Peptide	636.80	185.1918	30
	636.80	120.0731	85
	636.80	70.0602	90
	636.80	86.0925	55
	636.80	72.0762	85
Internal Standard	473.88	721.2636	20
	473.88	120.0732	40
	473.88	110.0648	45
	473.88	307.1230	30
	473.88	420.1966	20